

**NOVEL APPROACHES TO CONTROL THE
PROPAGATION OF ELECTROMAGNETIC
WAVES: METAMATERIALS AND
PHOTONIC CRYSTALS**

A DISSERTATION SUBMITTED TO
THE DEPARTMENT OF PHYSICS
AND THE INSTITUTE OF ENGINEERING AND SCIENCE
OF BILKENT UNIVERSITY
IN PARTIAL FULFILLMENT OF THE REQUIREMENTS
FOR THE DEGREE OF
DOCTOR OF PHILOSOPHY

By
İrfan Bulu
March, 2007

I certify that I have read this thesis and that in my opinion it is fully adequate, in scope and in quality, as a dissertation for the degree of doctor of philosophy.

Prof. Dr. Ekmel Özbay(Supervisor)

I certify that I have read this thesis and that in my opinion it is fully adequate, in scope and in quality, as a dissertation for the degree of doctor of philosophy.

Asst. Prof. Dr. M. Özgür Oktel

I certify that I have read this thesis and that in my opinion it is fully adequate, in scope and in quality, as a dissertation for the degree of doctor of philosophy.

Asst. Prof. Dr. Hilmi Volkan Demir

I certify that I have read this thesis and that in my opinion it is fully adequate, in scope and in quality, as a dissertation for the degree of doctor of philosophy.

Asst. Prof. Dr. Fatih Ömer İlday

I certify that I have read this thesis and that in my opinion it is fully adequate, in scope and in quality, as a dissertation for the degree of doctor of philosophy.

Assoc. Prof. Dr. Birsen Saka Tanatar

Approved for the Institute of Engineering and Science:

Prof. Dr. Mehmet Baray
Director of the Institute

ABSTRACT

NOVEL APPROACHES TO CONTROL THE PROPAGATION OF ELECTROMAGNETIC WAVES: METAMATERIALS AND PHOTONIC CRYSTALS

İrfan Bulu

PhD in Physics

Supervisor: Prof. Dr. Ekmel Özbay

March, 2007

Applications in areas such as photonics, antennas, imaging and optics require the control of propagation of electromagnetic waves and the control of emission of electromagnetic radiation. Achievements in three key research fields may provide the answer to these problems. These emerging research fields are metamaterials, photonic crystals and surface plasmons. This thesis will be about our work on metamaterials and photonic crystals. Metamaterials are a new class of artificial structures whose electromagnetic response can be described by effective permeability and permittivity functions that may attain negative values. I will present our results on the properties of a metamaterial structure that we proposed recently, the labyrinth structure. I will demonstrate that the labyrinth structure can be used to design a medium that exhibits negative permeability values within a certain frequency range. Moreover, I will explore the possibility of negative refraction and sub-wavelength focusing of electromagnetic waves by two and three-dimensional labyrinth structure based left-handed mediums. Novel applications such as metamaterial based compact size antennas, ultra-small high-Q cavities will be also discussed. Another type of artificial electromagnetic structures are the photonic crystals. Photonic crystals can be described by a periodic modulation of the permittivity and/or the permeability of a medium. I will discuss two phenomena arising from the dispersion properties of photonic crystals and their possible applications. One of these phenomena is the existence of surface-bound electromagnetic modes and the other is the negative refraction effect. I will further show that the surface-bound modes can be used for applications such as beaming of electromagnetic waves and enhancement of transmission through sub-wavelength apertures. In addition, I will demonstrate that the negative refraction effect can be utilized to focus electromagnetic waves emitted from a finite size source.

Keywords: Metamaterial, photonic crystal, labyrinth structure, plasma frequency, negative refraction, sub-wavelength focusing, surface mode, beaming, enhanced transmission .

ÖZET

ELEKTROMANYETİK DALGALARIN YAYILMASININ KONTROLÜNDE YENİ YÖNTEMLER: METAMALZEMELER VE FOTONİK KRİSTALLER

İrfan Bulu

Fizik, Doktora

Tez Yöneticisi: Ekmel Özbay

Mart, 2007

Fotonik, antenler, görüntüleme ve optik gibi bir çok uygulama alanı elektromanyetik dalgaların yayılmasının ve salınmasının kontrolünü gerektirmektedir. Üç anahtar alanda kaydedilen gelişmeler bu problemlerin yanıtı olabilir. Bu yeni araştırma alanları metamalzemeler, fotonik kristaller ve yüzey plazmonlarıdır. Bu tez benim metamalzemeler ve fotonik kristaller hakkında gerçekleştirdiğim çalışmalar üzerine yoğunlaşacaktır. Metamateryaller insan eli ile üretilen ve doğada benzeri bulunmayan ve doğal olarak karşılaştığımız malzemelerden farklı elektromanyetik özellikler gösteren yapılardır. Bu yeni tür malzemeler belli bir frekans aralığında negatif permitivite ve permeabilite özellikleri gösterebilmektedir. Tezimin ilk kısmını önermiş olduğumuz labirent metamalzemesine ayıracağım. Labirent yapısını kullanarak belli bir frekans aralığında negatif permeabilite değerlerinin elde edilebileceğini göstereceğim. İki ve üç boyutlu labirent tabanlı yapıları kullanarak negatif kırınım, dalgaboyu altı odaklama gibi metamateryal uygulamalarını inceleyeceğim. Yine metamalzemeler gibi yapay bir malzeme olan fotonik kristaller etrafında iki önemli etki hakkında yaptığımız çalışmalardan bahsedeceğim. Bahsedeceğim bu iki fenomen yüzeye bağımlı elektromanyetik modların varlığı ve negatif kırınım etkisi olacak. Bu iki fenomen etrafında odaklama ve dalga demeti oluşturma gibi uygulamaları göstereceğim.

Anahtar sözcükler: Metamalzeme, fotonik kristal, labirent yapısı, plazma frekansı, negatif kırılma, dalga-boyu altı çözümleme, yüzey modu.

Acknowledgement

I would like to express my gratitude to my supervisor Prof. Dr. Ekmel Özbay for his support and friendship during both my undergraduate and graduate years.

I would like to express my special thanks and gratitude to my friend and colleague Hümeýra Çađlayan.

I would like express my gratitude to my friend Ertuđrul Çubukçu.

I would like to thank my group friends for a warm environment filled with friendship and encouragement.

There are so many people that I want to thank, but before all else I feel in great debt towards my teachers.

Finally, I would like to thank my family. No word can express my gratitude for them.

Fun is over once you discover it.

Contents

1	Introduction	1
2	Metamaterials	3
2.1	Introduction	3
2.1.1	Negative Permittivity?	3
2.1.2	Negative Permeability?	9
2.1.3	Properties and Applications of Metamaterials	14
2.2	The Labyrinth Structure	18
2.2.1	Properties of the labyrinth structure with respect to different orientations	27
2.2.2	Effective permittivity and permeability of the labyrinth structure	30
2.2.3	Composite medium of labyrinth structures and thin wires	33
2.3	Sub-wavelength Focusing	37
2.4	Transmission, refraction, and focusing properties of a three dimensional structure	45

2.5	Sources Inside Metamaterials	48
2.6	Compact size highly directional antennas based on SRR metamaterial medium	56
2.6.1	Properties of the split-ring resonator	56
2.6.2	Near field distribution of the electric field emitted from a source that is embedded inside a SRR based medium	65
2.6.3	Angular distribution of electric field emitted from a source that is embedded inside the metamaterial medium	66
3	Photonic Crystals	73
3.1	Introduction	73
3.2	Beaming of Light and Enhanced Transmission via Surface Modes of Photonic Crystals	75
3.2.1	Theoretical and Experimental demonstration of Surface Propagating Modes	76
3.2.2	Enhanced Transmission Through PC Waveguide via Surface Modes	82
3.2.3	Beaming of EM Waves by Photonic Crystal Surface Modes	84
3.2.4	Conclusion	88
3.3	Negative Refraction and Focusing of Electromagnetic Waves by Metallodielectric Photonic Crystals	89
3.3.1	The Metallodielectric Photonic Crystal	91
3.3.2	Negative Refraction of Electromagnetic Waves by Metallodielectric Photonic Crystal	94

3.3.3	Focusing of Electromagnetic Waves	102
4	Related Work	109
4.1	Content-Based Retrieval Systems	109
4.2	Visual Query Languages and Interfaces	109
4.3	Presenting Results and Design Guidelines	109
5	Conclusions and Future Work	110
A	Publications in SCI journals	129
B	Conference Proceedings	133

List of Figures

2.1	The periodic array of thin wires. The lattice constant is a and the radius of the wires is r	5
2.2	Plasma frequencies of one wire (a), plasma frequencies of two wires (b), and plasma frequencies of three wires (c) as a function of the wire width.	8
2.3	The split-ring structure.	11
2.4	A medium that is composed of periodic arrangement of split-ring structures.	13
2.5	a) When both ϵ and μ are positive, the vectors form a right-handed coordinate system b) When both ϵ and μ are negative, the vectors form a left-handed coordinate system.	15
2.6	Electromagnetic waves, emitted from a horn antenna, are incident on a left-handed slab.	17
2.7	a) Schematics of the labyrinth structure. $r_1 = 1.35$ mm, $r_2 = 1.8$ mm, $r_3 = 2.25$ mm, $r_4 = 2.7$ mm, $g = 0.15$ mm, $w = 0.3$ mm, and $d = 0.15$ mm. b) The unit cell of the actual, fabricated structure and the coordinate system that we use throughout this section. . .	20
2.8	The vector network analyzer: HP8510C.	21

2.9	a) Measured transmission through a single labyrinth structure (A), a single closed labyrinth structure (B). Calculated transmission through a single labyrinth structure (C), a single closed labyrinth structure (D). b) Induced surface current density at 6.2 GHz. c) Measured (E) and calculated (F) transmission through a single labyrinth structure. d) Induced surface current density at 6.2 GHz.	23
2.10	a) Measured transmission spectrum of the z-component of the electric field through (A) the labyrinth metamaterial medium and (B) through the closed labyrinth metamaterial medium. Only the z-component of the incident electric field was nonzero. b) Measured transmission spectrum of the x-component of the electric field through (C) free space and through (D) the labyrinth metamaterial medium. Only the z-component of the incident electric field was nonzero.	24
2.11	a) Orientation 1, b) Orientation 2.	28
2.12	a) Transmission spectrum of four-ring single labyrinth structure with respect to orientations 1 and 2, b) Transmission spectrum of two-ring single labyrinth structure with respect to orientations 1 and 2.	29
2.13	Transmission spectrums of 5 layers of labyrinth based LHM medium with respect to orientations 1 and 2.	30
2.14	a) real part of the effective permeability for a single layer of the labyrinth structure, b) imaginary part of the effective permeability for a single layer of the labyrinth structure.	32
2.15	Real part of the effective permittivity for a single layer of the labyrinth structure.	33
2.16	A layer of the composite structure. Wires are printed on the back and labyrinth are printed on the front of the printed circuit board.	34

2.17	a) Transmission spectrum of electromagnetic waves through the wire medium. b) Measured transmission spectrum of electromagnetic waves through the CMM medium. c) Measured transmission spectrum of electromagnetic wave through the closed CMM medium.	35
2.18	a) The labyrinth structure: $r_1 = 1.35$ mm, $r_2 = 1.8$ mm, $r_3 = 2.25$ mm, $r_4 = 2.7$ mm, $g = 0.15$ mm, $w = 0.3$ mm, and $d = 0.15$ mm. b) Unit cell of the two-dimensional labyrinth based left-handed metamaterial.	38
2.19	a) Phase differences between the ends of isotropic FR4 slabs (dashed curves) and the labyrinth based metamaterial (solid curves) b) Calculated indices of refraction for the labyrinth based metamaterial. (inset: measured transmission spectrum through the labyrinth based composite metamaterial medium (solid-curve) and the simulated transmission spectrum (dotted-curve).)	40
2.20	The measurement setup. The setup consists of HP8510C, two monopole antennas and a two-dimensional linear stage.	41
2.21	Measured electric field intensities on the output side of the metamaterial when the source was 2 cm away (a) and 1 cm away (b) from the input surface of the metamaterial.	42
2.22	Measured intensity profile of the source monopole antenna along the x axis in free space when it was placed 2 cm away from the receiver antenna (A) 8 cm away from the receiver antenna (B). Measured intensity profile along the x axis on the output side of the metamaterial when the source was placed 2 cm away (C) and 1 cm away (D) away from the input surface of the metamaterial.	43
2.23	a) The photographs of the three dimensional structure. b) The measured transmission spectrum of TE and TM polarized waves through the labyrinth based three dimensional left-handed structure.	46

2.24	a) The measured electric field intensities for the incidence angle of 30 degrees. b) The measured electric field intensities for the incidence angle of 15 degrees.	47
2.25	a) The measured electric field intensities for a source distance of 15 mm. b) The measured electric field intensities for a source distance of 5 mm.	48
2.26	The calculated effective medium parameters of the labyrinth-based left-handed medium: real part of the ϵ (- -) and real part of the μ (-). The measured reflection spectrum from the labyrinth-based left-handed medium (...).	49
2.27	Top panel: The simulated field intensity emitted from a source placed inside the homogeneous left-handed medium. Bottom panel: The cross section of the field intensity along the x-axis on the source plane.	51
2.28	a) The measured field intensity when the source was placed 3 layers away from the interface inside the labyrinth-based left-handed medium. b) The measured field intensity when the source was placed 7 layers away from the interface inside the labyrinth-based left-handed medium.	54
2.29	The SRR structure. Following dimensions are used through out our experiments and simulations: $g=0.2$ mm, $d=0.2$ mm, $w=0.9$ mm, $r1=3.6$ mm, $r2=1.6$ mm. Arrows indicate the direction of current flowing around the structure.	57
2.30	Surface current density along the SRR structure at the resonance frequency.	58
2.31	Simulated electric field distribution within the unit cell of the SRR metamaterial medium. Incident planewave has a unit amplitude. View angle is tilted for better visualization.	59

2.32	This setup was used to determine the resonance of a single split-ring resonator.	60
2.33	Measured transmission spectrum of (A) SRR structure, (B) closed SRR structure. Simulated transmission spectrum of (C) SRR structure, (D) closed SRR structure.	61
2.34	Experimental setup that we used to measure the transmission properties of the SRR metamaterial medium. The setup consists of transmitting-receiving horn antennas and HP-8510C network analyzer.	62
2.35	Transmission spectrum of the electromagnetic waves through the SRR metamaterial medium. Electric field is oriented along z-axis and the magnetic field is perpendicular to the plane of the SRR structures.	63
2.36	Real part of the effective permeability for the split-ring resonator based medium that we used in our study.	64
2.37	a) Measured electric field intensity near the surface of the SRR array at 3.8 GHz when the source is located inside the array b) measured electric field intensity near the surface of the SRR array at 4.7 GHz when the source is located inside the array.	65
2.38	a) Far field radiation pattern in the H-plane near the resonance frequency of the SRR structure. b) Far field radiation pattern in the H-plane at an off resonance frequency. Frequency for this plot is 4.7 GHz.	68
2.39	a) Far field radiation pattern in the E-plane near the resonance frequency of the SRR structure. b) Far field radiation pattern in the E-plane at an off resonance frequency. Frequency for this plot is 4.7 GHz.	69

2.40	a) Far field radiation pattern in the H-plane from a source embedded inside CRR array near the resonance frequency of the SRR structure. b) Far field radiation pattern in the H-plane from a source embedded inside CRR array at 4.7 GHz.	70
2.41	a) Far field radiation pattern in the E-plane from a source embedded inside CRR array near the resonance frequency of the SRR structure. b) Far field radiation pattern in the E-plane from a source embedded inside CRR array at 4.7 GHz.	71
2.42	Measured S11 for the monopole source in free space (red curve) and for the monopole when the source is located inside the SRR array (blue curve).	72
3.1	The layer-by-layer photonic crystal. This structure is described the face cubic tetragonal lattice (FCT).	74
3.2	a) The TM (electric field parallel to the axis of the rods) band structure of the infinite size PC b) the TM band structure of the finite size c) the TM band structure of the finite size PC when the radius of the rods at the surface of the PC is reduced to 0.76 mm. d) zoomed view of the TM band structure of the finite size PC when the radius of the rods at the surface of the PC is reduced to 0.76 mm.	77
3.3	Modes of the finite size PC a) electric field profile of mode extending both in air and PC b) electric field profile of mode extending in air but decaying in PC c) electric field profile of mode decaying in air but extending in PC d) electric field profile of surface mode	79
3.4	The photonic crystal structure that we used in the study of surface modes.	81

3.5	Measured reflection spectrum from (A) bare photonic crystal surface (B) from the corrugated layer added PC surface (C) from the corrugated PC surface when the grating-like structure is added . . .	82
3.6	A) The measured transmission spectrum through the PC waveguide, B) the calculated transmission spectrum through the PC waveguide, C) the measured transmission spectrum through the PC waveguide when the surface corrugation and the grating-like structure is added in front of the input surface of the PC waveguide, C) the calculated transmission spectrum through the PC waveguide when the surface corrugation and the grating-like structure is added in front of the input surface of the PC waveguide	83
3.7	The measured intensity distribution at the exit side of the PC waveguide. Y-axis is parallel to the PC surface.	85
3.8	Calculated field intensity when the surface corrugation is added to the exit surface of the PC waveguide.	86
3.9	The measured intensity distribution at the exit side of the PC waveguide when the corrugation and grating-like layer are added to the exit surface of the PC waveguide. Y-axis is parallel to the PC surface.	86
3.10	a) Measured far field radiation pattern of the EM waves emitted from PC waveguide at 12.45 GHz b) Measured far field radiation pattern of EM waves emitted from the PC waveguide with surface corrugation and grating-like layer	88
3.11	The first 3 TM polarized bands for (a) the metallic photonic crystal (b) the metallodielectric photonic crystal (c) the unperturbed dielectric photonic crystal (d) the perturbed dielectric photonic crystal.	90

- 3.12 Equal frequency contours, solid curves, are shown for the metal-
 lodielectric photonic crystal. Crystal orientation is shown by the
 dashed line. Dotted circle represents the free space equal frequency
 contour at 9.5 GHz. Frequencies are shown in the GHz scale. Long
 dashed arrow with black color represents the free space wave vec-
 tor whereas the short black arrow represents the free space group
 velocity. Long dashed arrow with white color represents the wave
 vector of the refracted waves in photonic crystal. Small white col-
 ored arrow indicates the direction of group velocity inside photonic
 crystal. 92
- 3.13 a) Electric field distribution for incidence angle 15° b) Electric field
 distribution for incidence angle 45° . Black represents the maximum
 field amplitude, whereas white color represents the minimum field
 amplitude. 95
- 3.14 Experimental setup for negative refraction measurement. Electric
 field intensities are measured along the surface of the photonic
 crystal (shown by the dashed line) by a monopole receiver. Origin
 of the coordinate system is the middle of the surface. Source is a
 horn antenna. Incidence direction is represented by the arrow. . . 96
- 3.15 Measured electric field intensities along the surface of the photonic
 crystal are shown for incidence angles of (a) 15° (b) 25° (c) 35° (d)
 45° . Incidence direction is shown by the arrow. Black represents
 the maximum field intensity, whereas white color represents the
 minimum field intensity. 97
- 3.16 Measured and calculated indices of refraction between 9 GHz and
 10 GHz at 15° incidence angle. Solid curve represents the experi-
 mental data and the dashed curve represents the theoretical indices
 of refraction obtained from FDTD simulations. 99
- 3.17 a) Electric field intensity for 9 GHz. b) Electric field intensity for
 9.7 GHz. Incidence angle is 25 degrees. 101

3.18	A simple illustration of the focusing effect.	102
3.19	a) Electric field distribution from a monopole source placed in front of the metallodielectric PC. Black represents the maximum field amplitude, whereas white color represents the minimum field amplitude. b) Electric field intensity along the dashed-line c) Electric field intensity along the dotted-line	103
3.20	(a) Experimental setup for focusing measurement. Both the receiver and the source are monopole antennas. Electric field intensities are measured along the direction shown by the arrow. (b) Electric field intensities for when the source is placed 11 cm away from the photonic crystal. Black represents the maximum field intensity, whereas white color represents the minimum field intensity. (c) Measured and calculated electric field intensities at 9.7 GHz	104
3.21	(a) Electric field intensities measured at a distance of 13 cm away from the surface of the photonic crystal. Measurement direction is along the surface of the photonic crystal. Measurement is performed at 9.7 GHz.	106
3.22	Measured electric field intensity at the output side of the metallodielectric photonic crystal. The source monopole was placed on the other side of the photonic crystal. The distance of the source monopole antenna to the input surface of the metallodielectric photonic crystal was 11 cm.	108
5.1	Relative spontaneous emission rate of a point dipole when it is placed in front of a left-handed structure. The term "relative" refers to the spontaneous emission rate in free space.	111
5.2	S11 response of a finite size dipole when it is placed in free space and when it is placed in closed vicinity to a left-handed material.	112

5.3 a)Transmission through negative permeability medium when a local perturbation is introduced to the structure. b)Transmission through negative permeability and negative permittivity medium when a local perturbation is introduced to the structure. 114

5.4 Off-axis beaming of electromagnetic waves by utilizing surface modes.116

List of Tables

Chapter 1

Introduction

Three key research fields are attracting a great deal of attention in these recent years: photonic crystals, metamaterials and surface plasmon phenomenon. The basic reason behind this interest is the fact that these structures provide means to control the propagation of electromagnetic waves. In addition, these structures may play a key role in controlling the emission properties of electromagnetic wave sources. Photonic crystals are already being used in some commercial applications such as light emitting diodes (by Samsung) [1], gas and chemical sensing [2], fibers [3] and lasers [4]. Moreover, A great deal of applications based on surface plasmons have been suggested such as optical detection [5], mass-spectroscopy [6], optical-heads for data recording [7] and many more. In fact, a search on the US patent database about surface plasmons returned 1745 counts (As of February 2007). On the other hand, the field of metamaterials is a relatively new research topic. Although metamaterials is a relatively new field, it is attracting a great deal of attention. There are already 34 US patents issued for metamaterial based applications. The fundamental reason for this interest in metamaterials is that these structures can be designed to have permittivities and permeabilities with almost any values including negative ones. This possibility of negative permittivities and permeabilities lead to some exciting conclusions such as the negative refraction [8], inverse doppler shift [9], superlensing [10] and many more... In

addition, the ability to design a medium with desired permittivity and permeability values lead to some interesting applications such as resonant antennas [11], phased array antenna systems [12], active THz devices [13]....

I will briefly summarize my work on metamaterials and photonic crystals in this thesis. Second chapter will be devoted to metamaterials with a brief introduction to the theory and properties of metamaterials. This chapter will first introduce the labyrinth structure, a metamaterial structure that we proposed. We will first investigate the properties of the labyrinth structure. We will show that the labyrinth structure has strong magnetic response and it can be used to create a medium that has negative effective permeability within a certain frequency range. The remainder of the chapter will be devoted to the applications of labyrinth and split-ring resonator based metamaterials. These applications include sub-wavelength focusing, directive radiation sources and the properties of sources inside metamaterials. Chapter 3 will be about my work on photonic crystals. This chapter will include two very interesting phenomena and their applications. The first of these phenomena is the existence of bound modes at the surface of a modified photonic crystal structure. I will demonstrate that these surface-bound modes can be utilized in certain applications such as beaming and enhanced transmission through sub-wavelength apertures. Chapter 3 will conclude with another phenomenon arising from the dispersion properties of photonic crystals: negative refraction effect. Chapter 4 will be about further work that I find interesting from an application point of view and also for basic studies.

Chapter 2

Metamaterials

2.1 Introduction

The possibility of the negative refraction of electromagnetic (EM) waves by materials with simultaneous negative permittivity and negative permeability was predicted by Vesalago in 1968 [14]. This proposition was not demonstrated until recently; the main difficulty being in obtaining negative permeability. Negative permittivity is available through metals or the periodic arrangement of metallic wires [15, 16, 17]. On the other hand, obtaining negative permeability was an issue. Pendry et al. proposed several structures in order to obtain negative permeability [18].

2.1.1 Negative Permittivity?

In this section, we will revisit the electromagnetic properties of an artificial medium that is composed of a periodic arrangement of thin conducting wires. Such a medium may be regarded as a metallic photonic crystal [15]. However, the electromagnetic properties of a periodic arrangement of wires can also be explained in terms of effective permittivity function. An exciting interpretation and justification for the use of effective permittivity was suggested by Pendry [16, 19].

The dielectric function of an ideal electron plasma is given by:

$$\varepsilon_{plasma} = 1 - \frac{\omega_p^2}{\omega^2} \quad (2.1)$$

where ω_p , plasma frequency, is directly proportional to the electron density and inversely proportional to the effective electron mass,

$$\omega_p^2 = \frac{ne^2}{\varepsilon_0 m_e}. \quad (2.2)$$

This function may be expanded by adding a damping term to describe the dielectric function of real metals:

$$\varepsilon_{plasma} = 1 - \frac{\omega_p^2}{\omega(\omega + i\tau)}. \quad (2.3)$$

A similar equation can be used for a medium of periodic arrangement of thin wires, Fig. 2.1, by taking the effects of confining electrons to move inside finite cylinders into account. Such a constraint has two effects: (1) reduced electron density and (2) enhancement of effective mass. But let us first consider the Lagrangian density for an electron plasma and photons when electromagnetic fields are acting on the medium:

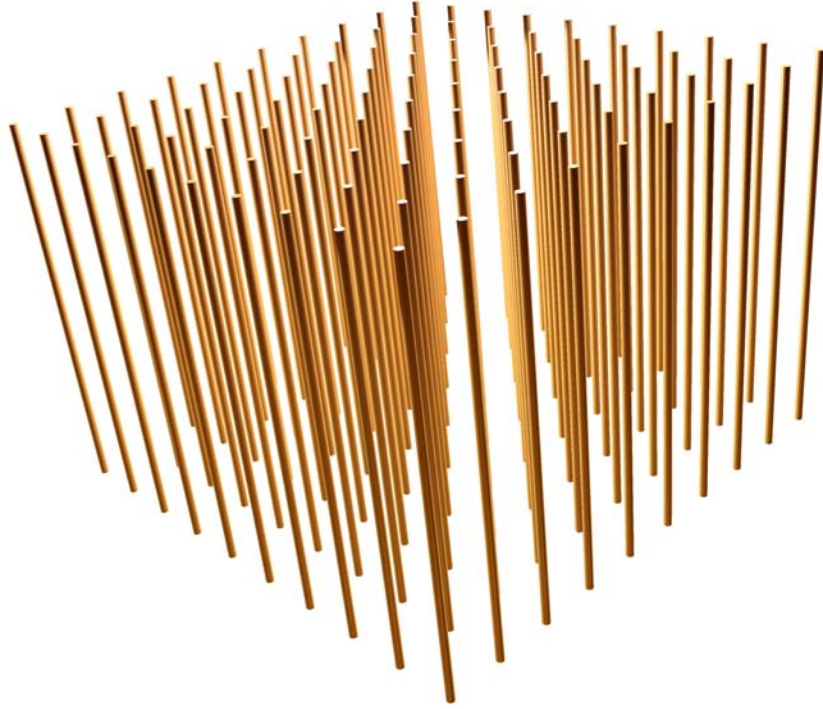


Figure 2.1: The periodic array of thin wires. The lattice constant is a and the radius of the wires is r .

$$L = -1/4 F_{\mu\nu} F^{\mu\nu} - \frac{1}{\varepsilon_0 c^2} \rho \phi + \mu_0 \mathbf{J} \cdot \mathbf{A} \quad (2.4)$$

where $F^{\mu\nu}$ is the electromagnetic field tensor, \mathbf{J} is the current density, ρ is the charge density, and \mathbf{A} is the vector potential. The components of the canonical momentum of the field are then:

$$\pi_\mu = \frac{\partial L}{\partial \dot{A}_\mu} \quad \pi(x) = -E(x). \quad (2.5)$$

Since $\mathbf{E} = -\partial\mathbf{A}/\partial t$ and $m\dot{\mathbf{v}} = -e\mathbf{E}$, we can write the canonical momentum as $m_e\mathbf{v} + e\mathbf{A}$. Note that the canonical momentum is conserved. Hence, $m_e\mathbf{v} = -e\mathbf{A}$.

We shall now calculate the vector potential \mathbf{A} . We will assume long wavelength limit, that is the wavelength is much larger than the periodicity of the

wire medium, while carrying out the calculation. In this approximation, current is confined to very thin wires. In addition, \mathbf{D} is uniform through out the medium. Another line of approximation follows by replacing each unit cell with a circle of the same area. If the lattice constant is a then the radius of the circle becomes $R = a/\sqrt{\pi}$. We assume that the contribution from other cells is negligible. While this approximation may sound very coarse, it is justified if the radius of the actual current carrying wires is small compared to the wavelength. We can now write down the magnetic field:

$$H = \frac{j}{2\pi r} - \frac{jr^2}{2\pi r R^2} \quad 0 < r < R$$

$$H = 0 \quad r > R \quad (2.6)$$

The vector potential can be derived from the above equation:

$$A = \frac{\mu j}{2\pi} \left[\ln\left(\frac{r}{R}\right) - \frac{r^2 - R^2}{2R^2} \right] \quad 0 < r < R$$

$$A = 0 \quad r > 0 \quad (2.7)$$

This equation may be approximated at the wire position as:

$$A \approx \frac{\mu_0 c}{2\pi} \ln(r/a) \quad (2.8)$$

Since the mechanical momentum is equal to $-e\mathbf{A}$, then the momentum density for the per unit length of the wire is:

$$j = nev \quad (2.9)$$

$$P = \frac{\mu_0 e^2 \pi^2 r^4 n^2 v}{2\pi} \ln(a/r) \quad (2.10)$$

We can now assign an effective electron mass, which is:

$$m_{eff} = \frac{\mu_0 e^2 \rho}{2\pi} \ln(a/r) \quad (2.11)$$

In addition to enhanced effective electron mass, the effective electron density is reduced:

$$\rho_{eff} = \rho \frac{\pi a^2}{d^2} \quad (2.12)$$

Using eqns. 2.11 and 2.12, we can write the plasma frequency, ω_p as:

$$\omega_p^2 = \frac{\rho e^2}{\varepsilon_0 m} = \frac{2\pi c_0^2}{a^2 \ln(a/r)} \quad (2.13)$$

We calculated the plasma frequency of thin copper wires by using the above formula and by using a fullwave solver. The results for various configurations of wires are plotted in Fig. 2.2. Both results agree quite well.

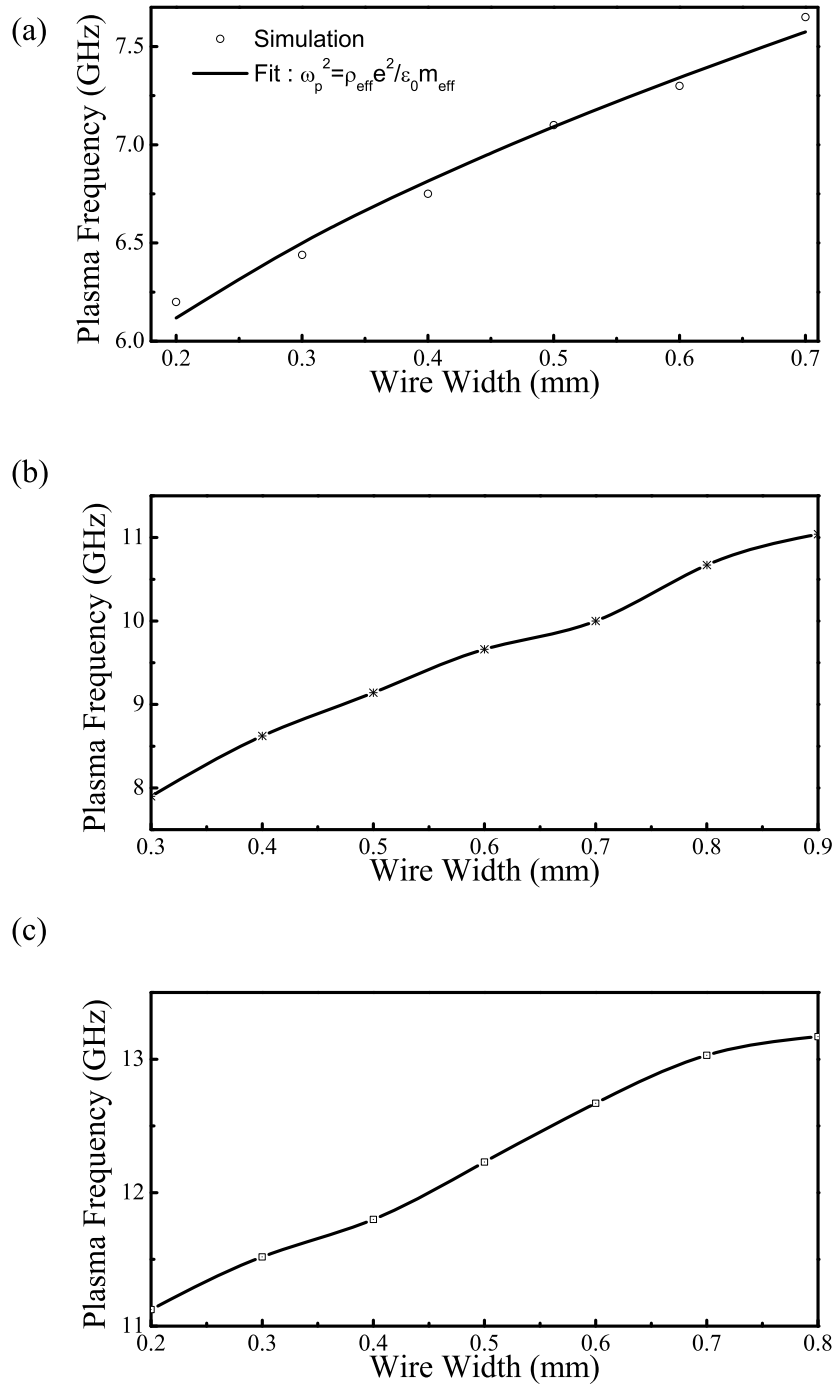


Figure 2.2: Plasma frequencies of one wire (a), plasma frequencies of two wires (b), and plasma frequencies of three wires (c) as a function of the wire width.

This simple model has been improved by several researchers [20]. Another approach makes use of the circuit theory and models the periodic wire medium as a collection of coupled inductors [21].

2.1.2 Negative Permeability?

In the previous section, it was shown that a periodic array of thin wires acts as a plasma and the resulting medium can be described in terms of an effective permittivity function. We will provide a brief summary of the properties of the structures that are proposed to yield negative permeability values. While several researchers proposed different structures for the purpose of negative permeability, probably the most common feature of these structures is the fact that they are based on resonance phenomena. Simply put, in order to have magnetic response, the underlying elements need to have non-zero magnetic dipole moment. But, it is well-known that the magnetic response of naturally occurring materials is small at high frequencies. This suggests that we can not make use of the magnetic dipole moment of the molecules or atoms. Hence, we need to create our magnetic dipoles. A current carrying loop has a magnetic dipole moment. As a matter of fact, a medium composed of small conducting rings is diamagnetic; a simple result of the Lenz Law. A comparison with the effective dielectric response of a medium that is composed of harmonic oscillators provides the necessary clue. The equation of motion for an electron bound by harmonic force can be written as:

$$\ddot{\mathbf{x}} + \gamma\dot{\mathbf{x}} + \omega_0^2\mathbf{x} = -e/m\mathbf{E}(\mathbf{x}, t) \quad (2.14)$$

Assuming a harmonic time dependence of the electric field this equation yields the following result for the electric dipole moment in the small amplitude limit:

$$\mathbf{p} = -e\mathbf{x} = \frac{e^2}{m}(\omega_0^2 - \omega^2 - i\omega\gamma)^{-1}\mathbf{E} \quad (2.15)$$

If there are N molecules per unit volume then the dielectric function is:

$$\epsilon(\omega) = 1 + \frac{Ne^2}{\epsilon_0 m} (\omega_0^2 - \omega^2 - i\omega\gamma)^{-1} \quad (2.16)$$

The real part of eqn. 2.16 is negative within a certain frequency range. The above argument suggests that we shall try to find a similar system for which the equation of motion for the current density has a similar form to eqn. 2.14. A very basic example of such a system is an LC circuit for which the equation of motion for the current is:

$$\frac{dV}{dt} = R \frac{dI}{dt} + L \frac{d^2 I}{dt^2} + \frac{I}{C} \quad (2.17)$$

So, all we need to do is actually add a capacitance to our conducting ring. Note that the capacitance term in eqn. 2.17 acts as the inertia for this system. This may be achieved by simply adding a cut to the ring.

It was Pendy whom first suggested several structures that might lead to negative permeability when assembled in a periodic arrangement [18]. One of these structures is the split-ring structure, Fig. 2.3 and it is by far the most common structure among researchers [22, 23, 24, 25, 26, 27, 28, 29, 30, 31, 32]. We can derive an approximate equation for the effective permeability of a medium that consists of split-ring structures by using the charge conservation theorem [33]. The geometry of the problem is detailed in Fig. 2.3.

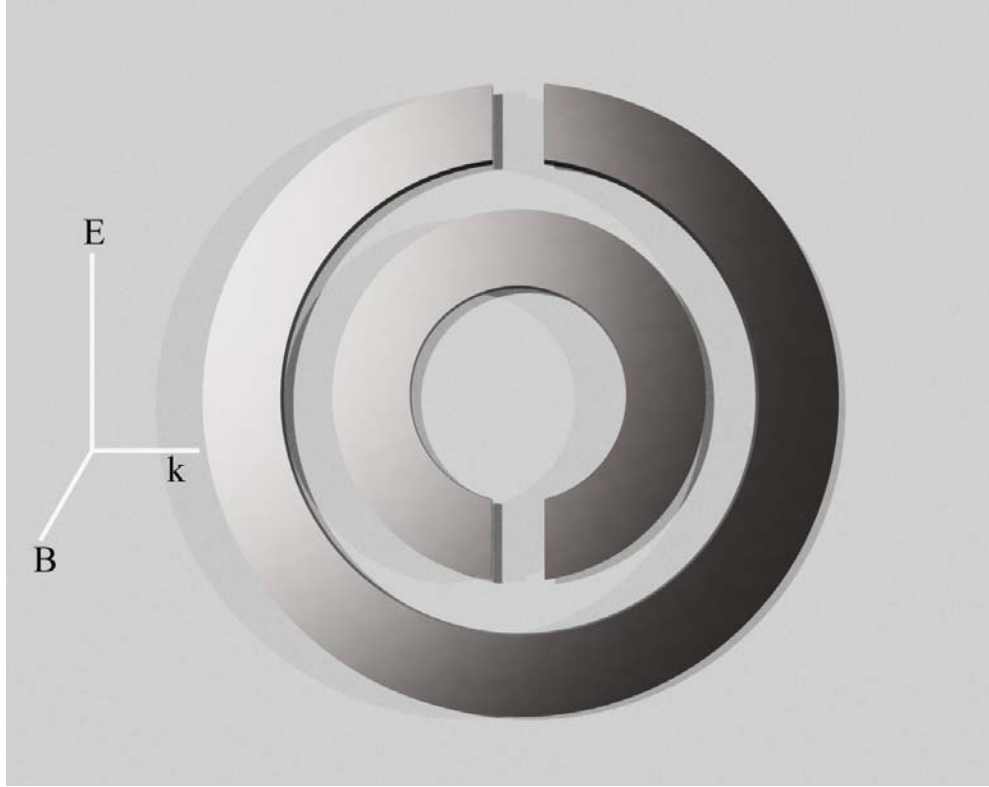


Figure 2.3: The split-ring structure.

$$\nabla \cdot J + \frac{\partial \rho}{\partial t} = 0. \quad (2.18)$$

Which leads to:

$$\begin{aligned} \frac{dI_1}{r_0 d\phi} &= -\frac{dq_1}{dt} = -i\omega C(V_1 - V_2) \\ \frac{dI_2}{r_0 d\phi} &= -\frac{dq_2}{dt} = -i\omega C(V_2 - V_1) \end{aligned} \quad (2.19)$$

where I_1 is the current flowing in the first ring, q_1 is the per unit length charge on the first ring, and C is the capacitance per unit length between the rings. Note that the derivative of the current is carried out with respect to the angle ϕ . The electromagnetic waves are incident on the structure such that the magnetic field is

perpendicular to the plane of the split-ring structure. As a result an electromotive force of $\varepsilon = -i\omega\pi r_0^2 B^{ext}$ is induced along the rings. We can write the potential difference in eqn. 2.19 as:

$$V_1 - V_2 = 2i\omega(LI + \pi r_0^2 B^{ext}) \quad (2.20)$$

assuming that the current density on each ring is uniform we then have:

$$\begin{aligned} I &= 4\pi\omega^2 r_0 C (LI + \pi r_0^2 B^{ext}) \\ I &= \frac{4\pi^2\omega^2 r_0^3 C}{1 - 4\pi\omega^2 LC r_0} B^{ext} \end{aligned} \quad (2.21)$$

Assuming that there are N split-rings per unit volume, then the magnetic moment per unit volume is:

$$M = NI\pi r_0^2 = \frac{F/\mu_0 \frac{\omega^2}{\omega_0^2}}{1 - \frac{\omega^2}{\omega_0^2}} B^{ext}, \quad F = N\pi r_0^2, \quad \omega_0^2 = \frac{1}{4\pi LC r_0} \quad (2.22)$$

Hence, the effective permeability can be written as:

$$\begin{aligned} B^{int} &= \mu_0 \mu_r H^{int} = \mu_r B^{ext} \\ M &= \frac{1}{\mu^0} \frac{\mu_r - 1}{\mu_r} B^{int} \end{aligned} \quad (2.23)$$

$$\mu_r = 1 - \frac{F\omega^2}{\omega^2 - \omega_0^2} \quad (2.24)$$

Equation 2.23 may be expanded to include dissipation by adding an imaginary part:

$$\mu_r = 1 - \frac{F\omega^2}{\omega^2 - \omega_0^2 + i\tau\omega} \quad (2.25)$$

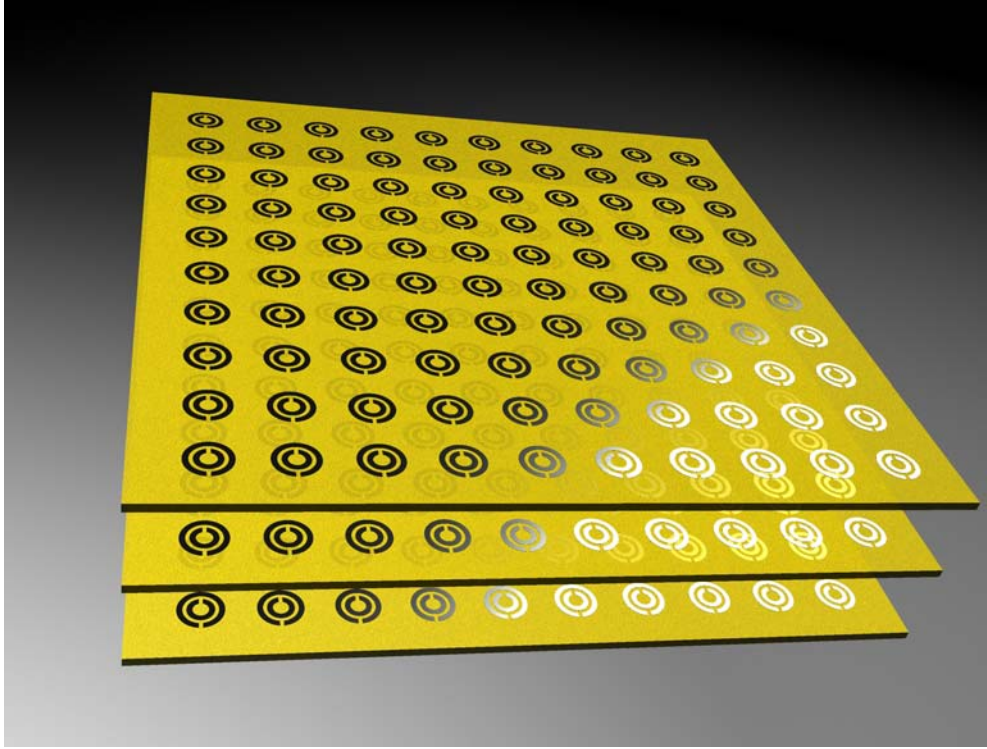


Figure 2.4: A medium that is composed of periodic arrangement of split-ring structures.

This first order approximation clearly demonstrates that the split-ring medium, Fig. 2.4, exhibits negative permeability over a certain frequency range when the electromagnetic field is incident on the structure such that the magnetic field is perpendicular and electric field is parallel to the plane of the split-ring structure. This simple approximation has been improved by several researchers to include higher order effects and magneto-electric coupling [34, 33, 35]. A more general form of constitutive relations are provided in terms of tensors:

$$\begin{aligned}\mathbf{D} &= \epsilon_0\epsilon\mathbf{E} - i\sqrt{\epsilon_0\mu_0}\kappa\mathbf{H} \\ \mathbf{B} &= i\sqrt{\epsilon_0\mu_0}\kappa^T\mathbf{E} + \mu_0\mu\mathbf{H}\end{aligned}\tag{2.26}$$

where:

$$\epsilon = \begin{pmatrix} 1 & 0 & 0 \\ 0 & \epsilon_{yy} & 0 \\ 0 & 0 & \epsilon_{zz} \end{pmatrix}, \mu = \begin{pmatrix} \mu_{xx} & 0 & 0 \\ 0 & 1 & 0 \\ 0 & 0 & 1 \end{pmatrix}, \kappa = \begin{pmatrix} 0 & 0 & 0 \\ \kappa_{yx} & 0 & 0 \\ 0 & 0 & 0 \end{pmatrix} \quad (2.27)$$

I would like to conclude this section by pointing out that the above equation includes the effect of dipolar moments. Investigation of higher order multipoles may lead to some interesting physics.

2.1.3 Properties and Applications of Metamaterials

Let us start to find out the plane wave solutions to the Maxwell equations when both the permeability and the permittivity of a medium are negative. The Maxwell equations in the frequency domain are:

$$\begin{aligned} \nabla \times \mathbf{E} &= -i\omega\mathbf{B} \\ \nabla \times \mathbf{H} &= i\omega\mathbf{D} \end{aligned} \quad (2.28)$$

From eqns. 2.28, we find that the plane wave solutions, $[\mathbf{E}, \mathbf{H}]exp(-i\mathbf{k} \cdot \mathbf{r})$ satisfies the following equations:

$$\mathbf{k} \times \mathbf{E} = \frac{\omega\mu}{c}\mathbf{H}, \quad \mathbf{k} \times \mathbf{H} = -\frac{\omega\epsilon}{c}\mathbf{E} \quad (2.29)$$

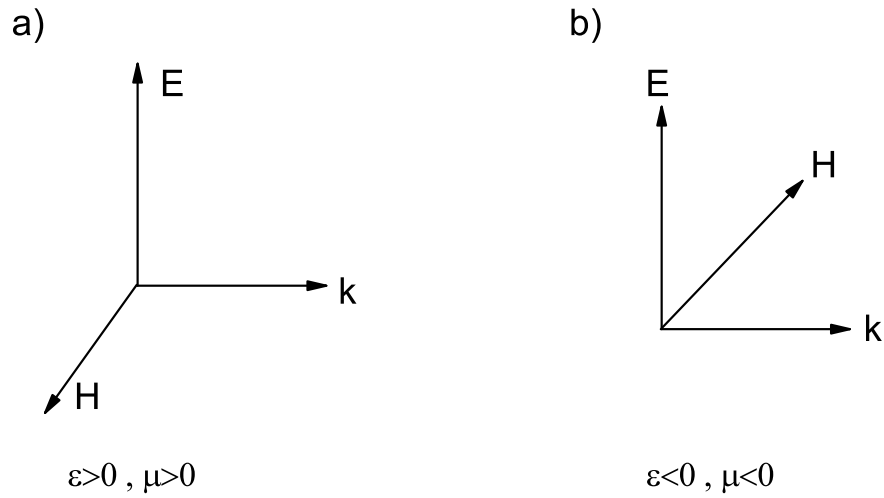


Figure 2.5: a) When both ϵ and μ are positive, the vectors form a right-handed coordinate system b) When both ϵ and μ are negative, the vectors form a left-handed coordinate system.

If both ϵ and μ are negative then eqns. 2.29 show that the wave vector, electric field vector, and magnetic field vector form a left-handed coordinate system, Fig. 2.5. Now let us consider what happens to the direction of Poynting vector, \mathbf{S} . Since \mathbf{S} is independent of the permittivity and permeability,

$$\mathbf{S} = \frac{c}{4\pi} \mathbf{E} \times \mathbf{H} \quad (2.30)$$

we immediately find out that the wave vector and the Poynting vector are antiparallel. As a result, the phase velocity and the group velocity of a plane wave in a left-handed medium are in opposite directions. This result has several prominent effects such as the reversal of Doppler shift [9] or Cherenkov radiation [36].

Another interesting result arises when we consider the transmission of electromagnetic waves from a right-handed medium to a left-handed medium, i.e., the refraction problem. The causality dictates that upon refraction the wave vector of

the transmitted wave and the incident wave are on the different sides with respect to the surface normal vector [14]. Note that if both mediums are right-handed, then the wave vectors of the transmitted wave and the incident wave fall in to the same side with respect to surface normal [37]. We plotted the electric field pattern when the electromagnetic waves that are emitted from a horn antenna are incident on a left-handed slab. The angle of incidence with respect to surface normal is 15 degrees. Note that the phase fronts in the left-handed medium has a direction that is on the opposite side of the surface normal with respect to the direction of the phase fronts of the incident wave.

Several novel applications have been proposed and some demonstrated based on metamaterials. Probably, at this point we shall give a definition of the term metamaterial. Since we are talking about a "material", the term "metamaterial" should be attached to structures whose electromagnetic response can be described in terms of effective medium parameters, such as an effective permittivity and permeability function. Up to this point, we did not mention about the size of the features that make up a metamaterial. In order to be able describe the electromagnetic properties of a medium, the size of the underlying features much be much smaller than a wavelength. In addition, due to the term "meta", these structures should be artificial ones. One of these applications that attracted great attention is the "superlens" [10]. The term "superlens" refers to a slab of metamaterial that is described by $\epsilon = -1$, $\mu = -1$. Pendry suggested that such a slab may resolve the sub-wavelength features of sources without any limitation. Ziolkowski suggested that a double-negative medium, for which the permittivity and permeability are simultaneously negative, may be used to increase to efficiency of antennas [38]. One of the most successful applications of metamaterials has been realized in the field of Magnetic Resonance Imaging (MRI) [39]. The researchers were able to enhance the MRI images significantly by using metamaterials.

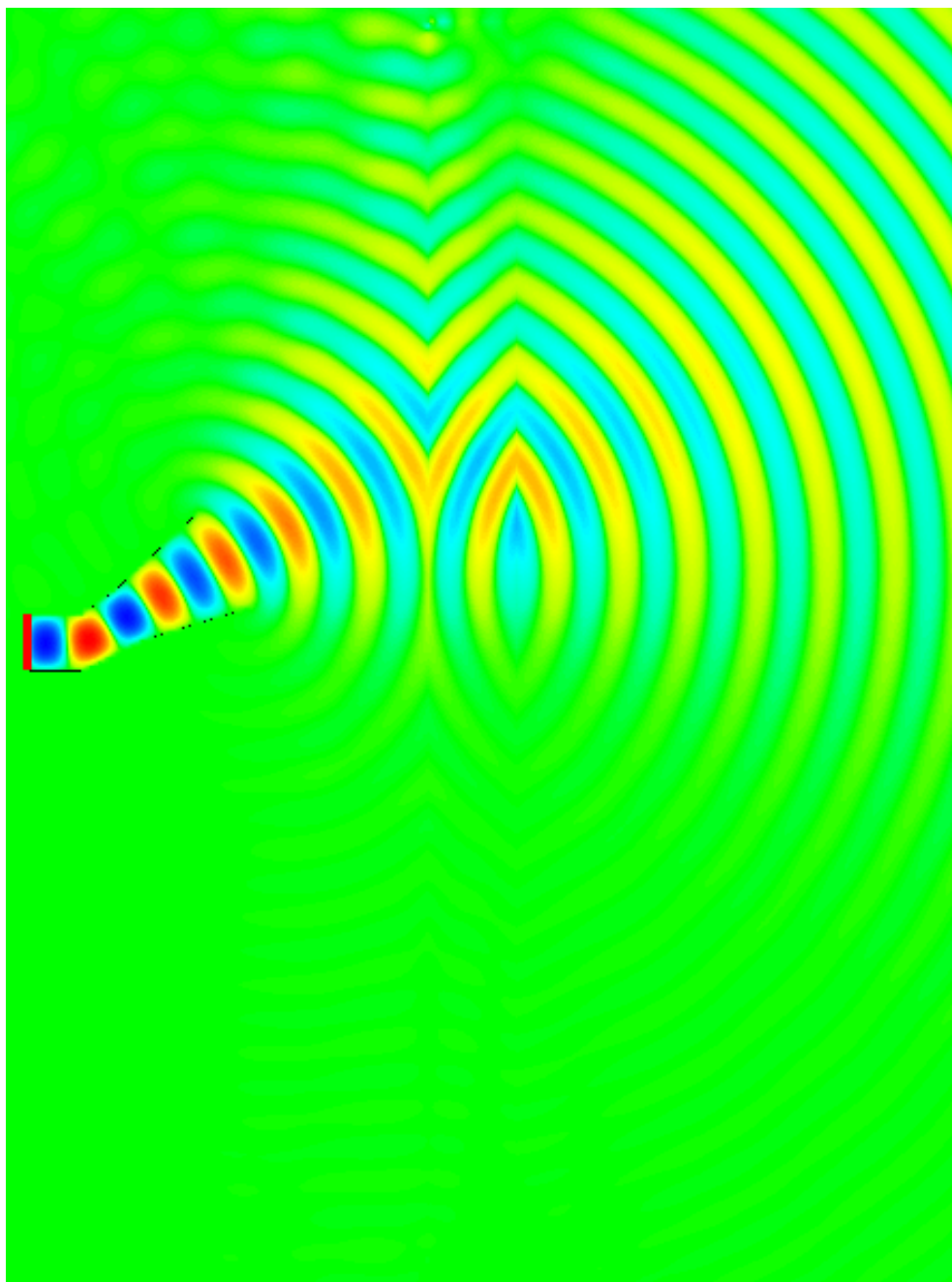


Figure 2.6: Electromagnetic waves, emitted from a horn antenna, are incident on a left-handed slab.

2.2 The Labyrinth Structure

Split-ring structure is commonly used among researchers in order to obtain negative permeability [22, 23, 24, 25, 26, 27, 28, 29, 30, 31, 32]. A single SRR is composed of two concentric rings with slits on each of them. The slits on the rings are situated on the opposite sides of the rings with respect to each other. The planar nature of the SRR structure makes it easy to fabricate and integrate into 2 and 3 dimensional structures. Several research groups have demonstrated negative indices of refraction by using the periodic arrangement of metallic wires with SRRs through several methods such as the retrieval of effective medium parameters [40, 41, 42, 43, 44, 45, 46], refraction type experiments and wedge experiments [8, 47, 48, 49, 50, 51, 52, 53, 54].

While SRR structure provides negative permeability and can be used to obtain negative refraction, it has several disadvantages. First of all, it has been shown that a medium consisting of a periodic arrangement of SRRs is bianisotropic [46, 34, 33]. The bianisotropy is a result of the non-zero electric dipole moment of the SRR structure due to the asymmetric placement of slits on the rings. Second, it has been shown that the magnetic resonance of the SRR structure can be excited via electric fields [55]. The excitation of the magnetic resonance of the SRR structure results from the capacitive coupling of the electric field. The capacitive coupling of the electric field creates non-zero current along the rings. These two disadvantages make it difficult to obtain isotropic, homogeneous two or three dimensional negative refraction media by using SRRs for negative permeability.

When an EM wave is incident on a metamaterial made of a periodic arrangement of SRRs with a wave vector in the plane of SRRs and with a magnetic field perpendicular to the plane of SRRs, the transmitted electric field contains a component that is perpendicular to the plane of SRRs. This extra component arises from the non-zero electric dipole moment induced by the incident magnetic field [55]. The electric dipole moment is non-zero because the currents that flow across each slit do not cancel out the current flowing on the other slit. As a result, the medium is bianisotropic and the constituent relations assume the following

forms [46]:

$$\overline{D} = \overline{\varepsilon} \cdot \overline{E} + \overline{\zeta} \cdot \overline{H} \quad (2.31)$$

$$\overline{H} = \overline{\mu} \cdot \overline{H} + \overline{\zeta} \cdot \overline{E} \quad (2.32)$$

Several researchers have pointed out the bianisotropy issue related to the SRR structure and they have suggested several ways to overcome it [46, 34, 33]. One such way is to place rings with equal radiuses on the opposite sides of the substrate [33]. In this case the currents flowing across the slits are equally balanced and as a result the bianisotropy is greatly reduced. This approach solves the problem related to the SRR metamaterial medium. But if one desires to combine this modified SRR metamaterial medium with a wire medium in order to obtain negative refraction they face a manufacturing problem. The placement of the wires is not obvious in this case. In addition, this approach cannot solve the problem related to the excitation of the magnetic resonance via incident electric waves.

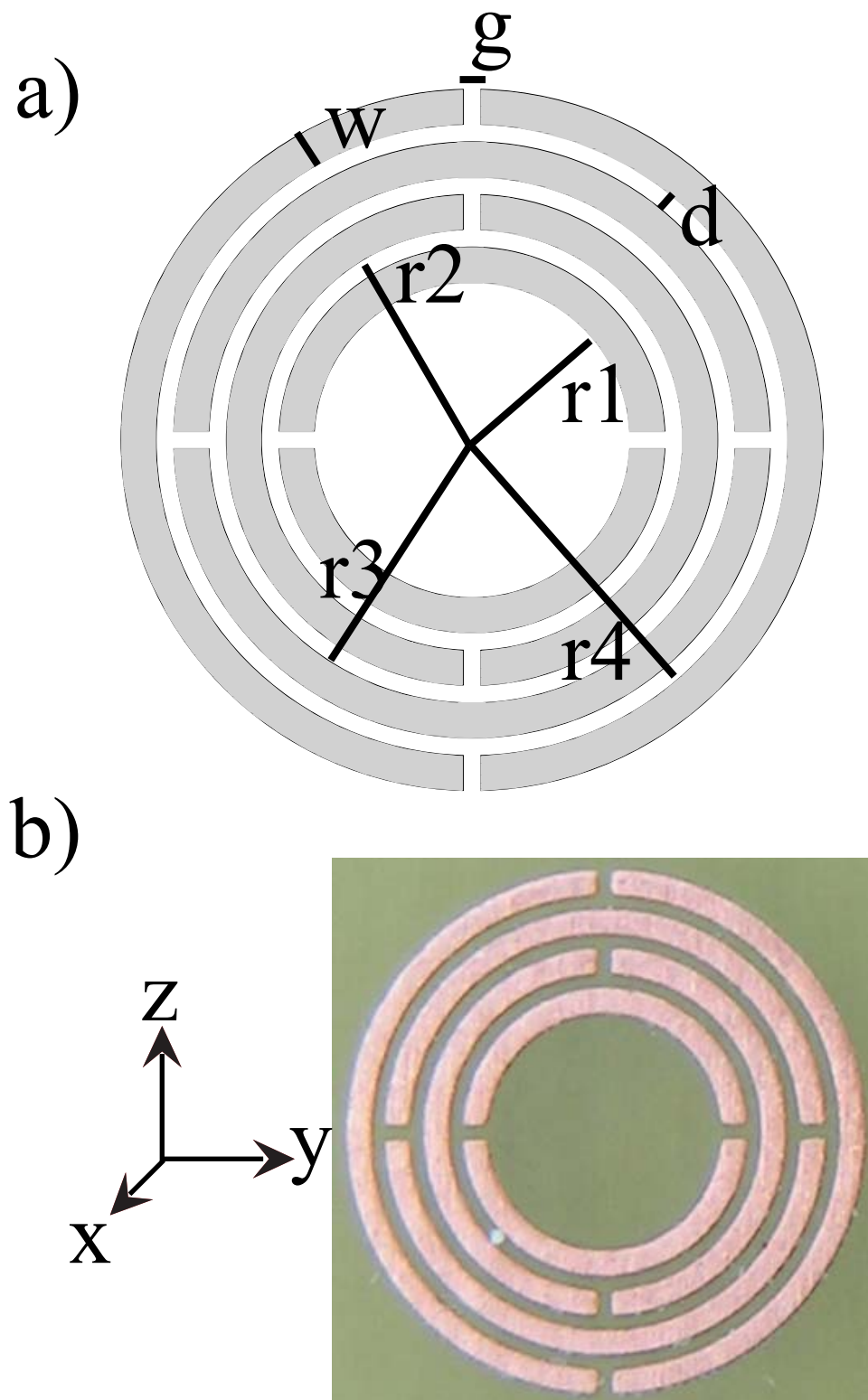


Figure 2.7: a) Schematics of the labyrinth structure. $r_1 = 1.35$ mm, $r_2 = 1.8$ mm, $r_3 = 2.25$ mm, $r_4 = 2.7$ mm, $g = 0.15$ mm, $w = 0.3$ mm, and $d = 0.15$ mm. b) The unit cell of the actual, fabricated structure and the coordinate system that we use throughout this section.

The magnetic resonance of the SRR structures can be excited by incident waves whose electric field is perpendicular to the slits and whose wave vector is perpendicular to the plane of SRRs. Such an incident electric field couples to the magnetic resonance capacitively and induces currents flowing across the rings. The induced currents on both rings are solenoidal, hence they resemble the currents that are induced by incident magnetic fields at the magnetic resonance. The resonance frequency observed due to the capacitive coupling of electric field is quite close to the magnetic resonance. The transmission spectra of the EM waves with magnetic fields perpendicular to the plane of SRRs and with wave vectors in the plane of SRRs are quite close to the transmission spectrum of electromagnetic waves with electric field perpendicular to the slits and with wave vector perpendicular to the plane of SRRs. Hence, the excitation of the magnetic resonance via incident electric fields introduces another problem if one attempts to obtain isotropic and homogeneous negative refraction media by using SRRs and wires.



Figure 2.8: The vector network analyzer: HP8510C.

The above argument suggests that one needs to modify the SRR structure in order to solve the aforementioned problems. The bianisotropy is related to the asymmetric placement of the slits on both rings. The imbalance in the currents on both rings can be remedied by using a more symmetric resonator structure. This can be achieved by adding two slits on both rings and then rotating both of them 90 degrees with respect to each other. Such a placement of rings results in the cancellation of the currents flowing across each slit by the current flowing on the slit that is located on the same ring. In turn, the resultant electric dipole moment due to the currents flowing across the slits is suppressed. The electric coupling to the magnetic resonance can be avoided by using the same structure. In order to avoid electric coupling to the magnetic resonance one must somehow suppress the currents flowing across the rings due to the capacitive coupling of the electric field through the slits. Such suppression can be obtained by creating opposing current flows on the same ring. This argument suggests that one needs to place two slits on the same ring. Since the currents due to capacitive coupling of the electric field on each slit will be opposite to each other, the net current on the ring will be suppressed. As a result, the net magnetic dipole moment will be reduced.

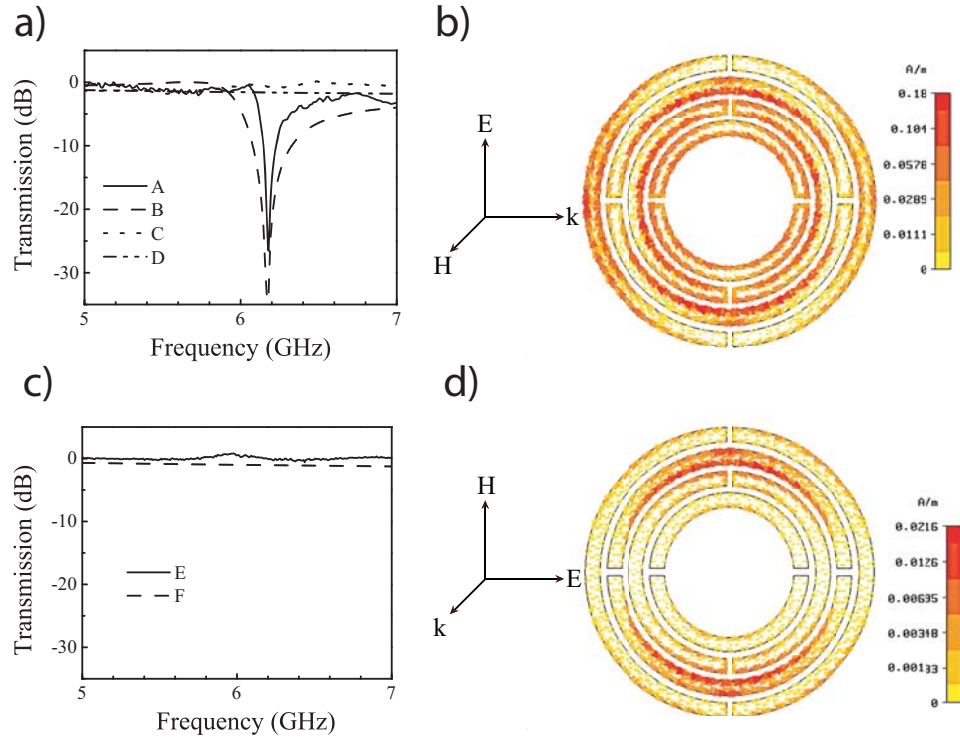


Figure 2.9: a) Measured transmission through a single labyrinth structure (A), a single closed labyrinth structure (B). Calculated transmission through a single labyrinth structure (C), a single closed labyrinth structure (D). b) Induced surface current density at 6.2 GHz. c) Measured (E) and calculated (F) transmission through a single labyrinth structure. d) Induced surface current density at 6.2 GHz.

Figure 2.7(a) shows schematics of the modified SRR structure that we propose. We call the modified SRR as “labyrinth” structure due to its shape. The labyrinth structure consists of four rings instead of two. The two additional rings are used for two main purposes, of which the first is to enhance the strength of the resonance. Second, the two-ring structure has two magnetic resonances that are close to each other. We used the additional two rings in order to separate the two magnetic resonances further away in frequency from each other. The unit cell of the fabricated structure is shown in Fig. 2.7(b). The structures are fabricated by using standard printed circuit board manufacturing methods. Figure 2.7(b) also

shows the coordinate system that we used throughout this section.

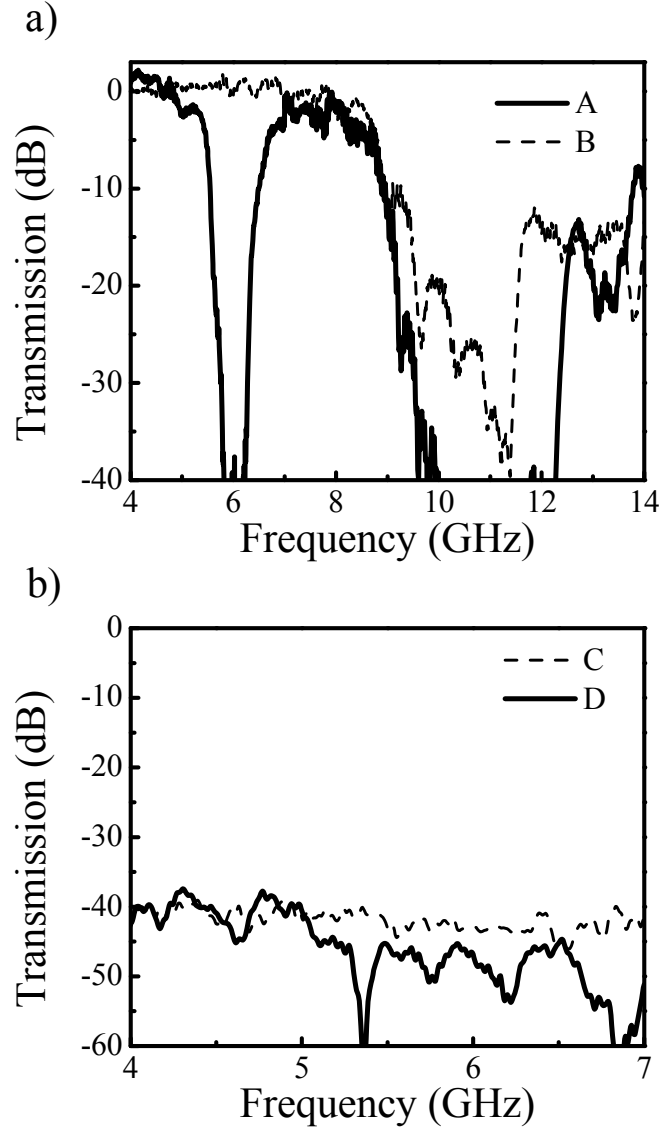


Figure 2.10: a) Measured transmission spectrum of the z-component of the electric field through (A) the labyrinth metamaterial medium and (B) through the closed labyrinth metamaterial medium. Only the z-component of the incident electric field was nonzero. b) Measured transmission spectrum of the x-component of the electric field through (C) free space and through (D) the labyrinth metamaterial medium. Only the z-component of the incident electric field was nonzero.

We calculated the induced surface currents, electric field distributions, and transmission properties of incident plane EM waves through the labyrinth structure by using a commercial 3 dimensional full-wave solver. We also measured the transmission properties of the labyrinth structure. The transmission properties of a single labyrinth structure are measured by using a HP 8510C vector network analyzer (Fig. 2.8) and two monopole antennas as receiver and transmitter antennas. The measured and calculated transmission spectrum of plane EM waves through a single layer of labyrinth structure is shown in Fig. 2.9(a). The directions of the electric field, magnetic field, and wave vector of the incident EM waves are shown in Fig. 2.9(b). First of all the transmission spectrum exhibits a resonance around 6.2 GHz with a transmission of -25 dB. Second, the closed labyrinth structure does not exhibit this resonance in the transmission spectrum. The calculated induced surface current is shown in Fig. 2.9(b). The induced surface currents are solenoidal and in phase along each arm. As a result the induced dipole moment has a magnetic character. The comparison of the transmission spectrum of the labyrinth structure with the transmission spectrum of the closed labyrinth supports this conclusion as the closed labyrinth structure does not exhibit any resonance near 6.2 GHz. Hence, a single labyrinth structure with the given dimensions exhibits magnetic resonance around 6.2 GHz.

In order to check whether the magnetic resonance of the labyrinth structure may be excited by incident electric fields, we measured and calculated transmission spectrum through a single layer of labyrinth structure when the wave vector is in to the plane of labyrinth structure. The directions of the electric field, magnetic field, and wave vector of the incident EM waves are shown in Fig. 2.9(d). Note that for the case of incidence configuration shown in Fig. 2.9(d) the magnetic resonance of the SRR structure can be excited by electric fields. The measurement and calculation results for a single labyrinth structure are shown in Fig. 2.9(c). The transmission spectrum does not show any resonance around 6.2 GHz. In addition, the surface current density that we obtained through our calculations is shown in Fig. 2.9(d). First of all, the surface current density is reduced by an order of magnitude when compared to Fig. 2.9(b). Second, the surface current density along each arm of the labyrinth structure is balanced either

by an opposite surface current density on the same arm or by an opposite surface current density flowing along the opposite direction on the opposite arm. As a result, the transmission spectrum shown in Fig. 2.9(c) and the surface current density shown in Fig. 2.9(d) clearly demonstrate that the magnetic resonance of the labyrinth structure cannot be excited by incident electric fields.

For the case of incidence depicted in Fig. 2.9(b), the SRR structure exhibits bianisotropy near the first magnetic resonance i.e., one also observes a non-zero electric field component parallel to the incident magnetic field in the transmission spectrum. In order to demonstrate that the labyrinth structure does not exhibit bianisotropy, we measured the transmission spectrum through a labyrinth metamaterial medium. The transmission measurements were performed with a HP-8510C network analyzer by using horn antennas as the receiver and transmitter. The labyrinth metamaterial is composed of periodic arrangement of labyrinths in a 1 dimensional array of 25 layers along the x direction, 20 layers along the z direction, and 5 or 10 layers along the propagation direction (y-axis). The directions are those of Fig. 2.7(b). The incident electric field is along the z direction and the wave vector is parallel to the y direction. We measured both the x and z components of the transmitted electric fields. Note that the incident magnetic field is parallel to the x-axis. The transmission measurement results for the z component of the electric field are shown in Fig. 2.10(a). The measured transmission data for the medium composed of closed labyrinth structures with the same number of layers is also shown in Fig. 2.10(a). The transmission spectrum for the labyrinth metamaterial medium exhibits a band gap between 5.9 GHz and 6.6 GHz for the z component of the electric field. The transmission spectrum for the closed labyrinth structure does not exhibit such a band gap. More importantly, we did not detect any appreciable electric field along the x direction in the transmission spectrum of the labyrinth metamaterial medium (Figure 2.10(b)). The x component of the electric field is measured by rotating the receiver horn antenna by 90 degrees. We measured the x component of the electric field with and without the labyrinth metamaterial medium in between the transmitting and receiving horn antennas. The transmitted x component of the electric field is around -40 dB within the frequency range of interest in free space. Note that the

polarization of the transmitting horn antenna is such that the emitted electric fields are z polarized. The measured transmission coefficients of the x component of the electric fields drop below -40 dB when the labyrinth structure is inserted between the horn antennas. Hence, these results clearly show that the labyrinth metamaterial medium is not bianisotropic.

2.2.1 Properties of the labyrinth structure with respect to different orientations

At this point, I would like to discuss the dependence of the properties of the labyrinth structure on the orientation. Two particular orientations are of considerable interest. The properties of the labyrinth structure with respect to these two orientations is important, if one creates three dimensional left-handed mediums by use of labyrinth structures. These two orientations are depicted in Figs. 2.11 (a) and (b). We will refer to these orientations as orientation 1 (Fig. 2.11(a)) and orientation 2 (Fig. 2.11 (b)). The calculated transmission spectrums of a single labyrinth structure (without the wires on the back of the PCB board) with respect to the orientations 1 and 2 are plotted in Fig. 2.12 (a). The resonance frequencies of labyrinth structures can be observed as dips in the transmission spectrum. The resonance frequencies of the single labyrinth structure with respect to the orientations 1 and 2 are 6.28 GHz and 6.32 GHz, respectively. The difference between the resonance frequencies with respect to the orientations 1 and 2 is 0.04 GHz, which is a change of 0.7 percent with respect to the resonance frequency. We also calculated the transmission spectrums of two-ring labyrinth structures with respect to orientations 1 and 2. The results are shown in Fig. 2.12 (b). For the two-ring labyrinth structure, the difference in the resonance frequency with respect to the two different orientations is 0.07 GHz, which is a change of 1.1 percent with respect to the resonance frequency. These results show that the resonance frequencies of four-ring labyrinth structure with respect to the orientations 1 and 2 are quite similar. In addition, we also conclude that the use of more rings reduces the difference in the response of the labyrinth structure with respect to the two different orientations. Next, we calculated the transmission spectrums

of labyrinth based left-handed metamaterial (LHM) medium with respect to the orientations 1 and 2. The labyrinth based LHM structures includes a single wire with a width of 2.5 mm in the unit cell printed. The wire was located on the back of the PCB board. There were 5 layers along the propagation direction in our calculations. We plotted the results in Fig. 2.13. The transmission spectrums of the labyrinth based LHM structure with respect to both orientations are in good agreement. We believe that the small difference in the transmission spectrums will be reduced in real experimental situations due to the fabrication imperfections.

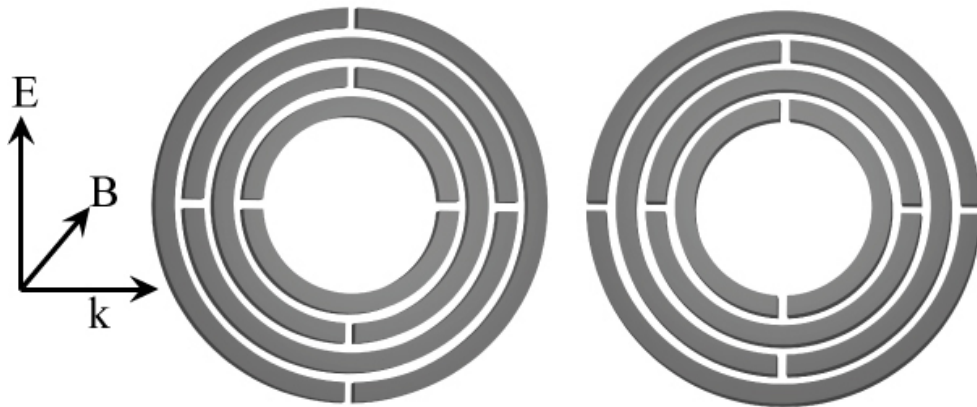


Figure 2.11: a) Orientation 1, b) Orientation 2.

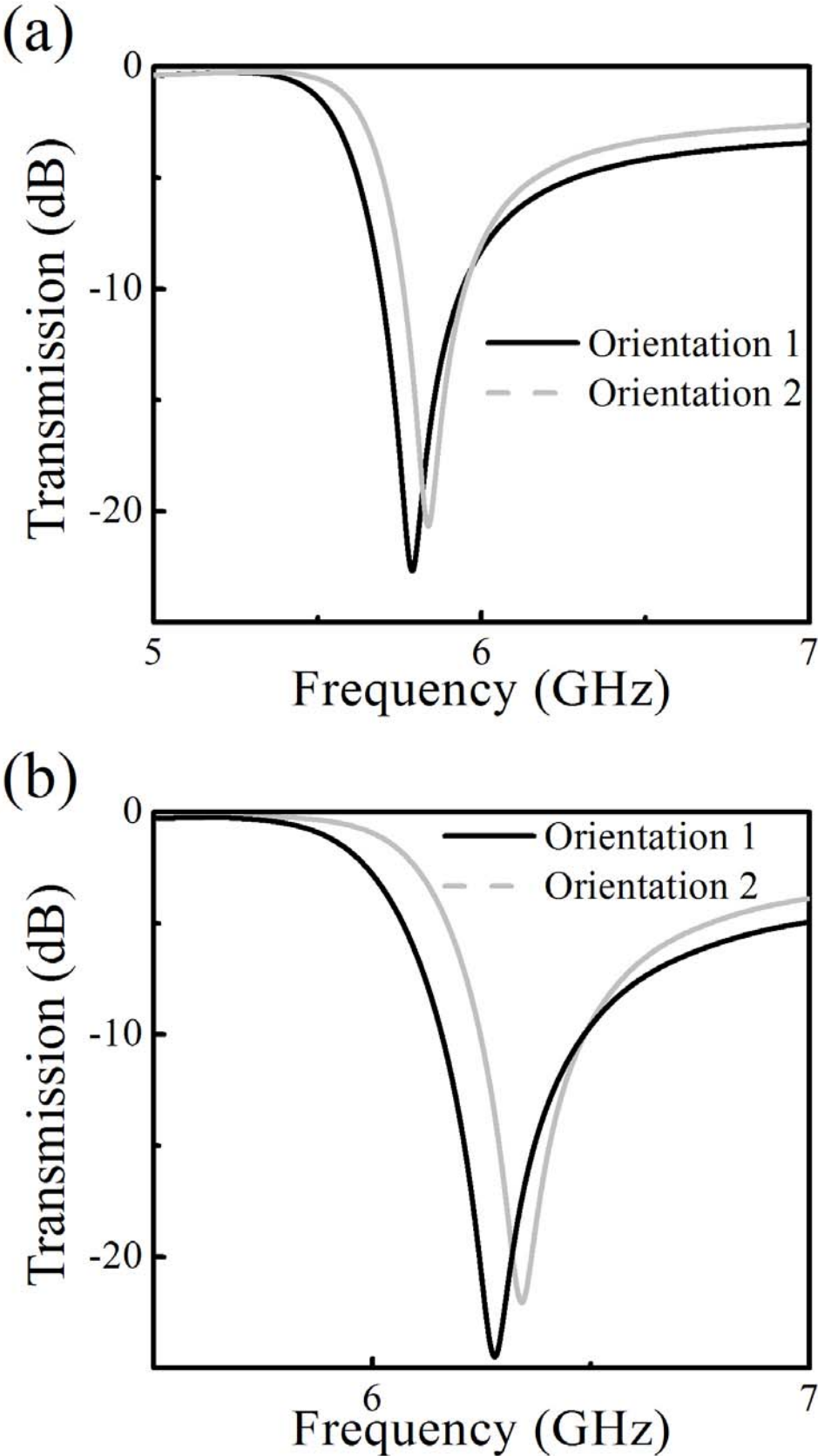


Figure 2.12: a) Transmission spectrum of four-ring single labyrinth structure with respect to orientations 1 and 2, b) Transmission spectrum of two-ring single labyrinth structure with respect to orientations 1 and 2.

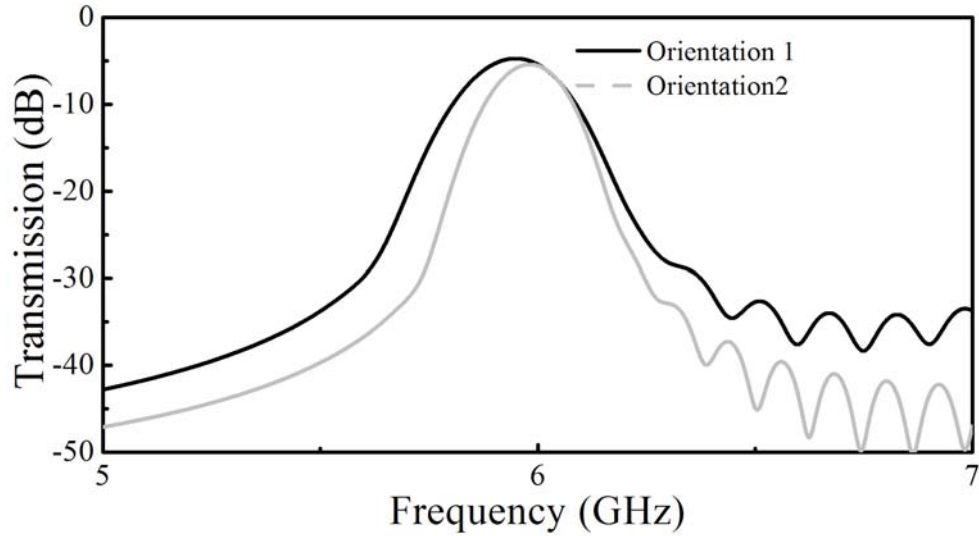


Figure 2.13: Transmission spectrums of 5 layers of labyrinth based LHM medium with respect to orientations 1 and 2.

2.2.2 Effective permittivity and permeability of the labyrinth structure

We calculated the effective permittivities and permeabilities of various labyrinth based LHM mediums by use of a retrieval procedure. The details of the particular procedure used in this study are outlined in references [45] and [46]. This particular method has the advantage of identifying the correct branch of the effective permittivities and permeabilities. The ambiguity in the determination of the correct branch is resolved by use of an analytic continuation procedure. There was one layer of the labyrinth based LHM structure along the direction of the propagation in our calculations. The orientation of the single layer LHM was that of Fig. 2.11 (a). We employed periodic boundary conditions along the directions other than the propagation direction. Hence, the simulation setup coincides with a slab of LHM that consists of a single layer. The dielectric constant of the PCB board was taken as 3.85. The PCB board has a thickness of 1.56 mm. The effective permittivities and permeabilities were derived from the transmission and

reflection coefficients. We would like to comment that the results of such a calculation are directly related to the electric and magnetic polarizabilities of a single feature because such a calculation does not involve the local field corrections due to other labyrinth features. The retrieval results for a single labyrinth structure without the wires on the back of the PCB board are plotted in Figs. 2.14 (a) and (b). First of all, the real part of the effective permeability attains negative values above a certain frequency. Both the real and imaginary parts of the permeability fit quite well to the relation

$$\mu_{eff} = 1 - \frac{f\omega^2}{\omega^2 - \omega_0^2 + i\tau\omega} \quad (2.33)$$

We used the following fitting parameters for both the real and imaginary parts of the effective permeability: $f=0.1806$ GHz and $t=0.0526$ GHz. It is also interesting to observe that the imaginary part of the permeability attains quite high values in the close vicinity of the resonance frequency. This result indicates that the labyrinth structure shows a quite strong resonant behavior at the resonance frequency. We also calculated the real part of the effective permittivity. The results are shown in Fig. 2.15. Notice that the permittivity is significantly increased just above the resonance frequency when compared to the effective permittivity of the host medium. The effective permittivity of the host medium was around 1.7 for our structure. This value was calculated by use of the relation

$$\varepsilon_{eff} = f\varepsilon_i + (1 - f)\varepsilon_e \quad (2.34)$$

. At 5.55 GHz, the permittivity of the labyrinth structure attains a value, 5.92, that is 3.5 times larger than the effective permittivity of the host medium. Hence, one should consider the dielectric response of the labyrinth structure around the resonance frequency when designing LHM mediums.

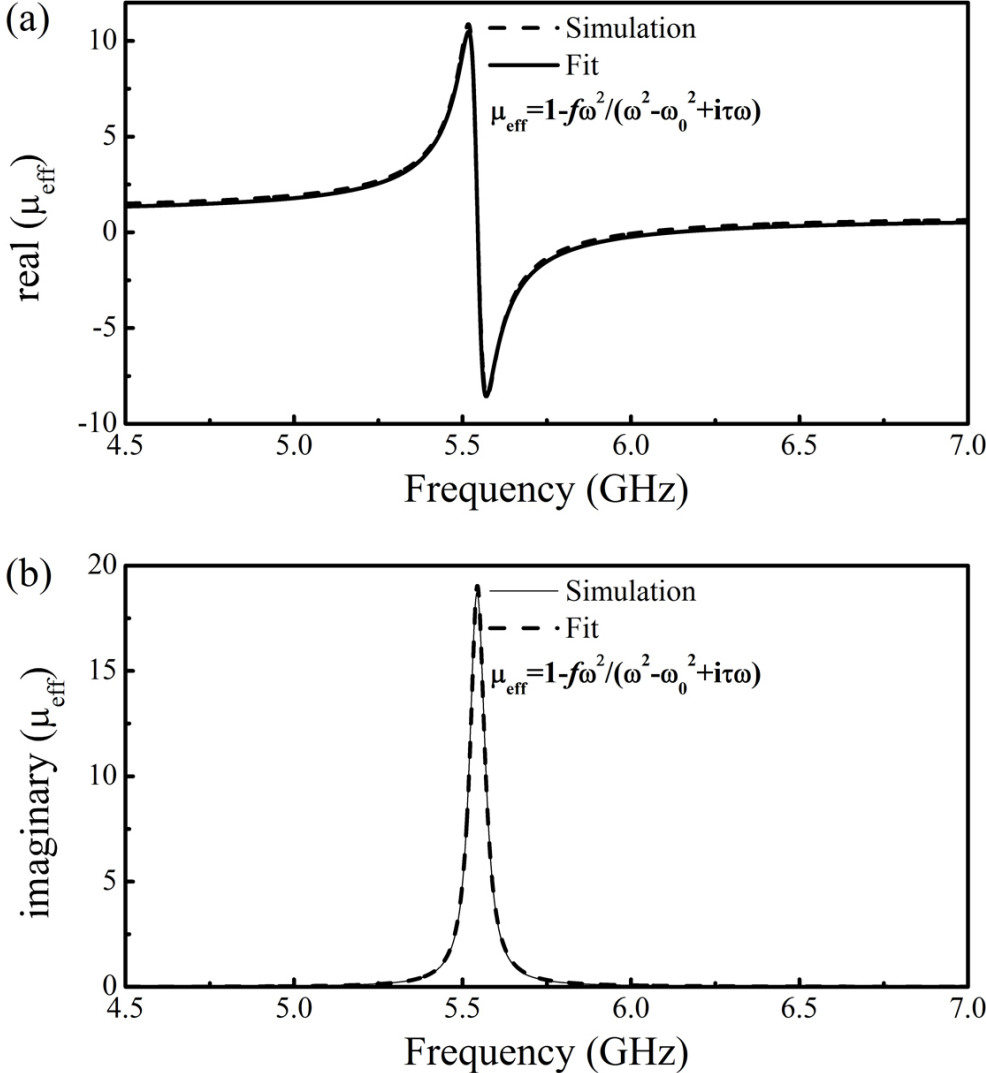


Figure 2.14: a) real part of the effective permeability for a single layer of the labyrinth structure, b) imaginary part of the effective permeability for a single layer of the labyrinth structure.

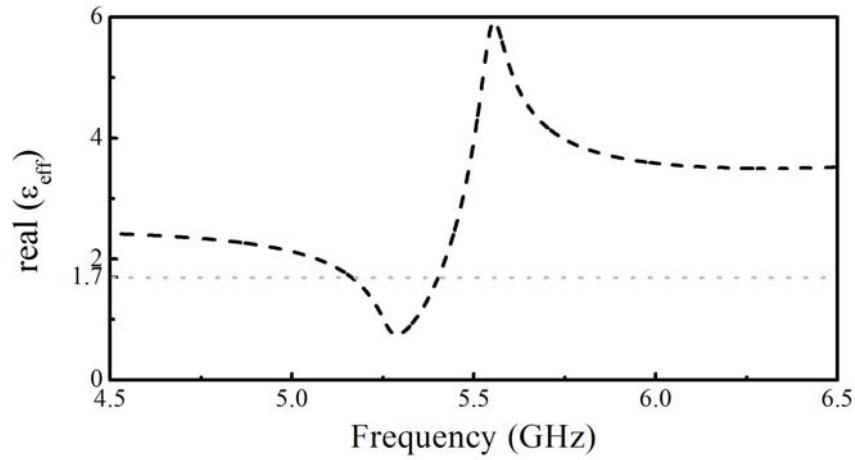


Figure 2.15: Real part of the effective permittivity for a single layer of the labyrinth structure.

2.2.3 Composite medium of labyrinth structures and thin wires

In the previous section we showed that unlike the SRR structure, the labyrinth structure does not exhibit bianisotropy. In addition, we showed that the electric coupling to the magnetic resonance of the labyrinth structure is forbidden due to the balanced currents. These properties provide important improvements over the common SRR structure. It is natural to ask if one combines the labyrinth metamaterial medium with a suitable wire medium, would the resulting composite metamaterial medium (CMM), Fig. 2.16, exhibit left-handed transmission within a frequency range.



Figure 2.16: A layer of the composite structure. Wires are printed on the back and labyrinth are printed on the front of the printed circuit board.

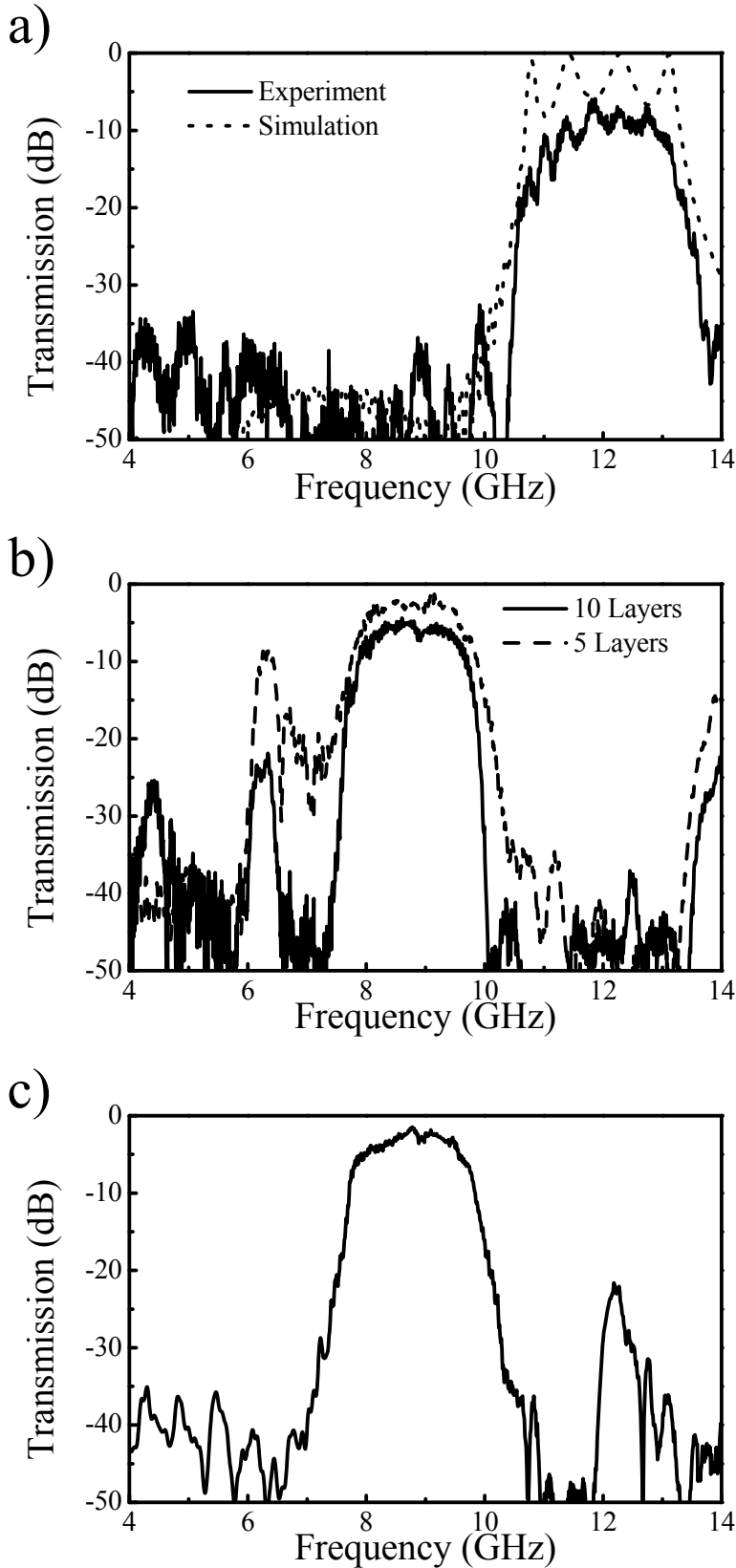


Figure 2.17: a) Transmission spectrum of electromagnetic waves through the wire medium. b) Measured transmission spectrum of electromagnetic waves through the CMM medium. c) Measured transmission spectrum of electromagnetic wave through the closed CMM medium.

The wire medium that we considered in our study was a one-dimensional periodic arrangement of metal stripes on the back surface of the printed circuit boards (PCB). The width of the wire stripes was chosen to be 2.5 mm. This choice was made in order to obtain a plasma frequency at a far enough frequency from the magnetic resonance of the labyrinth structure. The length of the wire stripes was 17.6 cm and the thickness of the stripes was 0.05 mm. The periodic arrangement of wire stripes had a lattice constant of 8.8 mm along y-axis and 6.5 mm along x-axis. The propagation direction was along y-axis. There were 10 layers of wire stripes along the y direction and 25 layers along the x direction. Measured transmission spectrum of the wire medium is shown in Fig. 2.17(a). The transmission spectrum for the wire medium exhibits a forbidden frequency range of up to 10.45 GHz. The plasma edge (10.45 GHz) of the wire medium is 4.2 GHz above the magnetic resonance of the labyrinth structure.

The CMM structure that we used in our study was composed of one-dimensional periodic arrangement of labyrinth structures and wire structures. Wires were printed on the back surface of the PCBs and labyrinth structures were fabricated on the front surface of the PCBs. Wires and labyrinth structures were aligned such that the axis of the wires were parallel to the splits on the labyrinth structure. There were 20 layers of CMM unit cells along z-axis and 25 layers of CMM unit cells along x-axis. The transmission spectrum for 5 and 10 layers of CMM unit cells along the propagation direction is shown in Fig. 2.17(b). Figure 2.17 shows that the transmission spectrum of the CMM medium exhibits a transmission band between 5.9 GHz and 6.55 GHz. Note that the magnetic resonance of the single labyrinth structure was observed at 6.2 GHz. In addition, the labyrinth structure exhibited a band gap between 5.9 GHz and 6.6 GHz. Hence, the transmission band of the CMM structure coincides with the band gap of the labyrinth metamaterial medium. We measured the transmission spectrum of the closed CMM medium in order to check whether the transmission band observed between 5.9 GHz and 6.55 GHz is left-handed [41, 56]. The closed CMM medium consists of a periodic arrangement of closed labyrinth structures and wires stripes. The lattice parameters were kept the same as the CMM medium. The transmission spectrum of the closed CMM medium is shown in Fig. 2.17(c).

First of all, the transmission spectrum of the closed CMM medium did not exhibit a transmission band between 5.9 GHz and 6.55 GHz. These results therefore show that the transmission band of the CMM medium is left-handed. In addition, the transmission spectrum of the closed CMM medium showed that the plasma edge of the wire medium shifts dramatically towards lower frequencies when the wire medium was combined either with a labyrinth medium or closed labyrinth medium. The plasma edge shifted from 10.45 GHz down to 7.6 GHz. Similar results demonstrating the shifting of the plasma edge towards lower frequencies were also reported for metamaterial mediums composed of SRR structures and wire structures [56].

2.3 Sub-wavelength Focusing

One fascinating consequence in particular of simultaneous negative permittivity and negative permeability is the possibility of focusing electromagnetic waves beyond the diffraction limit [10]. Pendry predicted that a slab of $\epsilon = -1, \mu = -1$ may recover evanescent components of the field emitted from a source. In addition, due to negative refraction, such a medium focuses the propagating components of the source field. As a result, it may be possible to focus all of the Fourier components of the field emitted from a source. Pendry coined the term superlens for structures that have these properties. However, until now Pendry's prediction has been subject to some criticism [57].

The metamaterial medium that we used was composed of a two-dimensional periodic arrangement of wire stripes and labyrinth structures. The unit cell of the metamaterial structure is shown in Fig. 2.18 (b). The wire stripes were printed on the back of the standard FR4 substrates and the labyrinths were printed on the front faces. The thickness of the metal, copper, was 0.05 mm. The width of the wire stripes was 2.5 mm. The lattice constant along the x and y directions were 8.8 mm (0.18λ , where λ corresponds to 6.3 GHz). There were 68 layers along the x direction and 5 layers along the y direction. The width of the structure was 0.92λ . The height of the structure was 20 layers long. This metamaterial medium has a

left-handed transmission band between 5.9 GHz and 6.5 GHz (Fig. 2.19 inset).

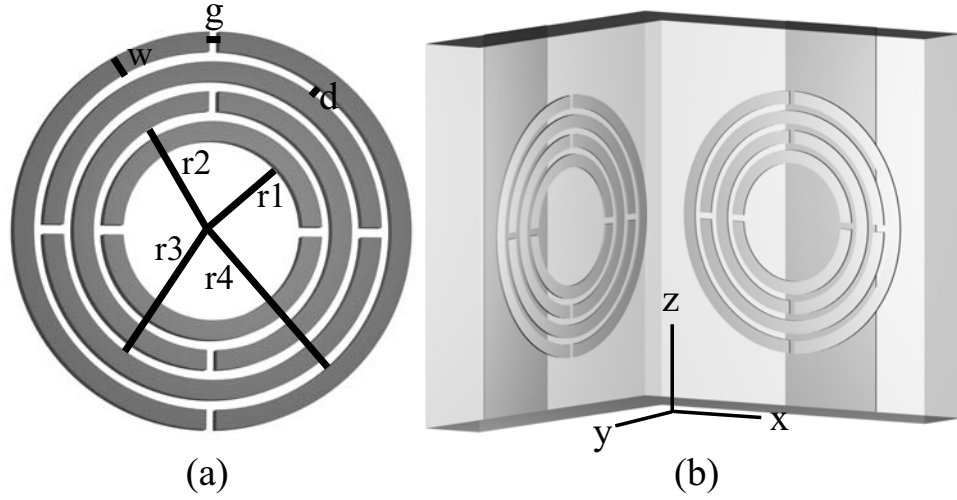
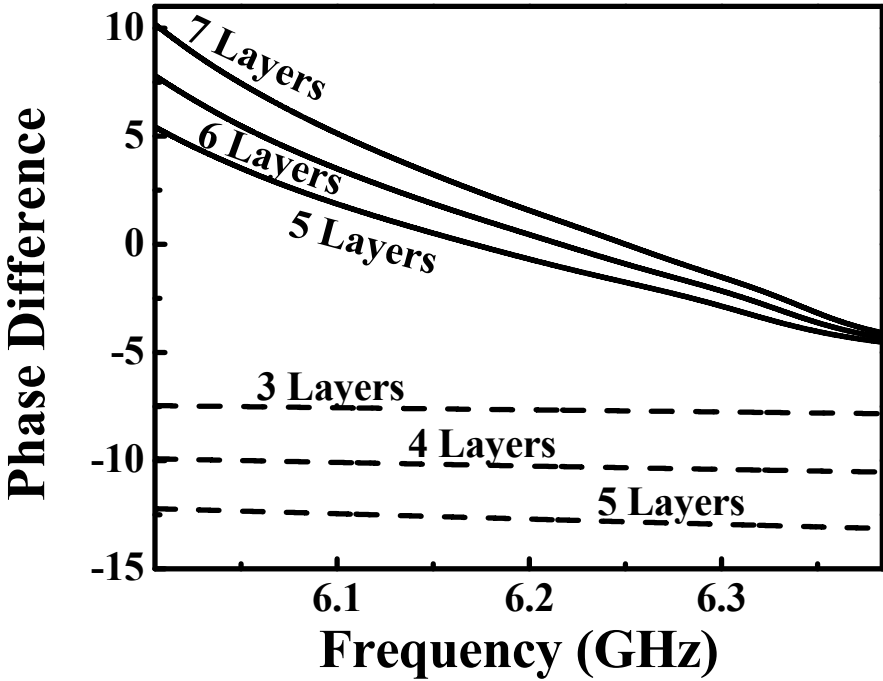


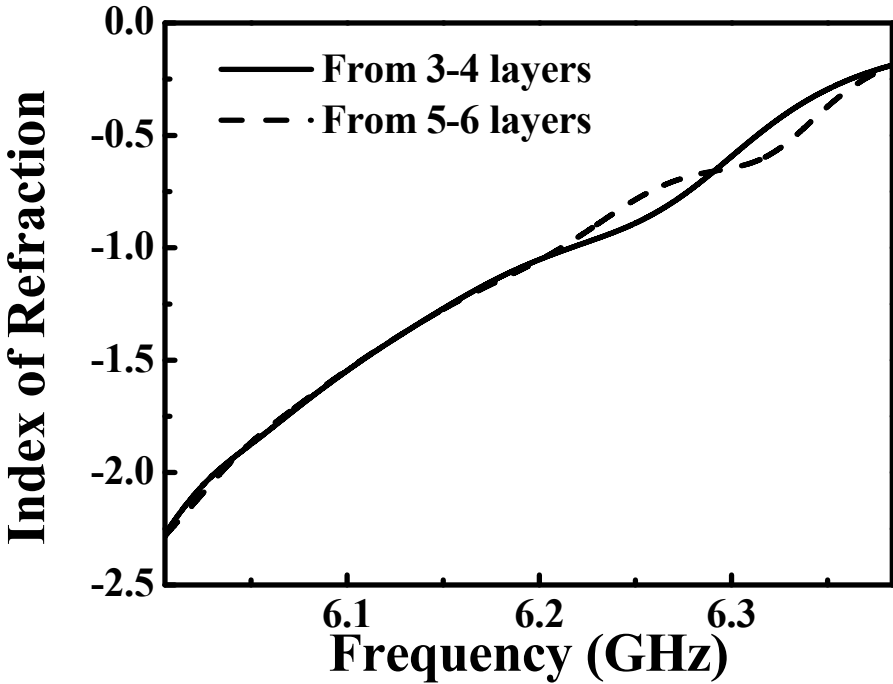
Figure 2.18: a) The labyrinth structure: $r1 = 1.35$ mm, $r2 = 1.8$ mm, $r3 = 2.25$ mm, $r4 = 2.7$ mm, $g = 0.15$ mm, $w = 0.3$ mm, and $d = 0.15$ mm. b) Unit cell of the two-dimensional labyrinth based left-handed metamaterial.

Several methods, such as retrieval procedures from S-parameters, can be used for the determination of the index of refraction [40]. Another rather straightforward method makes use of the phase shifts when the size of the structure along the propagation direction is increased [53]. It was experimentally shown that this method can accurately describe the real part of the index of refraction values for metamaterials even when the transmission was below -10 dB [53]. Consider two pieces of homogeneous material with lengths of L_1 and L_2 . The phase difference introduced due to the difference in lengths of the pieces can be written as $\Delta\phi = -\mathbf{k}_0 n(L_2 - L_1)$, where \mathbf{k}_0 is the free space wave vector. We used the $-\mathbf{k}_0$ convention in this study. In order to theoretically determine the phase shifts when the number of layers along the propagation direction is increased, we performed finite-integration method simulations by using a commercially available software program [58]. The simulation results for the phase differences between the ends of 5 layers, 6 layers, and 7 layers long metamaterials are shown in Fig. 2.19 (a). For comparison, we plotted the phase differences between the ends of 3 layers, 4 layers, and 5 layers long homogeneous, isotropic FR4 slabs. First of all, note that

the phase differences for the FR4 slabs advance in the negative direction when the number of layers is increased, as expected from a medium with positive index of refraction. Whereas, the phase differences between the ends of the metamaterial advance in the positive direction with increasing length along the propagation direction. In addition, the phase differences for different lengths of metamaterials do not change significantly around 6.4 GHz. We determined the index of refraction for the metamaterial medium by using the phase shifts shown in Fig. 2.19 (a). The results between 6.08 GHz and 6.4 GHz are plotted in Fig. 2.19 (b). The frequency range was chosen in order to have a transmission that was above -20 dB for accurate phase determination. The index of refraction is negative within this frequency range. In addition, there is a frequency range around 6.28 GHz at which the index of refraction is close to -1.



(a)



(b)

Figure 2.19: a) Phase differences between the ends of isotropic FR4 slabs (dashed curves) and the labyrinth based metamaterial (solid curves) b) Calculated indices of refraction for the labyrinth based metamaterial. (inset: measured transmission spectrum through the labyrinth based composite metamaterial medium (solid-curve) and the simulated transmission spectrum (dotted-curve).)

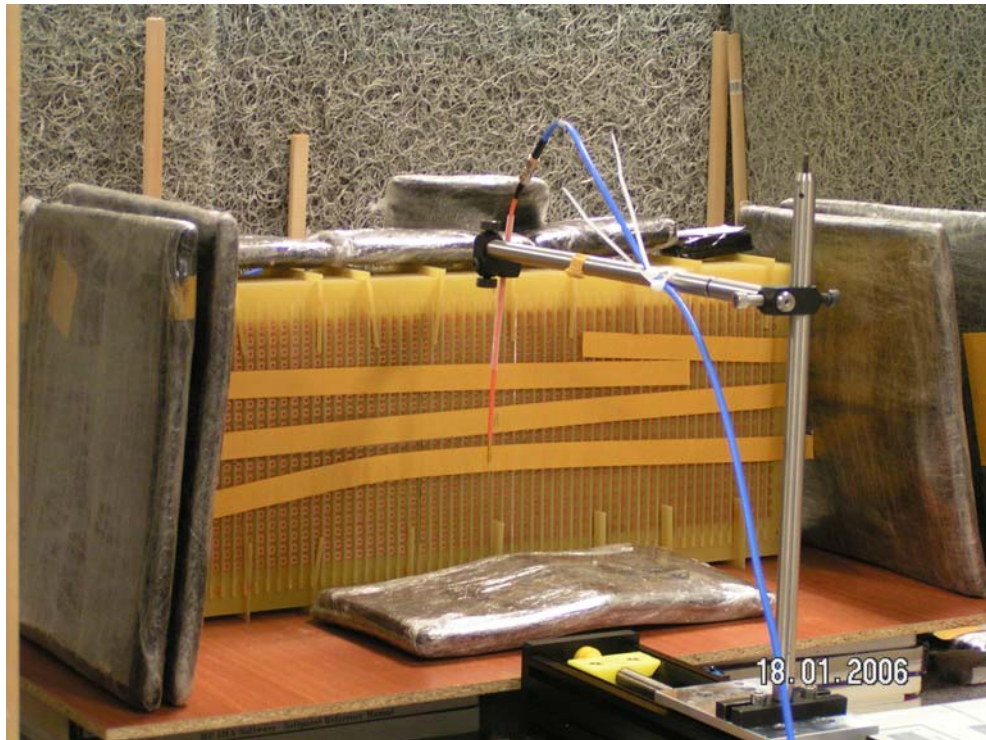


Figure 2.20: The measurement setup. The setup consists of HP8510C, two monopole antennas and a two-dimensional linear stage.

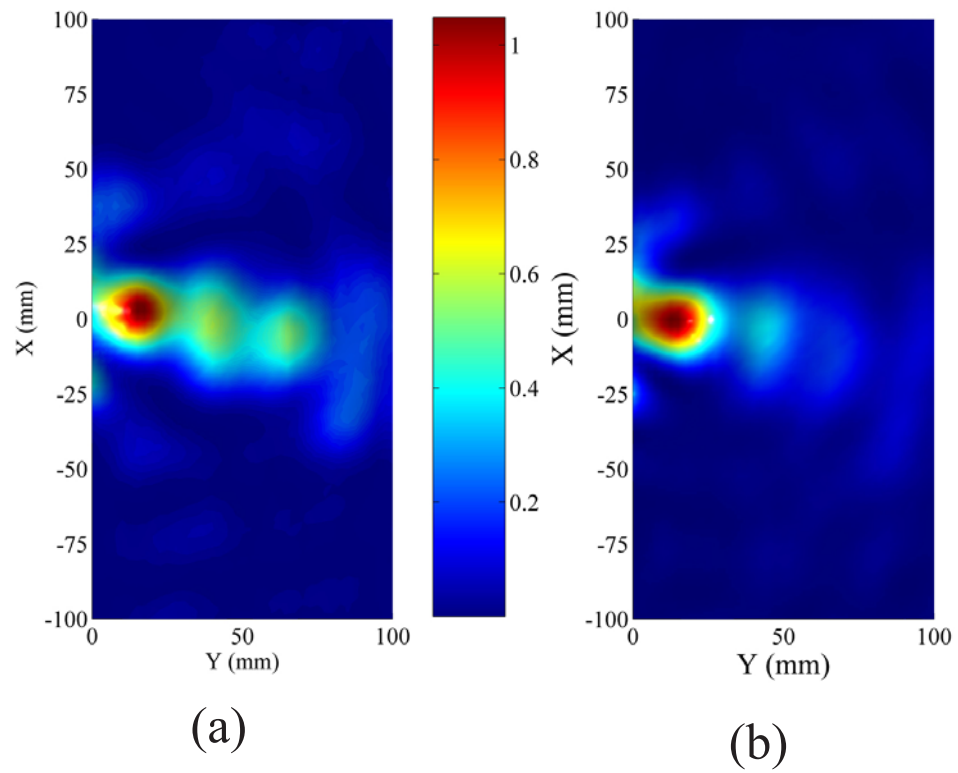


Figure 2.21: Measured electric field intensities on the output side of the metamaterial when the source was 2 cm away (a) and 1 cm away (b) from the input surface of the metamaterial.

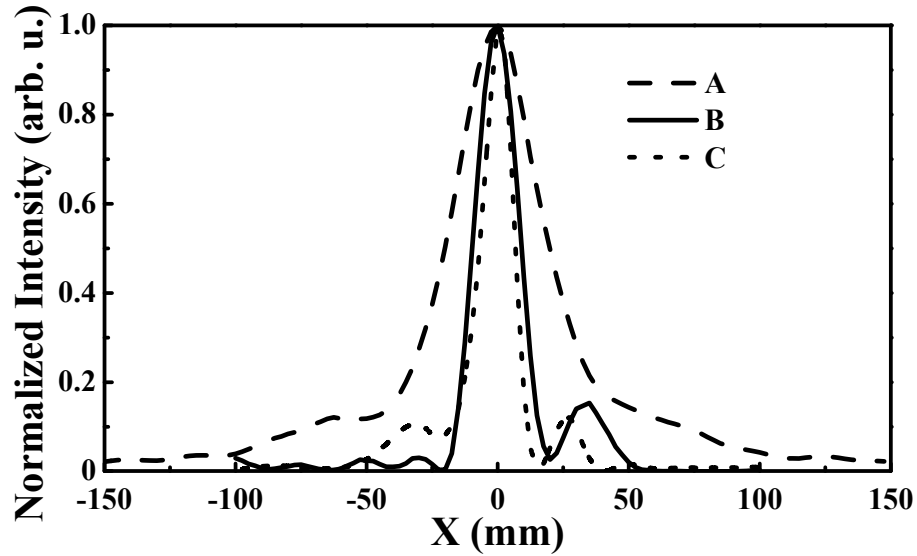


Figure 2.22: Measured intensity profile of the source monopole antenna along the x axis in free space when it was placed 2 cm away from the receiver antenna (A) 8 cm away from the receiver antenna (B). Measured intensity profile along the x axis on the output side of the metamaterial when the source was placed 2 cm away (C) and 1 cm away (D) away from the input surface of the metamaterial.

Encouraged by our theoretical results, we studied the focusing properties of the labyrinth based left-handed metamaterial. In our experiments we used monopole antennas as the source and receiver, Fig. 2.20. We placed the source antenna in front of the surface of the labyrinth based metamaterial. The axis of the source and receiver antennas were arranged parallel to the z -axis. The length and diameter of the monopoles were 3 cm and 1.5 mm, respectively. We measured the electric field intensities over an area of $200 \times 100 \text{ mm}^2$ ($4.25\lambda \times 2.1\lambda$) area on the output side of the left-handed metamaterial in steps of 2.5 mm (0.052λ), where λ corresponds to 6.3 GHz. The measured electric field intensities when the source antenna was placed 2 cm (0.42λ) and 1 cm (0.21λ) away from the input surface of the metamaterial are plotted in Fig. 2.21 (a) and (b), respectively. The measurement frequency was 6.3 GHz. Note that the surface of the metamaterial was parallel to the x axes. Figures 2.21 (a) and (b) clearly demonstrate the focusing of the source field on the output side by the left-handed metamaterial when the source was placed either 2 or 1 cm away from the input surface. The

maximum field intensity along the y axes was observed at 10 mm (0.21λ) when the source was 2 cm (0.42λ) away from the input surface, in which it was 17.5 mm (0.37λ) when the source was 1 cm (0.21λ) away. The half widths of the intensity profiles along the y axis for both cases were 19 mm, $\approx \lambda/2.5$. Moreover, the field intensities decay as $1/r^2$ along the y axes, where r is the distance from the focusing point. There are some extra features appearing on the image. We attribute these extra features to the interference from the waves reflected by the laboratory environment. The intensity profiles along the x axis are shown in Fig. 2.22. In addition, we plotted the measured intensity profile along the x axis when the source and receiver antennas were placed 2 cm apart from each other in free space (dashed-curve in Fig. 2.22). The measured half width of the intensity profile in free space, without the metamaterial in between, was 40 mm, $\approx \lambda$. Without the metamaterial, even at such a close distance, the source field could not be resolved with a resolution below the wavelength. On the other hand, the half width of the intensity profile on the output side of the metamaterial along the x axes was 12 mm, $\approx \lambda/4$, when the source was 1 cm away from the input surface, in which it was 16 mm, $\approx \lambda/3$, when the source was 2 cm away from the input surface. As a result, it was possible to resolve the source field with a resolution below the wavelength when the metamaterial was inserted in between the source and receiver antennas. The focusing property of the metamaterial was not restricted to 6.3 GHz. We observed the focusing effect for a range of frequencies between 6.2 GHz and 6.37 GHz, although the focusing was not as sharp as 6.3 GHz. Note that the source and image distances do not add up to the width of the slab (0.92λ). We attribute this to the complex part of the index of refraction.

Our experimental results showed that it was possible to focus the source field with a spot size as small as $\lambda/4$. We attribute the sub-wavelength focusing to two major reasons. First, the index of refraction is negative. Second, the left-handed metamaterial retains the inhomogeneous plane wave components of the source field. To our knowledge, this is the first experimental demonstration of the sub-wavelength focusing of electromagnetic waves by metamaterials in free space. Previously, sub-wavelength focusing was demonstrated by using a hard-wired L-C circuit network [59]. We believe that our study may find important applications

in areas of imaging. More importantly, our experimental results proved that metamaterials based on the labyrinth structure can focus the electromagnetic waves with half widths smaller than the wavelength.

2.4 Transmission, refraction, and focusing properties of a three dimensional structure

The three dimensional metamaterial that we used is shown in Fig. 2.23 (a) While the structure is an extension of the two dimensional labyrinth based metamaterial to three dimensions, the fabrication of the structure is itself quite complicated. Particular attention was paid during the design process in order to avoid intersecting wires. Such an intersection would evidently yield to a cut-wire medium. If not avoided, the cut-wire medium would cause us to lose the plasma-like behavior of a continuous wire medium. The results of the transmission measurements for TE and TM polarized electromagnetic waves, shown in Fig. 2.23 (b), show the evidence of a left-handed transmission band between 5.7-6.35 GHz. TE and TM is used to denote two perpendicular polarizations each of which is parallel to different wire orientations in the labyrinth-based metamaterial. The transmission of TE waves is weak when compared to TM polarized waves. This difference in the transmission properties of TE-TM polar-ized waves indicates the presence of strong anisotropy. Such anisotropy is expected as the unit cell of the structure lacks the electrical symmetries in certain directions. Nonetheless, there is a left-handed transmission band for both TE and TM polarized waves that overlap in the frequency range.

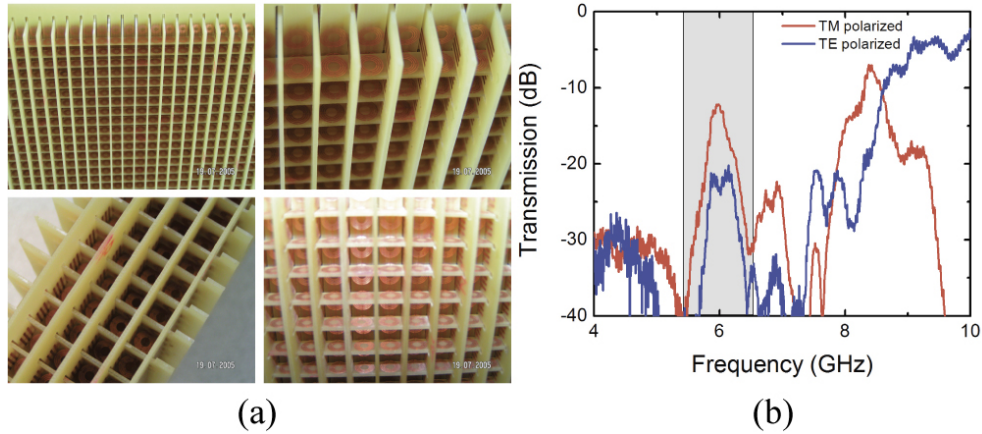


Figure 2.23: a) The photographs of the three dimensional structure. b) The measured transmission spectrum of TE and TM polarized waves through the labyrinth based three dimensional left-handed structure.

In order to study the refraction properties of the 3D structure at the frequencies corresponding to the left-handed transmission band, we used electromagnetic waves incident on the structure at various angles. The setup that we used consists of transmitting horn antennas and receiving monopole antennas. The horn antenna was tilted such that the angles of incidence with respect to the normal vector of the structure were 15 and 30 degrees. The transmitted waves on the other side of the surface were measured by using the monopole antennas over a rectangular mesh. The results of our measurements are shown in Figs. 2.24 (a) and (b) for incidence angles of 15 and 30 degrees, respectively. The output surface was parallel to the x axis. In addition, the waves were incident on the negative side with respect to the surface normal. Electromagnetic waves leave the output surface from the side of the surface normal that they were incident on. Hence, electromagnetic waves are negatively refracted by the 3D labyrinth based metamaterial. The index of refraction can be calculated by using the Snell's law and it is found to be around -1.02 at 6.2 GHz.

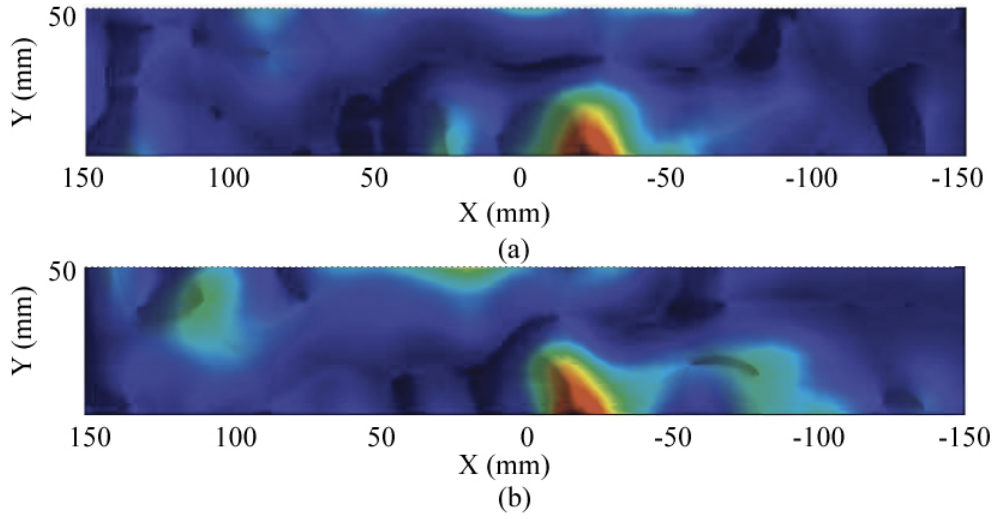


Figure 2.24: a) The measured electric field intensities for the incidence angle of 30 degrees. b) The measured electric field intensities for the incidence angle of 15 degrees.

Since our 3D structure exhibited negative refraction, we next checked the focusing properties of the structure. We placed a monopole antenna in front of the input surface of the structure and measured the transmitted signal on the output side over a rectangular mesh by using a receiving monopole antenna. The results are shown in Figs. 2.25 (a) and (b) for source distances of 15 mm and 5 mm to the input surface, respectively. First of all, one can clearly observe the images of the source field at the output side. In addition, the image of the source appears at a closer distance to the output surface for the source distance of 15 mm when compared to the source distance of 5 mm. This result is expected for a metamaterial medium with simultaneously negative permittivity and permeability [10]. The half-width of the image is $24.5, \lambda/2$, mm at 6.1 GHz.

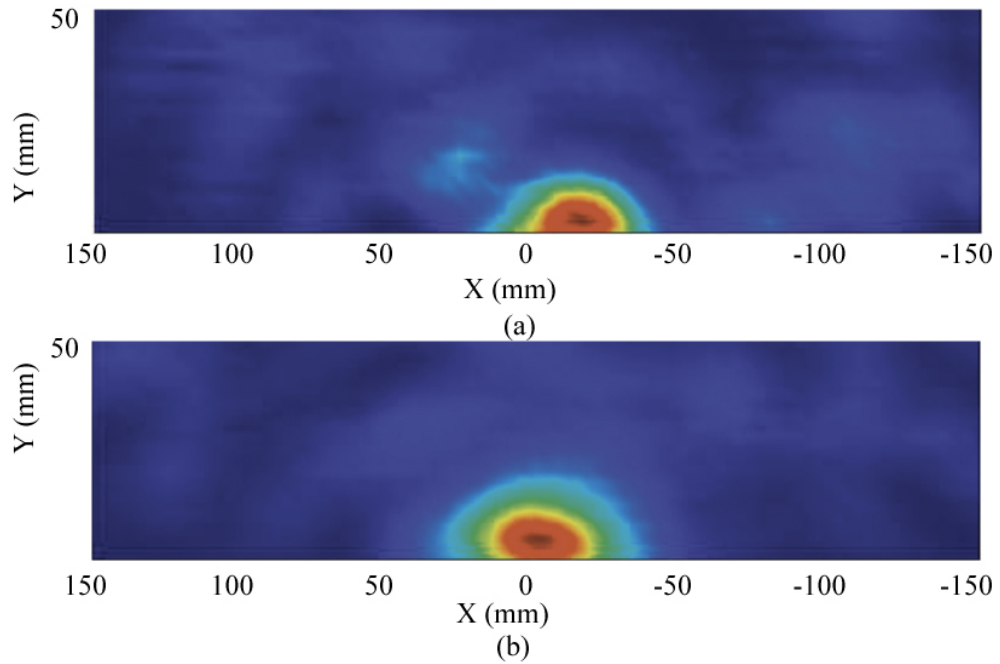


Figure 2.25: a) The measured electric field intensities for a source distance of 15 mm. b) The measured electric field intensities for a source distance of 5 mm.

2.5 Sources Inside Metamaterials

In this section, we studied the properties of the electromagnetic fields emitted from a source embedded inside a two-dimensional left-handed metamaterial that was based on labyrinth resonators. Our results showed that when the source is placed at a certain distance away from the interface, the transmitted field is focused on sub-wavelength dimensions. We will first present our retrieval results regarding the permittivity and permeability of the labyrinth based left-handed medium. We will show that there is a frequency at which the permittivity and permeability attains the same negative value i.e., impedance matched to free space. We will subsequently present our theoretical and experimental results for the impedance matched frequency when the source is placed inside the left-handed medium.

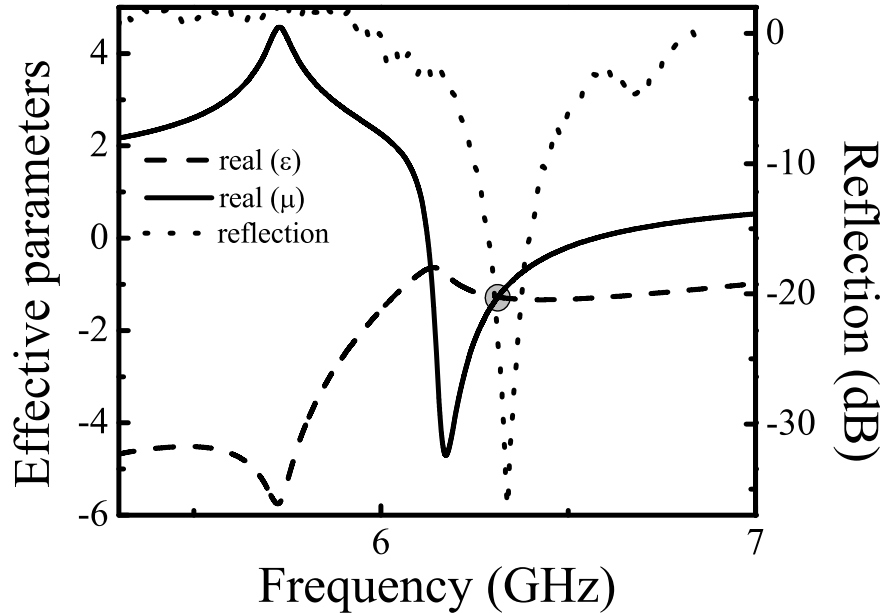


Figure 2.26: The calculated effective medium parameters of the labyrinth-based left-handed medium: real part of the ϵ (- -) and real part of the μ (-). The measured reflection spectrum from the labyrinth-based left-handed medium (...).

The transmission, refraction, and focusing properties of metamaterials have been extensively studied up to now. Several researchers demonstrated negative permeability, left-handed transmission, negative refraction and sub-wavelength focusing by using metamaterials [8, 60]. On the other hand, the emission properties of sources when they are placed inside metamaterials still remain to some extent unexplored. The study of the field emitted from a source, which is placed inside an LHM slab, provides exciting answers for both physical and technological considerations. First of all, such a study provides the means of checking the validity of ray optics on LHM metamaterials whose overall dimensions are comparable to one wavelength. In addition, the information gained from such studies are important for the applications that incorporate radiation sources and active or non-linear materials inside LHM metamaterials [61, 62, 63, 64, 65]. There are

several theoretical studies that investigate the issue of sources inside a metamaterial with permittivity and permeability that was equal to zero. In addition, there are some studies that attempt to use metamaterials in order to enhance the characteristics of antennas [66].

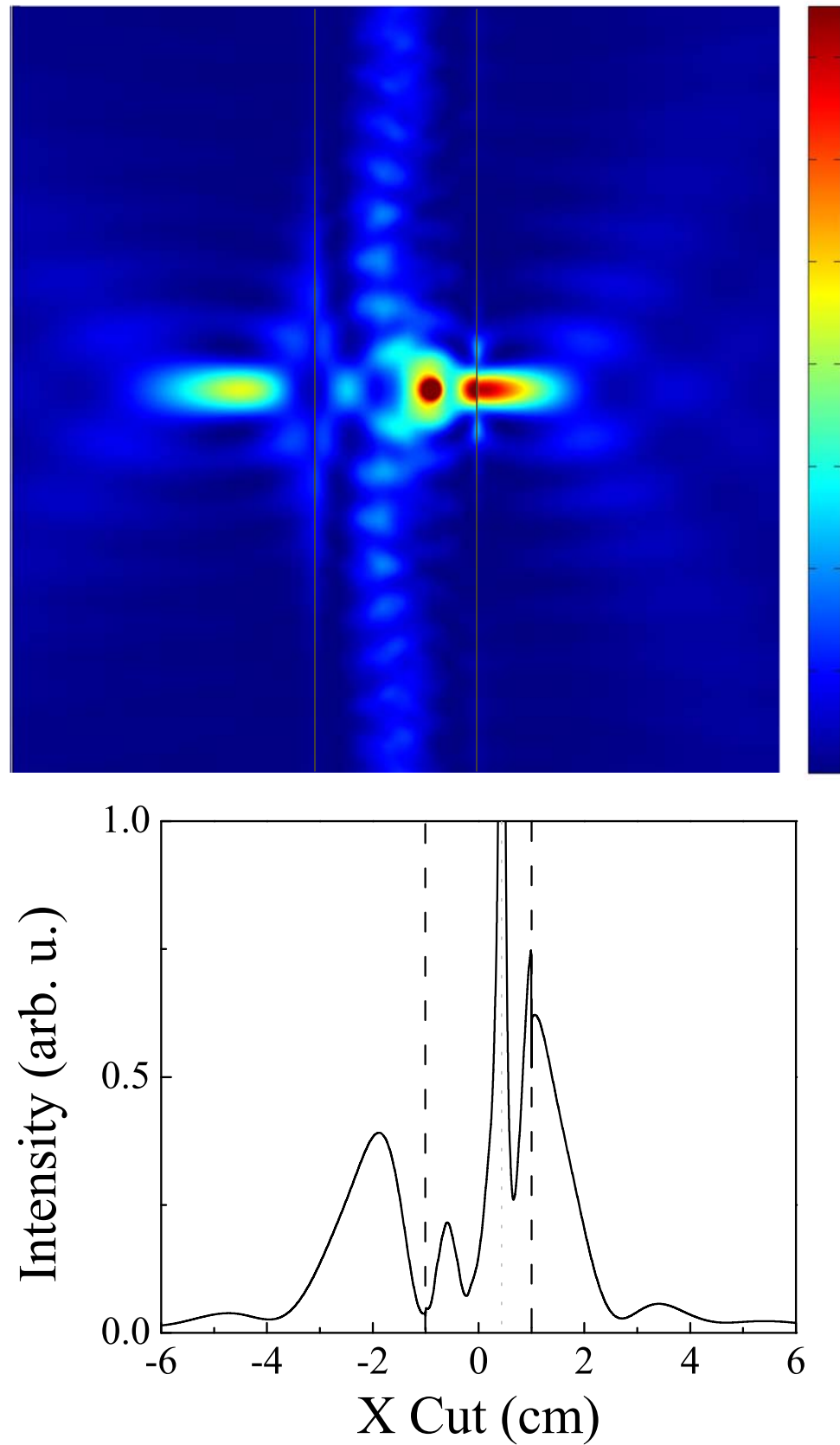


Figure 2.27: Top panel: The simulated field intensity emitted from a source placed inside the homogeneous left-handed medium. Bottom panel: The cross section of the field intensity along the x-axis on the source plane.

The structure that we used for this study was a two-dimensional periodic arrangement of wires and labyrinth structures. We calculated the effective permittivity and permeability of the two-dimensional medium by using a retrieval procedure. The results are shown in Fig. 2.26. There is a certain frequency range at which the permittivity and permeability are negative. In addition, the values of permittivity and permeability (real parts) are the same at 6.3 GHz with a value of -1.24. Moreover, the values of the imaginary parts are low at this frequency, 0.014 and 0.1, respectively. As a result, the impedance of the medium is matched to the free space at 6.3 GHz. Therefore, one expects a significant reduction of the reflection coefficient around 6.3 GHz. We measured the reflection spectrum from the two-dimensional left-handed medium by using an HP-8510C network analyzer. Receiving and transmitting horn antennas were used for the measurements. The measured reflection spectrum of the two dimensional medium is shown in Fig. 2.26. The reflection from the two-dimensional medium is rather small around 6.31 GHz (-35 dB at 6.31 GHz).

We carried out FDTD simulations in order to study the properties of the electromagnetic waves when the source was placed inside the left-handed medium. In our simulations, we treated the two-dimensional labyrinth-based medium as a slab of homogenous and isotropic material. This approximation provides the means to compare the actual left-handed metamaterial with an isotropic and homogenous medium. In addition, such an approximation is justified due to the fact that the size of the labyrinth features are very small compared to the wavelength of interest. The permittivity and permeability of the slab was set to -1.24, and the simulation frequency was 6.3 GHz. The thickness of the slab was equal to the thickness of the labyrinth-based medium that we used in our experiments, 8.8 cm (10 layers of a labyrinth-based medium). Note that the thickness of the slab was 1.87λ . The source was placed 7 layers, 6.16 cm, away from the left side interface. The result of the FDTD simulation is shown in Fig. 2.27. When the source is 7 layers away from the interface (left side interface), there is a clear focusing of the source field away from the interface. The half width of the image along the y axis at the maximum intensity point is $\lambda/2.35$. On the other hand, when the source is 3 layers away from the interface (right

side interface), the image is rather close to the surface. The half width of the image in this case is reduced to $\lambda/3.42$. It is noteworthy that geometrical optics considerations would lead image points away from the interfaces for both cases.

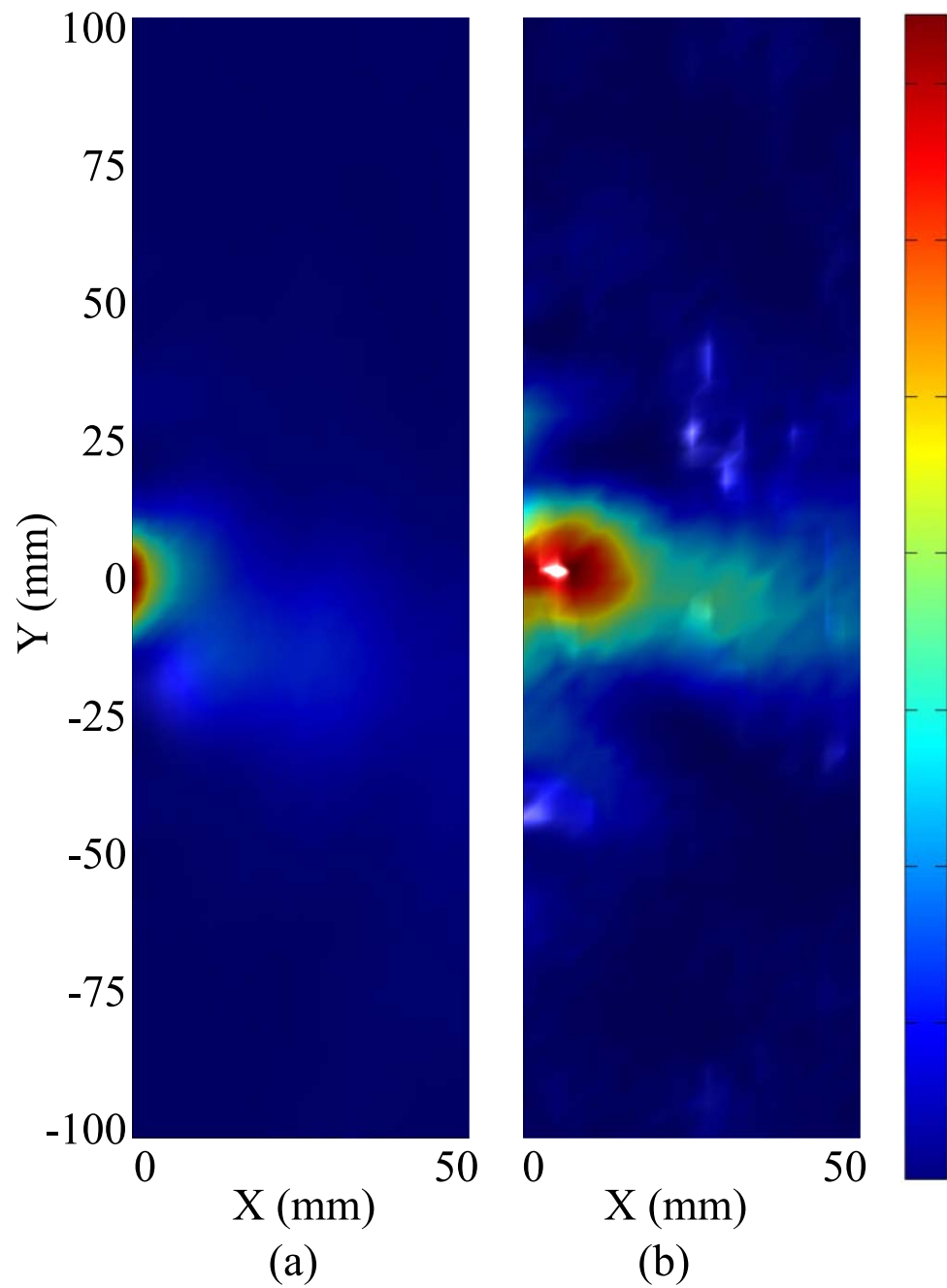


Figure 2.28: a) The measured field intensity when the source was placed 3 layers away from the interface inside the labyrinth-based left-handed medium. b) The measured field intensity when the source was placed 7 layers away from the interface inside the labyrinth-based left-handed medium.

We used an HP-8510C network analyzer to perform the experiments. The transmitting monopole antenna was placed inside the two-dimensional labyrinth-based left-handed medium. The width of the labyrinth-based medium was 10 layers, 8.8 cm. The receiving monopole antenna was used to measure the field outside the left-handed medium over an area of $50 \times 100 \text{ mm}^2$ area with steps of 2.5 mm. More details regarding the experimental procedure can be found elsewhere [60]. The results of our measurements when the source was 3 layers and 7 layers away from the interface are shown in Figs. 2.28(a) and (b), respectively. The image of the source field appeared to be tied to the surface when the source was 3 layers away from the interface. The half width of the image was $\lambda/3.2$. On the other hand, the image appeared away from the interface when the source was placed inside the seventh layer. The maximum intensity point along the x-axis was 10 mm away from the interface. In addition, the half width of the image was $\lambda/2.3$. We would like to note that the comparison of Figs. 2.27 and 2.28 shows a quite good agreement between our simulation results, which treated the left-handed medium as a homogenous and isotropic material, and experimental results. Both of these results indicate that one cannot treat a left-handed medium by use of geometrical optics if the overall dimensions of the medium are comparable to the wavelength of interest. The reason for this is if we were to apply the argument of the geometric optics, we would expect to observe an image away from the surface for both of the source distances. The discrepancy of both experimental and theoretical results from the expectations of the geometrical optics is attributed to two main reasons. One of the reason is related to the size of the left-handed medium. As the size of the left-handed medium is comparable to the wavelength, the results of geometrical optics are questionable. The second reason is related to the excitation of the surface plasmon waves. Figure 2.27 shows the existence of surface waves along the edges of the left-handed medium.

2.6 Compact size highly directional antennas based on SRR metamaterial medium

In this section, we experimentally and theoretically study the angular distribution of microwave radiation from a monopole source embedded inside a SRR metamaterial medium. We will first review two important properties of SRR structure relevant to the study of radiation sources inside SRR metamaterial medium. In this sense, we will be concerned with the distribution of the surface current along the SRR structure and the distribution of the electric field within the unit cell of the SRR metamaterial medium. Finally, we will experimentally demonstrate that the radiation emitted from a monopole source embedded inside a SRR metamaterial medium exhibit a highly directive radiation pattern.

2.6.1 Properties of the split-ring resonator

Since the introduction by Pendry [18] split-ring resonators (SRRs) attracted great interest among the scientific community [49, 8, 52, 33, 67, 68]. One of the major reasons of this great interest lies in the fact that SRR shows strong magnetic activity at high frequencies that is not obtainable by natural materials. Several researchers demonstrated strong magnetic activity by using SRRs in the Gigahertz and Terahertz region [49, 69]. In addition to negative permeability and strong magnetic activity, SRR is a resonant structure whose dimensions are much smaller than the resonance wavelength. The small size of the resonant SRR structure may provide means to modify and control the emission properties of sources with small-sized structures.

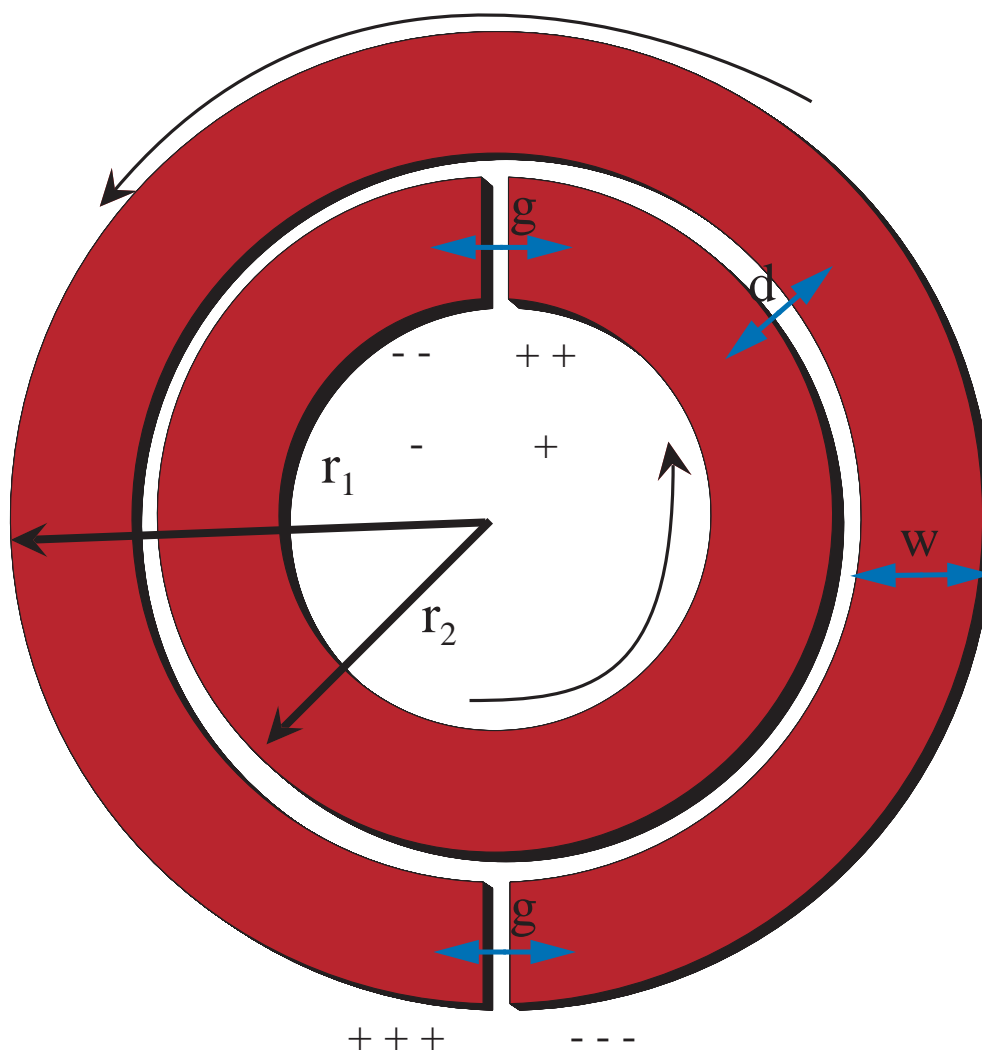


Figure 2.29: The SRR structure. Following dimensions are used through out our experiments and simulations: $g=0.2$ mm, $d=0.2$ mm, $w=0.9$ mm, $r_1=3.6$ mm, $r_2=1.6$ mm. Arrows indicate the direction of current flowing around the structure.

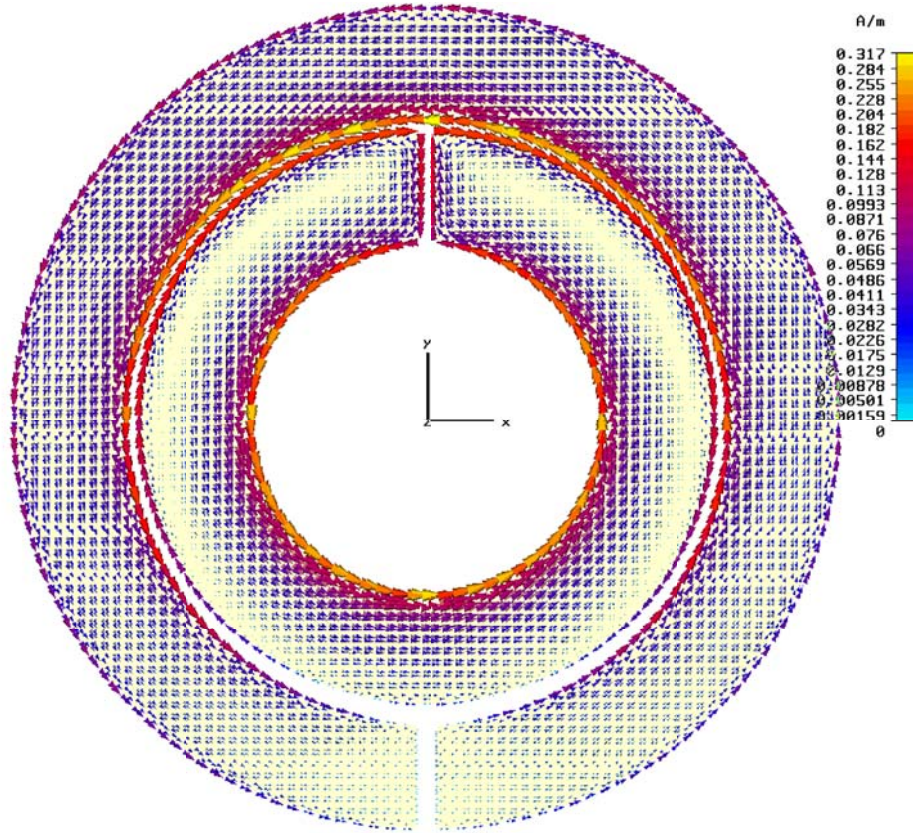


Figure 2.30: Surface current density along the SRR structure at the resonance frequency.

SRR structure consists of two concentric annuli of conducting material. There is a gap on each ring and each ring is situated opposite to the gap on the other ring. A common SRR structure is depicted in Figure 2.29. When excited by an external source, for example, by a time-varying magnetic field perpendicular to the plane of SRR, current flows along the rings are induced. The induced current flows result in accumulation of charges near the gaps of the SRR. The circuit is completed by the capacitive coupling between two rings. Due to the gaps on each ring, current flows on individual rings are very small. The structure is similar to an L-C circuit. The main contribution to the capacitance of the circuit comes from the mutual coupling between the two rings [31]. Induced surface current by a plane wave excitation at the resonance frequency of the SRR is shown in Figure 2.30 . First of all, the induced current density along the structure is in

phase. Second, the induced current is solenoidal. Hence, the SRR structure can be considered as a magnetic dipole. In fact, the associated magnetic field pattern from the SRR is dipolar [8]. In addition to the resonant solenoidal current, SRR structure concentrates the incident electric field to its close vicinity. Figure 2.31 shows the simulated electric field distribution within the unit cell of the SRR metamaterial medium. The incident wave is a planewave with unit amplitude. The electric field shown in Figure 2.31 indicates that the incident electric field is localized near the SRR structure. Also, note that the electric field amplitude attains values as large as 2 orders of magnitude larger than the incident wave.

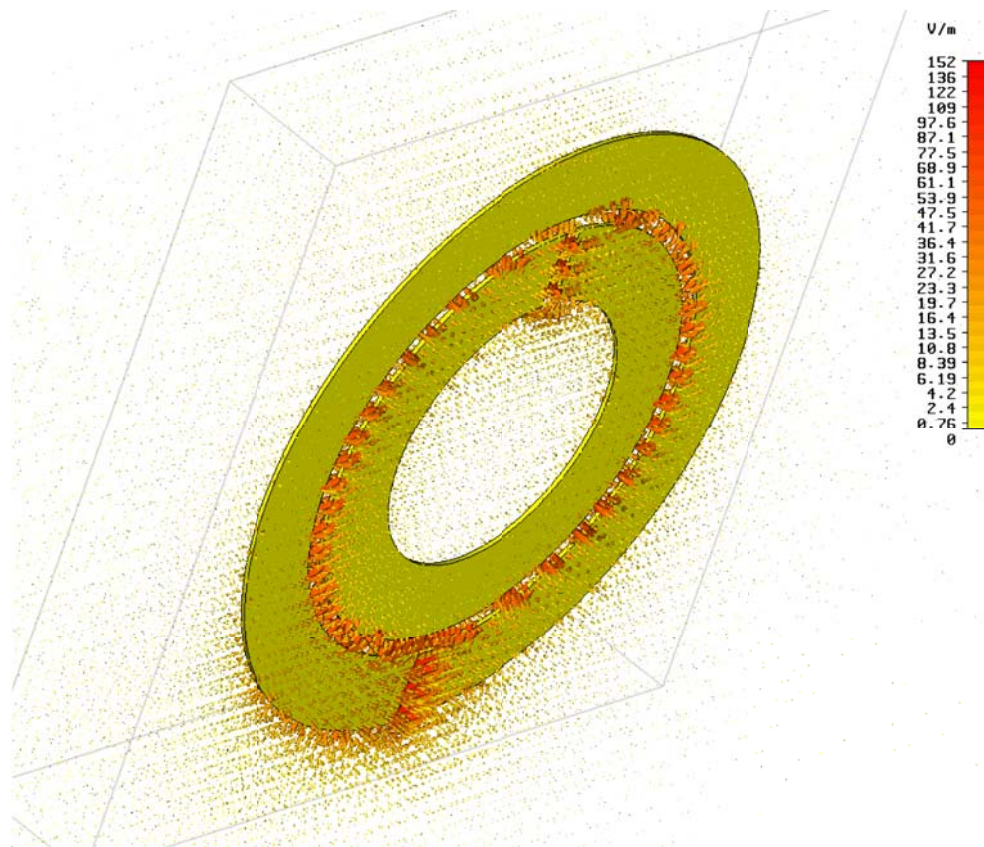


Figure 2.31: Simulated electric field distribution within the unit cell of the SRR metamaterial medium. Incident planewave has a unit amplitude. View angle is tilted for better visualization.

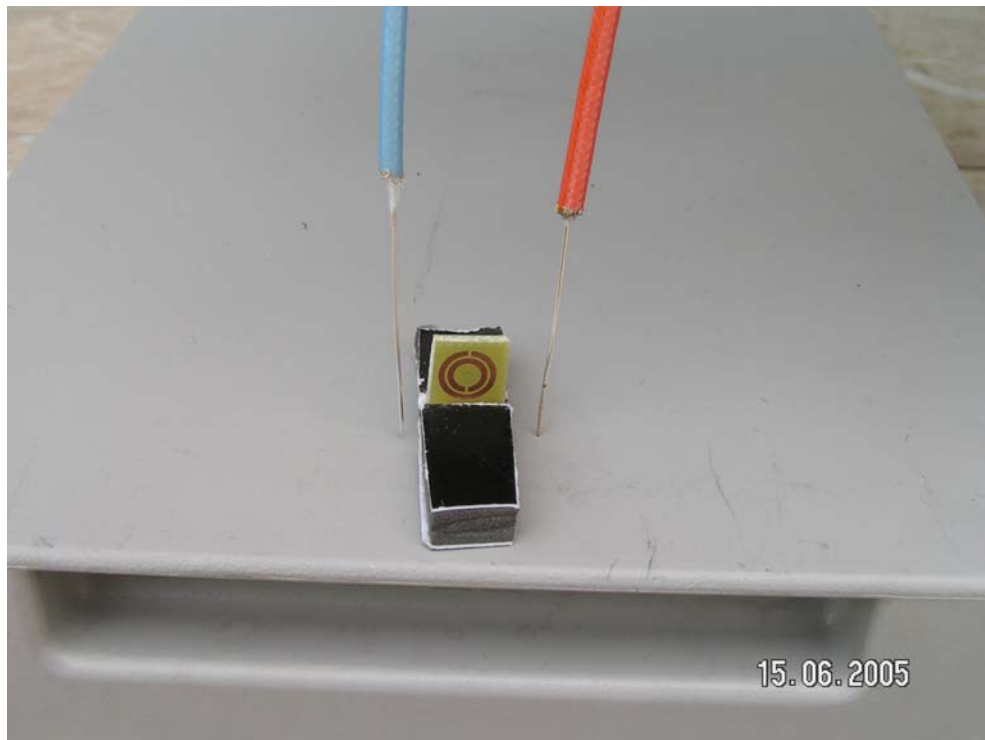


Figure 2.32: This setup was used to determine the resonance of a single split-ring resonator.

The resonant nature of the SRR structure is pronounced as a dip in the transmission spectrum. This dip can be easily observed by measuring the transmission spectrum of a single SRR structure by two monopole antennas, one transmitting and the other receiving, Fig. 2.32. The monopole antennas that we used in our experiments are obtained by removing the dielectric cladding and the metal shield of a microwave coaxial cable. The left inner core has a length of 7 cm. The monopole length is optimized for operation around 4 GHz. The transmission coefficients of a single SRR structure placed between two monopole antennas is then measured by an HP-8510C network analyzer. HP-8510C is a vector network analyzer capable of measuring both the transmission and the phase. SRR structure is manufactured by standard printed circuit board technology. The substrate is standard FR-4 material and the metal is copper with a thickness of 0.05 mm. The thickness of the board is 1.6 mm and the measured relative permittivity around 4 GHz is 3.85. The measured transmission data and the results of the FDTD

simulation are shown in Figure 2.33 . For comparison, we have also measured the response of the closed SRR structure. In the closed SRR structure we have two complete rings. The transmission data for a single SRR structure shows a strong dip around 3.65 GHz. Note that this dip is not observed in the transmission spectrum of the closed SRR structure.

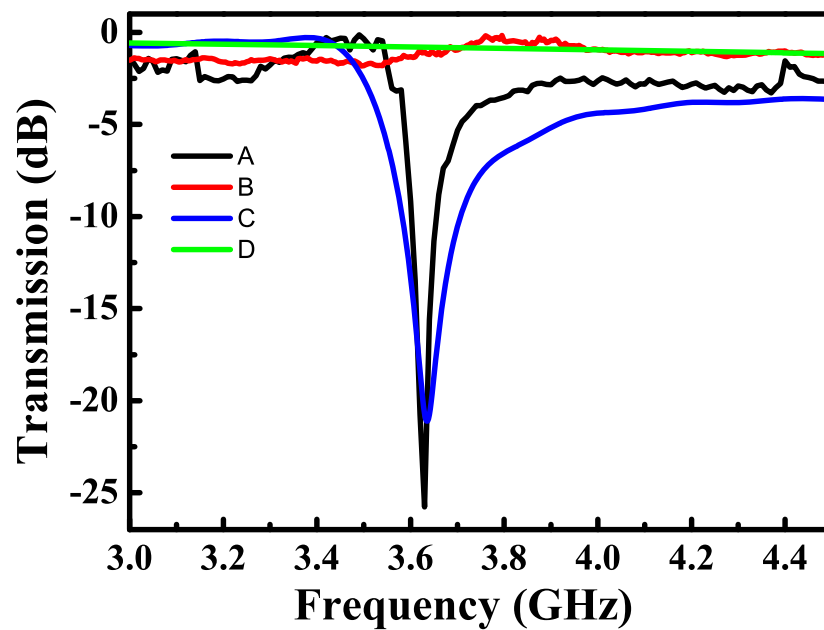


Figure 2.33: Measured transmission spectrum of (A) SRR structure, (B) closed SRR structure. Simulated transmission spectrum of (C) SRR structure, (D) closed SRR structure.

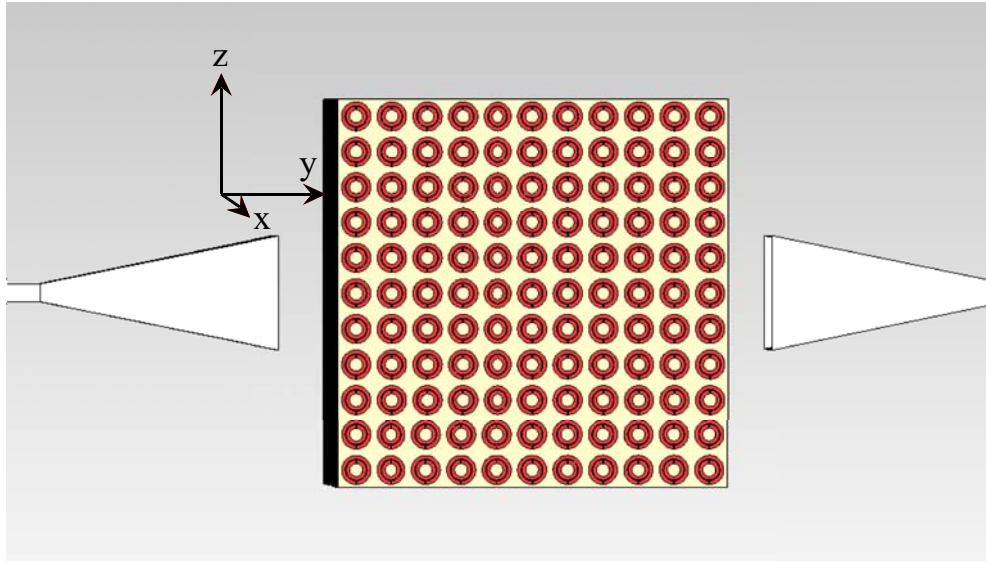


Figure 2.34: Experimental setup that we used to measure the transmission properties of the SRR metamaterial medium. The setup consists of transmitting-receiving horn antennas and HP-8510C network analyzer.

At this point, we would like to emphasize two important properties of the SRR structure. First of all, at the resonance frequency solenoidal currents flow along the SRR structure. As a result, the SRR structure can be regarded as a resonant magnetic dipole. In addition, SRR structure localizes the incident electric field to its close vicinity at the resonance frequency. These two properties of the SRR structure makes it interesting for antenna applications. Due to these two properties of the SRR structure, when arranged in a regular pattern, the resulting metamaterial SRR medium may be regarded as an antenna array. An array antenna is made up of more than one radiating element [70].

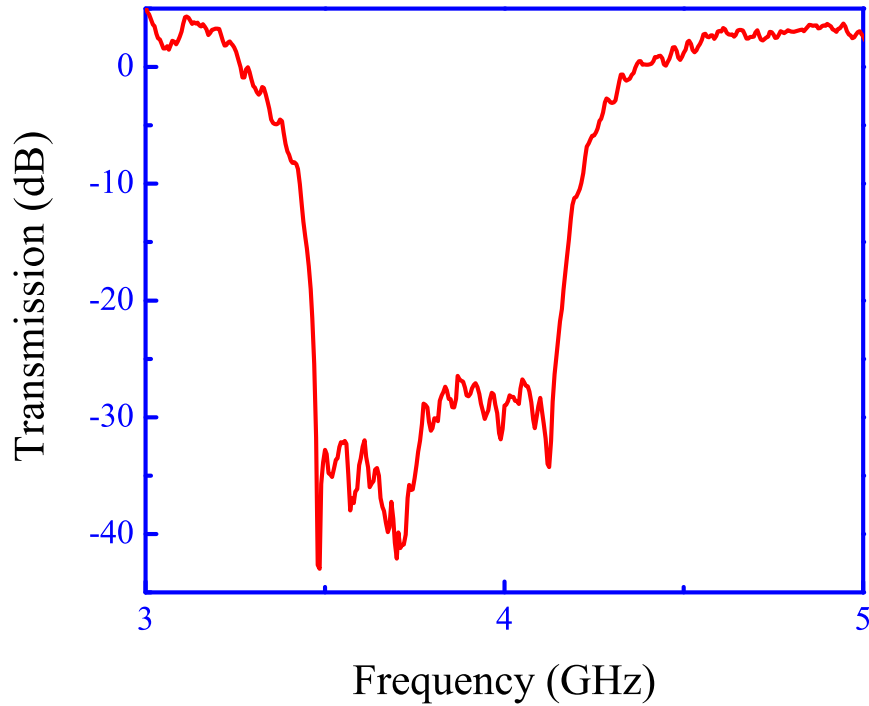


Figure 2.35: Transmission spectrum of the electromagnetic waves through the SRR metamaterial medium. Electric field is oriented along z-axis and the magnetic field is perpendicular to the plane of the SRR structures.

The experimental setup that we used to study the transmission properties of the SRR metamaterial medium is depicted in Figure 2.34 . The transmission setup consists of HP-8510C network analyzer and transmitting-receiving horn antennas. The measured metamaterial medium is obtained by arranging SRR structures in a rectangular array. The periodicity along z- and y-axes is equal to 8.8 mm. The periodicity along x-axis is 6.5 mm. There are 30 layers along x-axis, 15 layers along z-axis, and 15 layers along y-axis. The distance between horn antennas and the structure is 15 cm, which is larger than the wavelength at 3 GHz. The measured transmission spectrum of the SRR metamaterial medium is shown in Figure 2.35. The orientation of the incident fields and the SRRs is such that the magnetic field is perpendicular to the plane of SRRs and electric field is oriented along z-axis. The transmission spectrum of the metamaterial

SRR medium exhibits a band-gap between 3.4 GHz and 4.3 GHz.

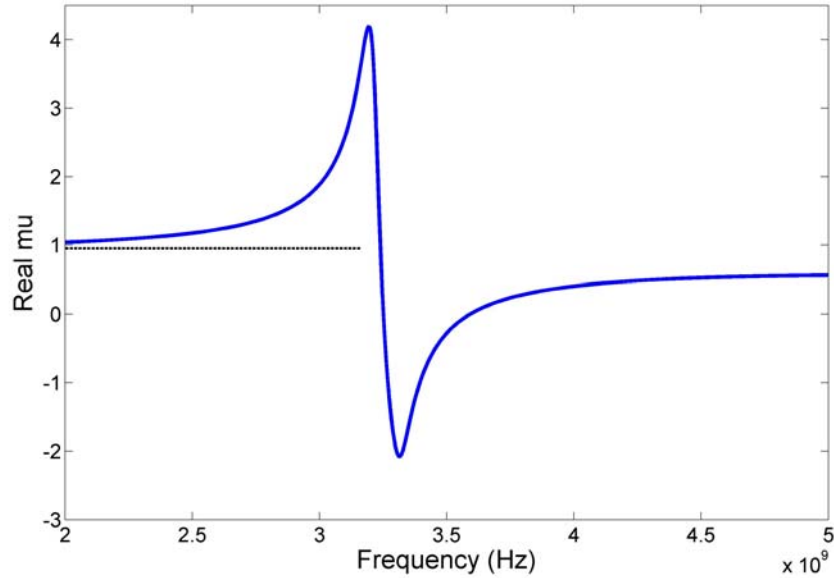


Figure 2.36: Real part of the effective permeability for the split-ring resonator based medium that we used in our study.

In addition to the transmission measurements and calculations, we also performed the retrieval calculations on the SRR metamaterial medium shown in Fig. 2.34. We plotted our results in Fig. 2.36. The effective permeability is positive below 3.25 GHz and approaches to the value of 1 at low frequencies. The values of the permeability between 3.25 GHz and 3.6 GHz are negative. The comparison of the results shown in Fig. 2.33 and Fig. 2.36 indicates some inconsistency. This inconsistency is due to the ambiguity in the dielectric constant of the printed circuit board.

2.6.2 Near field distribution of the electric field emitted from a source that is embedded inside a SRR based medium

One usually expects that the field intensity decreases strongly with the distance from the source. This means that when the surface is considered as a collection of individual antennas, the contribution of each antenna to the emitted radiation decreases with distance from the monopole antenna. In order to check the above statement we measured the electric field intensity near the surface of the SRR array when the monopole source was placed inside the SRR array. In our measurements we used another monopole antenna as a receiver to measure the electric field intensity. The measurements are carried out over an area of $150 \times 20 \text{ mm}^2$ with steps of 1 mm. The data for the resonance frequency is shown in Fig. 2.37 (a). At the resonance frequency a significant part of the surface contributes to the radiation appreciably. On the other hand, at the off-resonance frequency (4.7 GHz) a small part of the surface contributes to the radiation (Fig. 2.37 (b)).

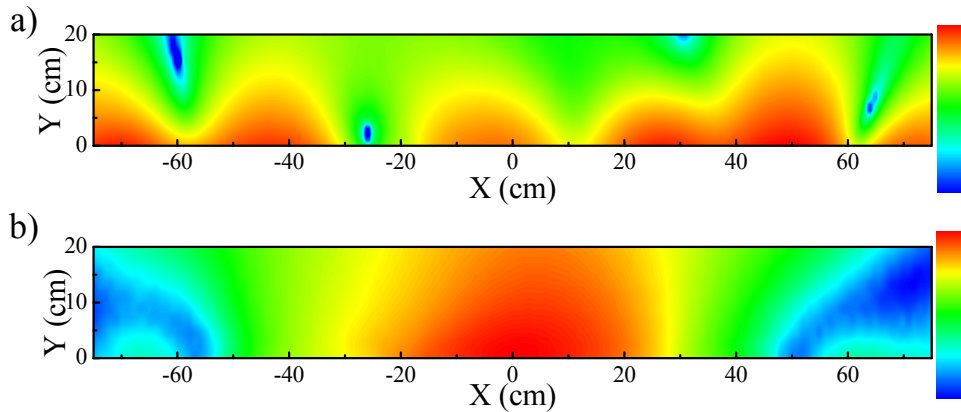


Figure 2.37: a) Measured electric field intensity near the surface of the SRR array at 3.8 GHz when the source is located inside the array b) measured electric field intensity near the surface of the SRR array at 4.7 GHz when the source is located inside the array.

2.6.3 Angular distribution of electric field emitted from a source that is embedded inside the metamaterial medium

For the far field radiation pattern measurements, we replaced the transmitting horn antenna with a monopole antenna and placed the monopole antenna inside the SRR metamaterial medium. The placement of the monopole antenna inside the SRR metamaterial medium was chosen such that the monopole antenna effectively excites the SRR structures at the surface of the medium. As a result, there are 3 layers of SRR planes in front of the monopole antenna. The orientation of the monopole antenna was along z-axis. The monopole antenna was placed at the middle of the SRR array along x-axis and z-axis. Hence, there are 15 SRR layers to the left and to the right of the monopole along x-axis. Along the z-axis, there are 7 layers above and below the center of the monopole antenna. Given the above dimensions, the surface of the SRR metamaterial medium was 2 wavelength long along the y- and z-axis. The power spectrum of the radiation emitted by the monopole antenna was then measured at a distance of 1.5 meters away from the metamaterial SRR medium. The measurements were done by varying the angle in the x-y plane. Figure 2.38 (a) shows the measured angular distribution of power near the resonance frequency of a single SRR structure. The half power beamwidth was approximately 14 degrees for the frequencies near the resonance frequency. These results show that the emitted power is confined to a narrow angular region near the resonance frequency. The experimental far field radiation pattern near the pass-band frequencies is presented in Figure 2.38 (b). Figure 2.38 (b), on the other hand, shows that the emitted power at the pass-band does not show a highly directional radiation pattern. The half power beamwidth at 4.7 GHz is 36 degrees. In a previous work, we showed that photonic crystals may be used to obtain highly directive radiation from sources [71]. Also, Enoch *et. al.* reported similar results by using a metallic mesh of thin wires [66]. The results of both of these previous works are related to the anisotropy of the band structure associated with the wave propagation inside photonic crystals. A physical explanation of highly directive radiation from sources embedded inside photonic crystals is provided by Chigrin *et. al.* in terms of stationary phase [72].

In addition several other researchers have reported directional radiation sources based on photonic crystals [73, 74, 75, 76]. On the other hand, the highly directional radiation near the resonance frequency from a source embedded inside an SRR array is due to the resonant behavior of the individual SRRs. It is worth to compare these values with our previous results obtained by using photonic crystals. For the case of the photonic crystal, the radiation surface had an area equal to $44\lambda^2$, where λ is the operation frequency. On the other hand, the surface area in this work is only $3.8\lambda^2$. This means that the surface area is approximately reduced by a factor of 11 times when compared to the photonic crystals that are composed of regular arrays of dielectrics or wire arrays. We believe that this improvement is important for compact size highly directional radiation sources.

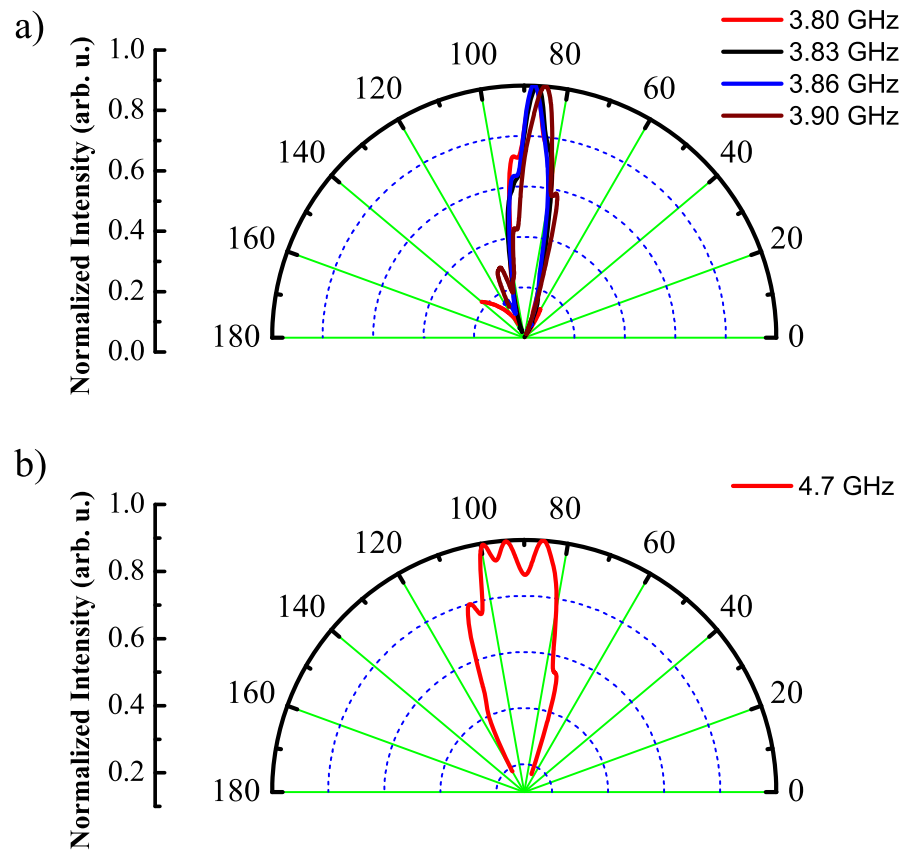


Figure 2.38: a) Far field radiation pattern in the H-plane near the resonance frequency of the SRR structure. b) Far field radiation pattern in the H-plane at an off resonance frequency. Frequency for this plot is 4.7 GHz.

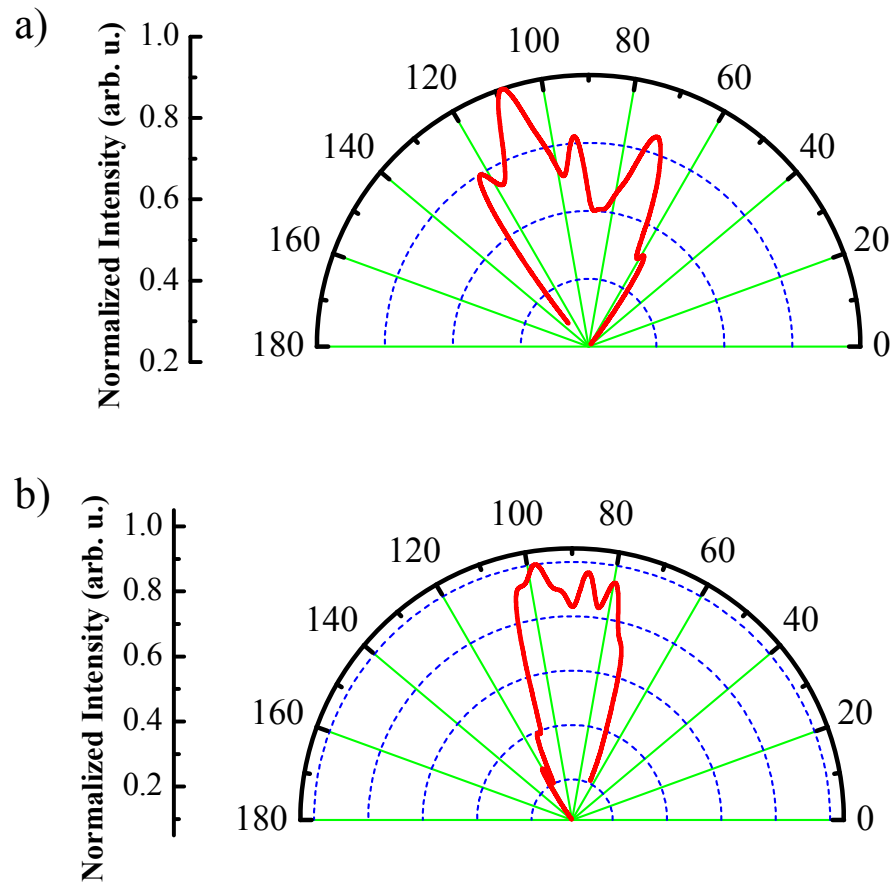


Figure 2.39: a) Far field radiation pattern in the E-plane near the resonance frequency of the SRR structure. b) Far field radiation pattern in the E-plane at an off resonance frequency. Frequency for this plot is 4.7 GHz.

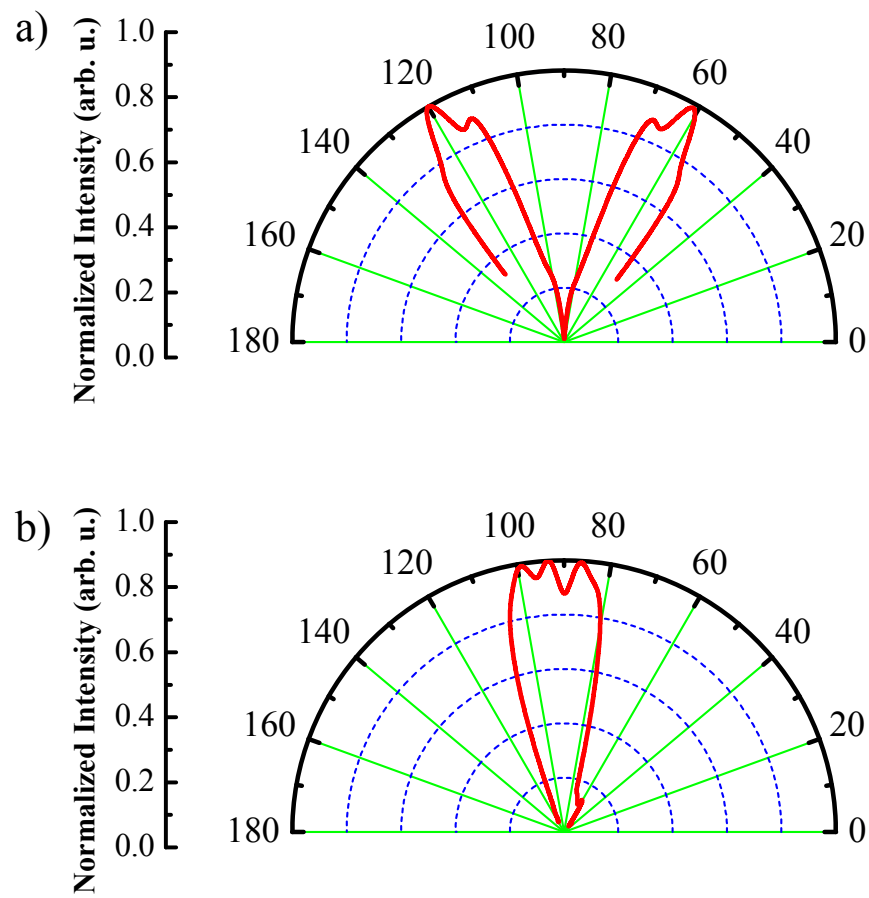


Figure 2.40: a) Far field radiation pattern in the H-plane from a source embedded inside CRR array near the resonance frequency of the SRR structure. b) Far field radiation pattern in the H-plane from a source embedded inside CRR array at 4.7 GHz.

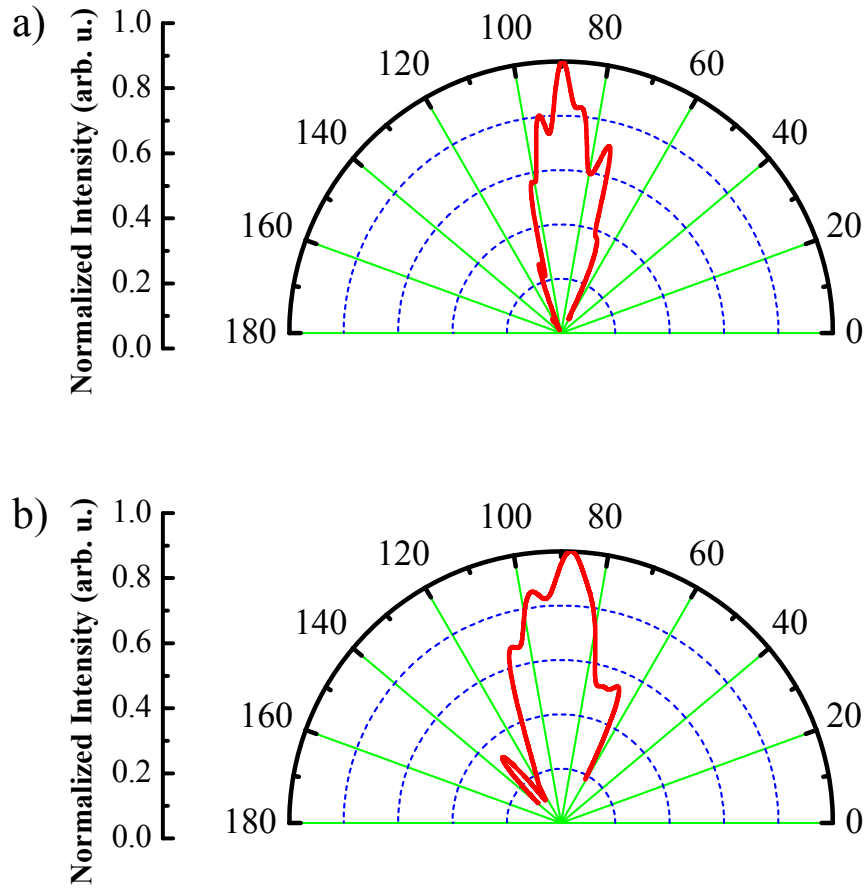


Figure 2.41: a) Far field radiation pattern in the E-plane from a source embedded inside CRR array near the resonance frequency of the SRR structure. b) Far field radiation pattern in the E-plane from a source embedded inside CRR array at 4.7 GHz.

We also checked the coupling efficiency of the monopole antenna by measuring the S_{11} values. The measured S_{11} values when the source is placed inside the SRR array and in free space is shown in Fig. 2.42. The measured S_{11} values at the resonance frequency is -5 dB when the source is placed in free space. On the other hand, when the source is located inside the SRR array S_{11} values reduces down to -24 dB at the resonance frequency. These results clearly indicate that the coupling efficiency is enhanced appreciably when the source is placed inside the

SRR array. The coupling efficiency is quite important for practical applications. The enhanced coupling efficiency may be attributed to the high local electric fields near the SRRs.

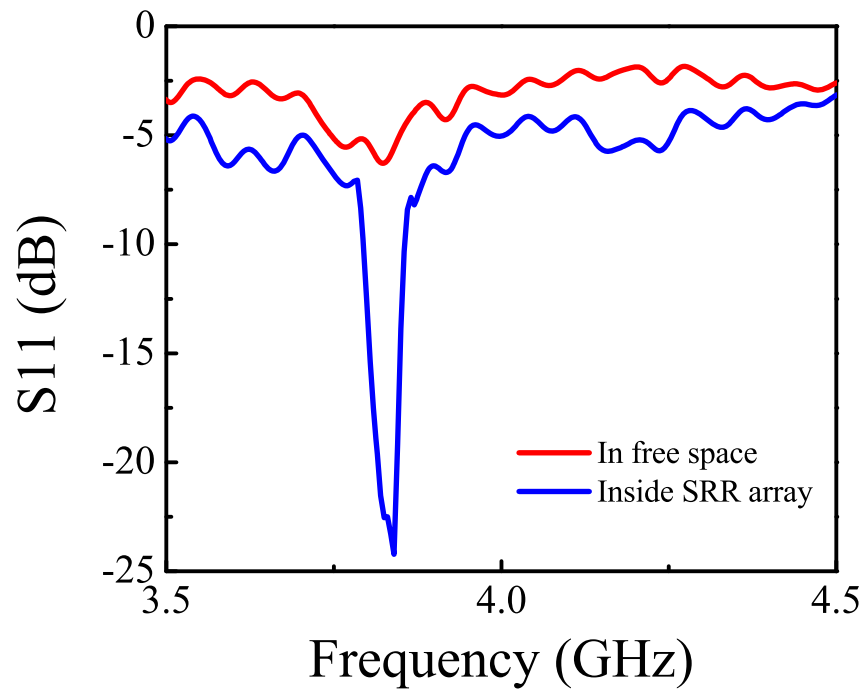


Figure 2.42: Measured S11 for the monopole source in free space (red curve) and for the monopole when the source is located inside the SRR array (blue curve).

Chapter 3

Photonic Crystals

3.1 Introduction

Photonic crystals can be defined as a periodic modulation of the permittivity and/or permeability function. An example of a photonic crystal is shown in Fig. 3.1. At this point this definition does not differentiate a photonic crystal from a metamaterial. But, the difference is strongly pronounced when we note that the periodicity of a photonic crystal is comparable to or larger than the wavelength of interest. Electromagnetic properties of such a structure can not be described in terms of effective parameters, i.e., the medium can not be homogenized. The periodic modulation means that we can describe the properties of a photonic crystal in terms of Bloch modes. That is, the solution to the Maxwell equations in the presence of a periodic modulation:

$$\frac{1}{\epsilon(\mathbf{r})} \nabla \times \{ \nabla \times \mathbf{E}(\mathbf{r}) \} = \frac{\omega^2}{c^2} \mathbf{E}(\mathbf{r})$$
$$\nabla \times \left\{ \frac{1}{\epsilon(\mathbf{r})} \nabla \times \mathbf{H}(\mathbf{r}) \right\} = \frac{\omega^2}{c^2} \mathbf{H}(\mathbf{r}) \tag{3.1}$$

$$\epsilon(\mathbf{r} + \mathbf{a}) = \epsilon(\mathbf{r}) \tag{3.2}$$

where \mathbf{a} is the periodicity of the photonic crystal, can be written as the so called Bloch solutions or modes:

$$\begin{aligned}\mathbf{E}_{\mathbf{k}n}(\mathbf{r}) &= \mathbf{u}_{\mathbf{k}n}(\mathbf{r}) \exp(i\mathbf{k} \cdot \mathbf{r}) \\ \mathbf{H}_{\mathbf{k}n}(\mathbf{r}) &= \mathbf{v}_{\mathbf{k}n}(\mathbf{r}) \exp(i\mathbf{k} \cdot \mathbf{r})\end{aligned}\quad (3.3)$$

$$\{\mathbf{u}_{\mathbf{k}n}(\mathbf{r} + \mathbf{a}), \mathbf{v}_{\mathbf{k}n}(\mathbf{r} + \mathbf{a})\} = \{\mathbf{u}_{\mathbf{k}n}(\mathbf{r}), \mathbf{v}_{\mathbf{k}n}(\mathbf{r})\} \quad (3.4)$$

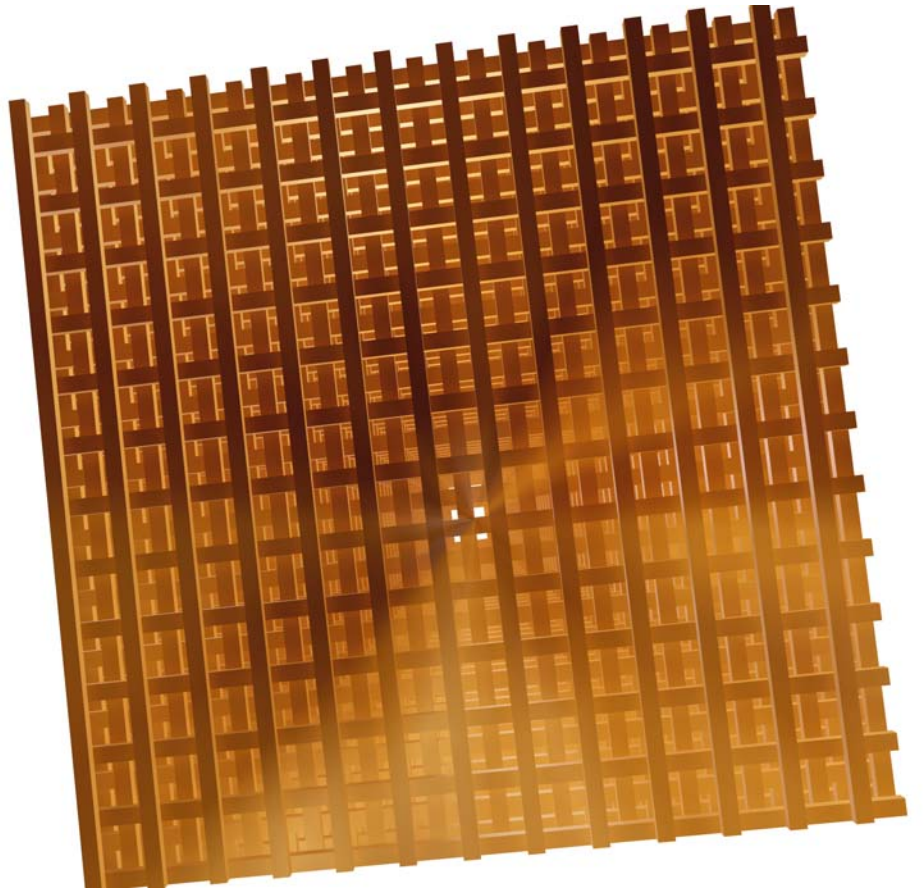


Figure 3.1: The layer-by-layer photonic crystal. This structure is described the face cubic tetragonal lattice (FCT).

In eqn. 3.3, \mathbf{k} is the wave vector and n is the band index. There are n solutions corresponding to each wave vector. These solutions are expressed as an eigenvalue, which is the $\omega_{\mathbf{k}n}$, and an eigenvector, $\mathbf{u}_{\mathbf{k}n}(\mathbf{r})$, $\mathbf{v}_{\mathbf{k}n}(\mathbf{r})$. We can think of

these solutions as a plane wave modulated by a periodic function, $\mathbf{u}_{\mathbf{k}n}(\mathbf{r})$, $\mathbf{v}_{\mathbf{k}n}(\mathbf{r})$. The Bloch modes or solutions can be calculated by several techniques one of which is the plane wave method [77]. This method solves the above equations by expressing the dielectric function, $\epsilon(\mathbf{r})$, and $\mathbf{u}_{\mathbf{k}n}(\mathbf{r})$, $\mathbf{v}_{\mathbf{k}n}(\mathbf{r})$ in terms of Fourier series.

Photonic crystals strongly modify the dispersion properties of electromagnetic waves (EM) waves. Since PCs may control the propagation of EM waves in certain directions, they have recently attracted much attention. Many interesting phenomena such as enhancement and suppression of spontaneous emission [78], propagation of photons via hopping over coupled defects [79], and localized donor and acceptor modes [80], have been suggested and observed. One particular application of photonic crystals has been commercialized by Samsung to increase the extraction efficiency of light emitting diodes (LEDs) [81].

In this chapter, we will experimentally and theoretically demonstrate two novel phenomena arising from the dispersion properties of the photonic crystals. One of these phenomena is the existence of the surface modes. We will demonstrate that a proper termination of the photonic crystal may lead to modes that are bound to the surface of the photonic crystal. We will further show that these modes may be useful in certain applications such as enhanced transmission through sub-wavelength apertures and beaming of electromagnetic waves. Another phenomena that we will demonstrate is the negative refraction effect. I shall point out that the negative refraction effect that we will show in this chapter is fundamentally different than the one we observed in the previous chapter.

3.2 Beaming of Light and Enhanced Transmission via Surface Modes of Photonic Crystals

A metallic surface and the surface of a corrugated PC have a similar property, i.e., both surfaces can support surface propagating electromagnetic waves [82, 83]. The properties of the surface propagating modes on metallic surfaces have

been extensively studied. Recently, extraordinary light transmission through a subwavelength aperture on a metallic surface surrounded by concentric grooves or a grating has been demonstrated [84, 85]. This extraordinary transmission is attributed to the excitation of surface modes on the metallic surface. In addition to the extraordinary transmission, beaming of electromagnetic waves via surface modes on the metallic surfaces have been reported [86, 87, 88, 89].

In this section, we theoretically show that PC surface can support surface propagating EM waves in the presence of a periodic corrugation. We experimentally demonstrate high transmission amplitudes through PC waveguides when a surface corrugation is added to the input surface of the PC. The enhanced transmission is attributed to the excitation of the surface modes. In addition, our far field radiation pattern measurements show that when a periodic corrugation is added to the output surface of the PC, the power emitted through the PC waveguide is confined to a narrow angular region.

3.2.1 Theoretical and Experimental demonstration of Surface Propagating Modes

Modes of an infinite photonic crystal can be calculated by using the plane-wave expansion method [77]. The same method can be used to identify the modes of a finite photonic crystal by employing a large enough supercell [90]. Figure 3.2 (a) shows the results of band structure calculations for the photonic crystal that we used in our study. The photonic crystal is a 2 dimensional square array of circular alumina rods. The crystal is assumed to be continuous along z axis in our band structure calculations. The radius of the rods is 1.55 mm. The dielectric constant of alumina is 9.61. Lattice constants along x and y directions are 11 mm. The supercell is 40 layers long along y axis and consists of 1 unit cell along x axis. 15 unit cells along y axis contains alumina rods and the rest is free space. For comparison, we calculated the band structure of an infinite photonic crystal, i.e., infinite both in x axis and y axis (inset of Fig. 3.2 (a)). The modes of a finite size photonic crystal can be classified into 3 parts: 1) modes extending both in air and

PC (Fig. 3.3 (a)), 2) modes extending in air but decaying in PC (Fig. 3.3 (b)), 3) modes decaying in air but extending in PC (Fig. 3.3 (a)). Only the modes that are extending both in air and PC are observed in the transmission spectrum.

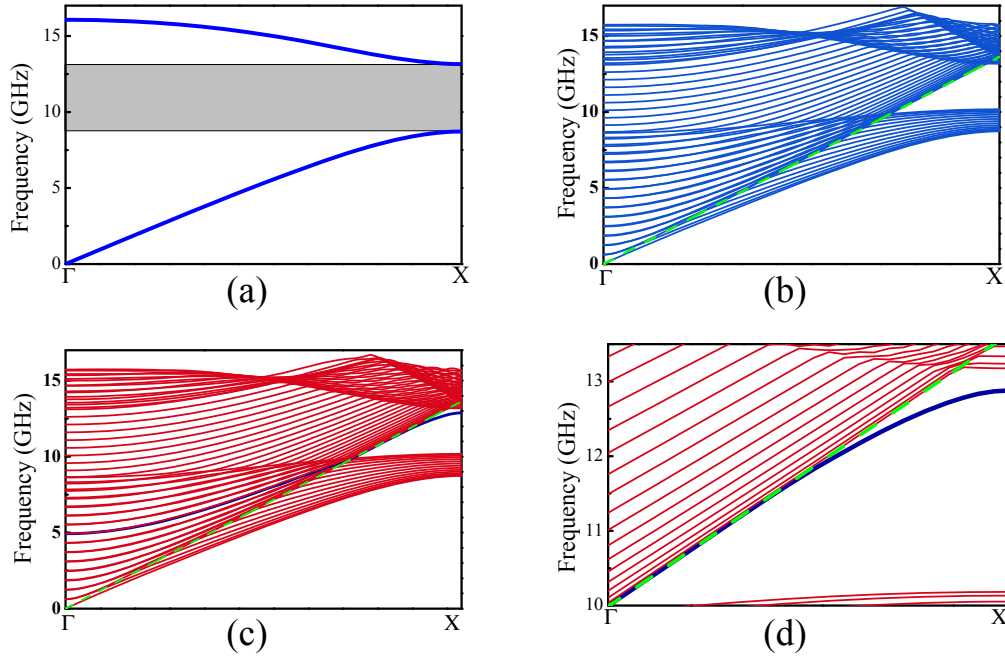


Figure 3.2: a) The TM (electric field parallel to the axis of the rods) band structure of the infinite size PC b) the TM band structure of the finite size c) the TM band structure of the finite size PC when the radius of the rods at the surface of the PC is reduced to 0.76 mm. d) zoomed view of the TM band structure of the finite size PC when the radius of the rods at the surface of the PC is reduced to 0.76 mm.

The PC surface supports surface propagating waves when an appropriate corrugation is added [82]. The corrugation may be achieved by reducing the rod radius at the surface of the PC or by using rods of different shape. For this study we changed the radius of the rods at the surface of the PC from 1.55 mm to 0.76 mm. The band structure of the corresponding PC is calculated by plane wave expansion method with a large supercell (Fig. 3.2 (b)). Figure 3.2 (b) shows that when the corrugation is added a band below the light line appears in the band structure (This band is shown with blue solid line in Fig. 3.2 (c) and (d)).

This band is inside the photonic band gap and extends from 11.9 GHz to 12.8 GHz. The electric field corresponding to these modes is calculated and plotted in Fig. 3.3 (d). Figure 3.3 (d) shows that the electric field for these modes is evanescent both in air and inside PC. However, these modes have real wave vectors parallel to the PC surface. As a result, these modes are surface propagating waves.

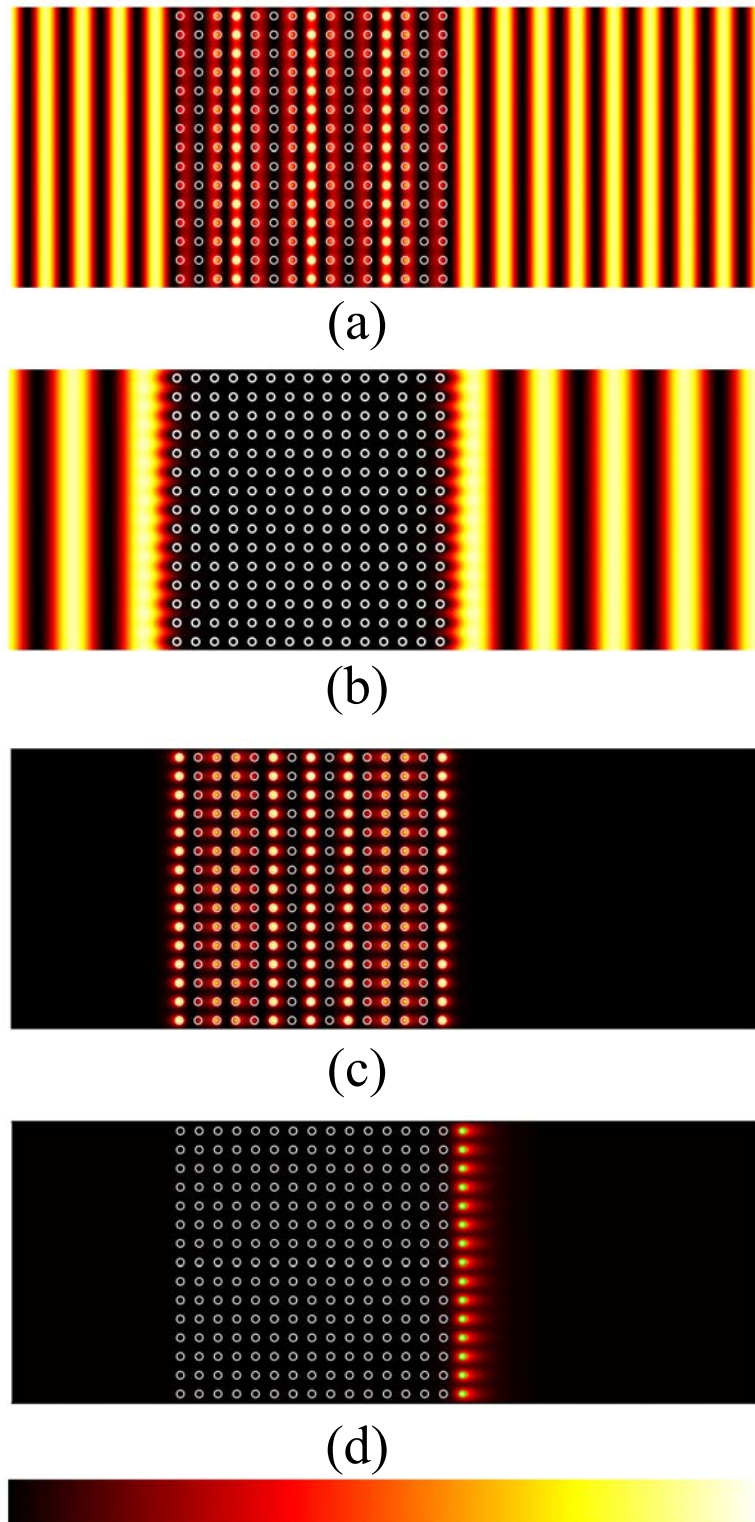


Figure 3.3: Modes of the finite size PC a) electric field profile of mode extending both in air and PC b) electric field profile of mode extending in air but decaying in PC c) electric field profile of mode decaying in air but extending in PC d) electric field profile of surface mode

Since the surface propagating modes lie below the light line (Fig. 3.2 (b)) they can not be excited by incident plane waves. These modes can be excited by two mechanisms. First mechanism is to couple the surface modes evanescently by using a prism configuration [91]. Second mechanism is to couple via wave vector conversion. Wave vector conversion can be achieved by adding a grating-like structure to the surface of the corrugated PC, i.e., by adding an extra layer with a suitable lattice constant. In this study, we used the second method. We added an extra layer in front of the corrugated PC surface. The added layer is composed of alumina rods with a radius of 1.55 mm and a lattice constant of 22 mm. The coupling to the surface modes of the PC can then be observed by measuring the reflection spectrum. The photonic crystal structure is shown in Fig. 3.4. We measured the reflection spectrum by using HP-8510C vector network analyzer and transmitting-receiving horn antennas. The details of the reflection and transmission measurements are explained elsewhere [92, 93]. The measured reflection spectrum is shown in Fig. 3.5. Both the uncorrugated and corrugated PC effectively reflect the incident EM waves. This can be compared to the band structure shown in the inset of Fig. 3.2 (a). On the other hand, when the grating-like layer is added to the surface of the corrugated PC, the resulting structure exhibits a dip in the reflection spectrum around 12.4 GHz. The magnitude of the reflection coefficient is -32 dB at 12.4 GHz. The dip in the reflection spectrum clearly shows that due to the grating-like structure the incident EM waves effectively couples to the surface modes of the corrugated PC around 12.4 GHz.



Figure 3.4: The photonic crystal structure that we used in the study of surface modes.

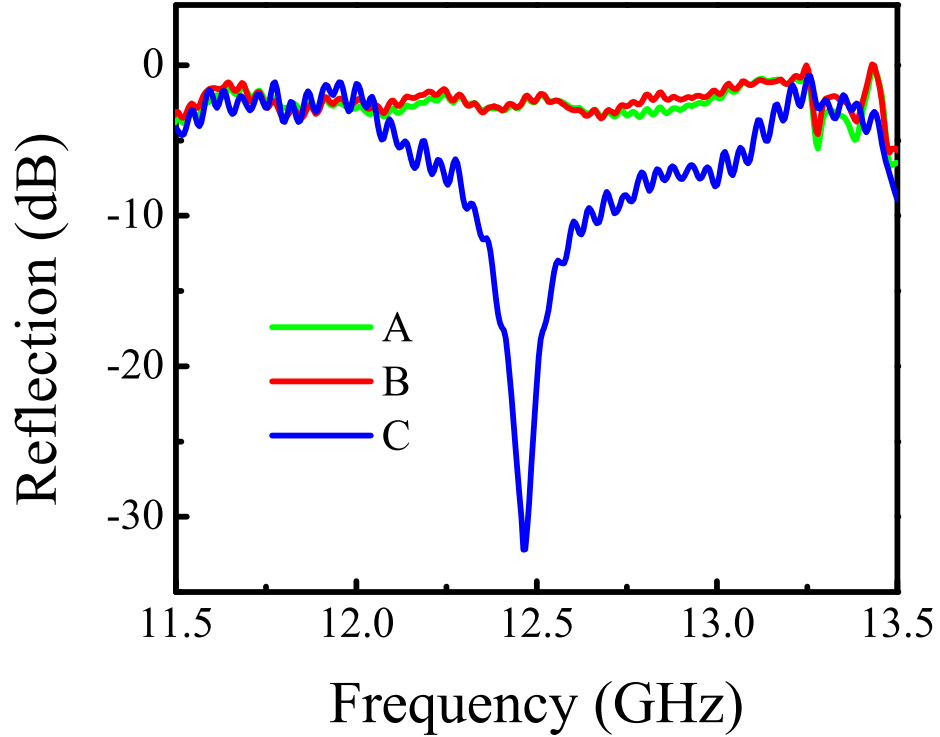


Figure 3.5: Measured reflection spectrum from (A) bare photonic crystal surface (B) from the corrugated layer added PC surface (C) from the corrugated PC surface when the grating-like structure is added

3.2.2 Enhanced Transmission Through PC Waveguide via Surface Modes

An important component of the photonic devices is waveguides. Previously, several waveguide structures based on photonic crystals have been proposed and demonstrated [94, 95]. The PC based waveguides are usually obtained by removing either a complete row from the PC or by creating coupled defects. One major problem with the PC based waveguides is the low transmission efficiency. The low transmission efficiency is usually attributed to the poor coupling between the

incident wave and the waveguide modes of the PC waveguide. Several methods have been suggested to overcome this problem.

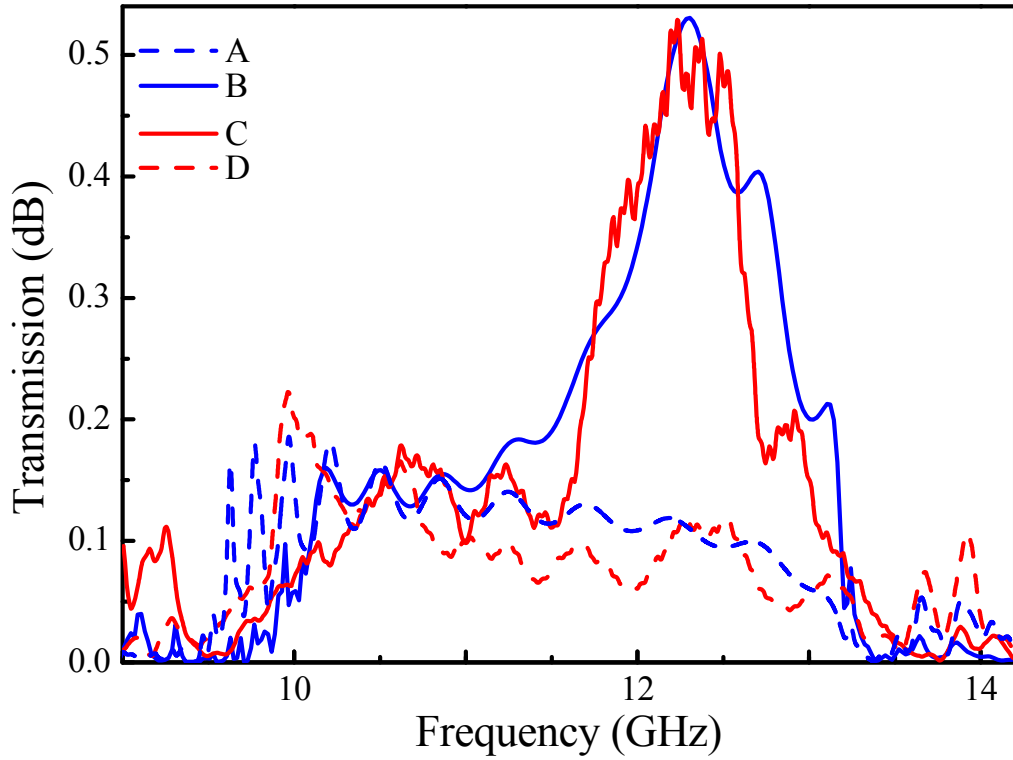


Figure 3.6: A) The measured transmission spectrum through the PC waveguide, B) the calculated transmission spectrum through the PC waveguide, C) the measured transmission spectrum through the PC waveguide when the surface corrugation and the grating-like structure is added in front of the input surface of the PC waveguide, D) the calculated transmission spectrum through the PC waveguide when the surface corrugation and the grating-like structure is added in front of the input surface of the PC waveguide

Recently, enhanced transmission through sub-wavelength metallic apertures surrounded by concentric grooves or a grating has been demonstrated by several researchers [84, 85]. The concentric grooves or the grating is used to excite the surface propagating modes on the metal. It has been suggested that surface modes play an important role in the enhanced transmission. A similar idea has

been suggested to increase the transmission efficiency of a PC waveguide [96].

We obtained the PC waveguide by removing one row of rods from a 21×15 square array of circular alumina rods. The crystal is 15 layers long along the propagation direction. The measured and calculated transmission spectrum through the PC waveguide is shown in Fig. 3.6. A waveguide band between 9.7 GHz and 13.1 GHz is observed in the transmission spectrum of the PC waveguide. The overall transmission efficiency is around %10 when compared to free space transmission. At 12.45 GHz the transmission efficiency is %11. These results show that the transmission efficiency of the PC waveguide is low.

We added an extra layer of rods with a radius of 0.76 mm to the input surface of the PC. As we showed in the previous section addition of this extra layer creates surface modes. In order to couple to the surface modes, we added the same grating-like layer explained in the previous section in front of the extra layer. Note that the grating-like layer results in efficient coupling to the surface propagating modes around 12.45 GHz (Fig. 3.5). The measured and calculated transmission spectrum through the PC waveguide with the input surface modulation is shown with solid curves in Fig. 3.6. The transmission efficiency is increased by a factor of 5 around 12.45 GHz when compared to the bare PC waveguide. Specifically, the transmission through the bare PC waveguide was %11 at 12.45 GHz. This value is increased to %53 for the PC waveguide with the surface modulation. These results indicate that efficient coupling to the PC waveguide modes can be achieved via surface propagating waves.

3.2.3 Beaming of EM Waves by Photonic Crystal Surface Modes

The EM waves emitted through a sub-wavelength aperture have a broad angular distribution, i.e., EM waves quickly diffract in all directions [97]. Recently, it has been shown that when a sub-wavelength aperture on a metal surface is dressed with a grating or concentric grooves, the EM waves emerging from the sub-wavelength aperture is confined to a narrow spatial region [86, 87, 88, 89].

This phenomenon is usually called beaming. The beaming effect is attributed to the surface plasmon diffraction. It has been suggested that beaming is observed for wavelengths at which the wave vector of the surface plasmon is smaller than the grating vector.

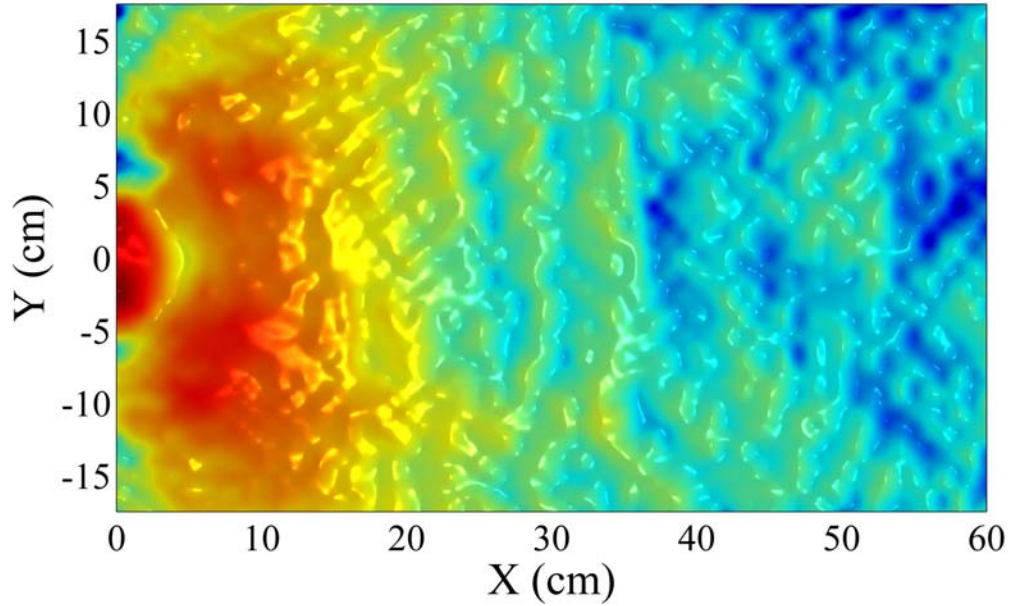


Figure 3.7: The measured intensity distribution at the exit side of the PC waveguide. Y-axis is parallel to the PC surface.

The photonic crystal waveguide that we used in this study has a width smaller than the operation wavelength. The operation wavelength is around 2.5 cm, whereas the waveguide width is 1.9 cm. Hence, it is expected that the EM waves emitted through the PC waveguide would diffract in all directions from the PC waveguide aperture. We measured the intensity of the EM waves emitted through the PC waveguide over a rectangular area of 35×60 cm. Measurement setup consists of transmitting horn antenna and receiving monopole antenna. The PC waveguide is excited with the incident waves emitted through the transmitting horn antenna. Electric field intensity is measured on the exit side by using the monopole antenna with 0.5 cm steps, which results in 8591 data points. The measured intensity distribution at 12.45 GHz is shown in Fig. 3.7. The data shows that the EM waves emitted through the PC waveguide quickly diffract in

all directions.

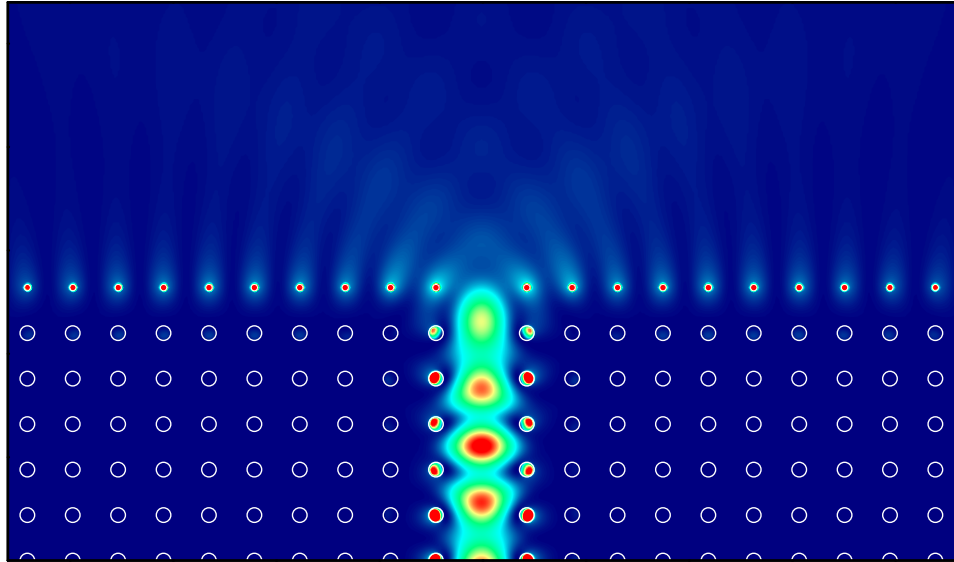


Figure 3.8: Calculated field intensity when the surface corrugation is added to the exit surface of the PC waveguide.

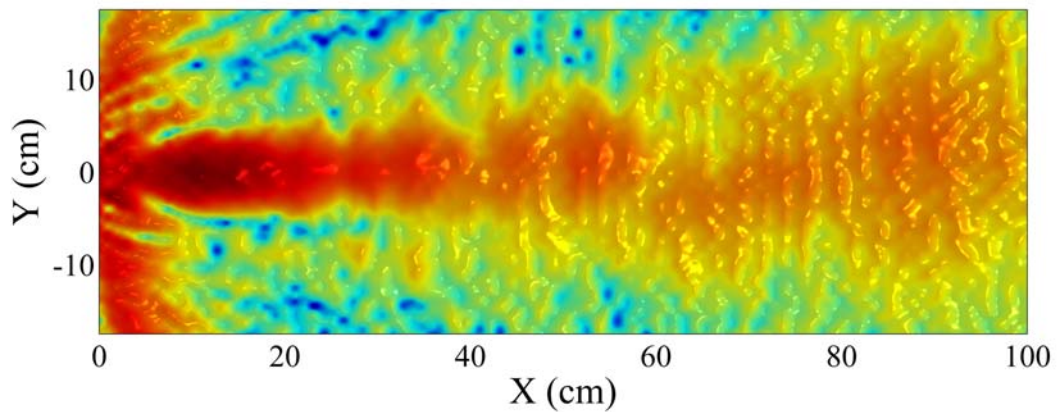


Figure 3.9: The measured intensity distribution at the exit side of the PC waveguide when the corrugation and grating-like layer are added to the exit surface of the PC waveguide. Y-axis is parallel to the PC surface.

In section 3.2.1, we showed that surface modes can be created on the surface of the PC by changing the radius of the rods on the PC surface. Since the modes

of the PC waveguide decay into the bulk region of the PC, surface modes can be excited by the PC waveguide. Figure 3.8 shows the calculated electric field intensity at 12.45 GHz when the radius of the rods at the exit surface of the PC waveguide is reduced from 1.55 mm to 0.76 mm. The PC waveguide is excited by the incident Gaussian wave. The beam width is 10 lattice constants long. The PC waveguide is 15 lattice constants long along the propagation direction. The field intensity is calculated by FDTD method. The data shows that the surface modes are excited by the PC waveguide. In addition, Fig. 3.8 shows that the surface modes are not coupled to the radiating modes of the free space.

The surface modes excited by the PC waveguide can be coupled to the radiating modes of the free space when a grating-like layer is added in front of the corrugation. We formed the grating-like layer with rods that have equal radius to the bulk PC rods. The grating-like layer has a period of twice the bulk PC period. In section 3.2.1, we showed that such a grating-like layer results in efficient coupling to the surface modes around 12.45 GHz. The measured electric field intensity at 12.45 GHz over a region of 35×50 cm area on the exit side of the PC waveguide in the presence of corrugation and grating-like layer is shown in Fig. 3.9. Figure 3.9 shows that the electric field intensity is confined to a narrow spatial region and propagates without diffracting into a wide angular region. In addition, the measured far field radiation patterns of the EM waves emitted from the PC waveguide with and without surface corrugation and grating-like layer is shown in Fig. 3.10 (a) and (b), respectively. Figure 3.10 shows that without the surface corrugation and grating-like layer the emitted power spreads into a wide angular region. However, Fig. 3.10 (b) shows that with the surface corrugation and the grating-like layer the emitted power is confined to a very narrow angular region with a half power beam width of 10 degrees.

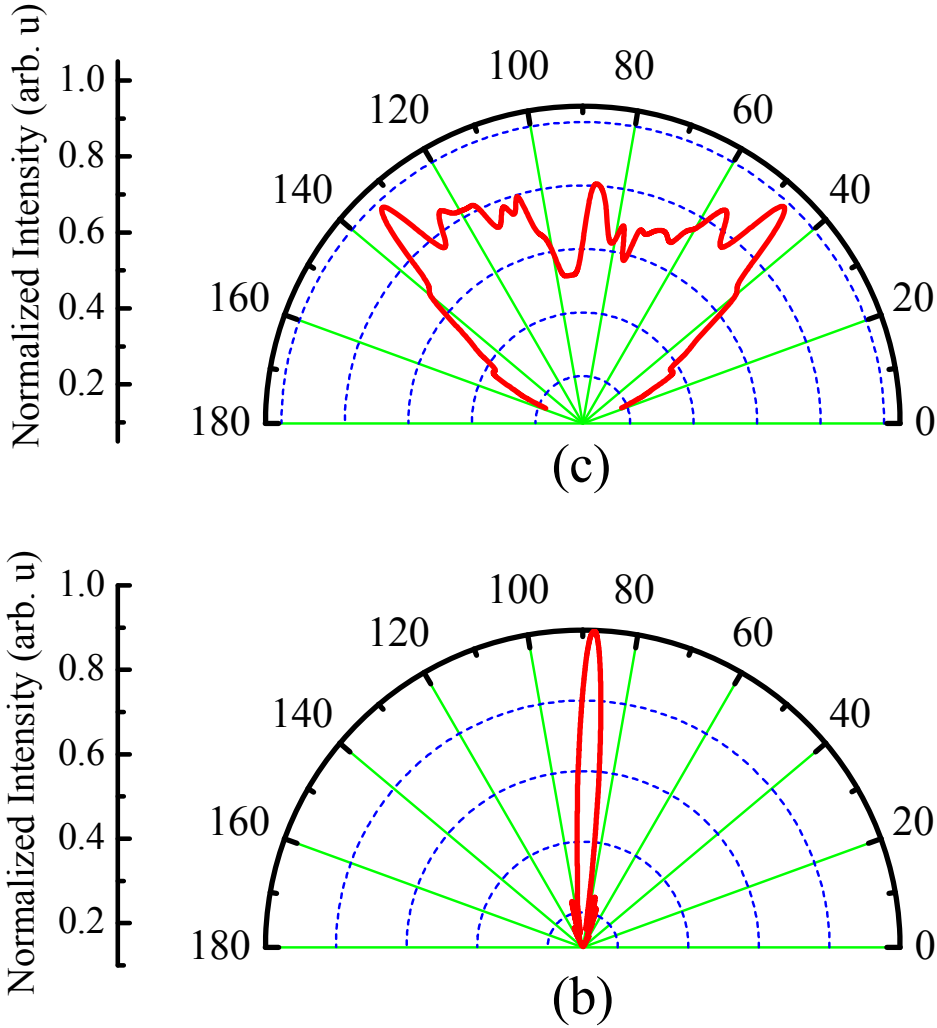


Figure 3.10: a) Measured far field radiation pattern of the EM waves emitted from PC waveguide at 12.45 GHz b) Measured far field radiation pattern of EM waves emitted from the PC waveguide with surface corrugation and grating-like layer

3.2.4 Conclusion

In conclusion of this section, we showed the existence of surface modes when the surface layer of the finite PC is corrugated. The existence of surface modes are experimentally verified by reflection measurements. Enhanced transmission through

the PC waveguide due to coupling to the surface modes have been demonstrated. The measured transmission without surface corrugation was about %10. We observed that the transmission was increased to %55 when the surface corrugation with the grating-like layer was added to the input surface of the PC waveguide. We believe that the enhancement in the transmission can further be increased by using a more optimized surface layer. In addition, we demonstrated that the electric field emitted through the PC waveguide in the presence of the surface corrugation and the grating-like layer was confined to a narrow spatial region. The measured field profiles showed that without the corrugation and grating-like layer the electric field transmitted through the aperture of the PC waveguide diffracts in all angles. Our theoretical results showed that the modes of the PC waveguide were coupled to the surface modes when the surface corrugation was added to the output surface of the PC waveguide. With the corrugation and the grating-like layer in front of the exit surface of the PC waveguide the electric field intensity exhibited the beaming effect.

3.3 Negative Refraction and Focusing of Electromagnetic Waves by Metallodielectric Photonic Crystals

Dispersion properties of photonic crystals provide various means to control the propagation of electromagnetic (EM) waves. In this sense many applications such as waveguides [95, 98, 94], wavelength division multiplexing (WDM) [99, 100, 101, 102], highly directional antennas [71, 103] have been proposed and demonstrated.

An interesting phenomenon arising from the dispersion relation of photonic crystals is the so called negative refraction effect [104, 105, 106, 107, 108, 109]. This effect is observed for frequency ranges at which the wave vector of the incident waves and the group velocity of the transmitted waves fell into the opposite sides of the interface normal [104]. As a result, for such frequency ranges photonic crystal behaves as if the index of refraction is negative.

In order to make use of the negative refraction effect in certain applications such as focusing of electromagnetic waves, one usually requires negative indices of refraction over a wide range of angles. To obtain negative indices of refraction over a wide range of angles is still a major challenge for photonic crystal based structures [106, 107, 108]. In this section we addressed this issue by using a metallodielectric photonic crystal. We showed that by adding a periodic dielectric perturbation to the metallic photonic crystal, one could increase the range of angles at which negative indices of refraction prevail. Furthermore, as an application of the negative refraction effect we demonstrated the focusing effect.

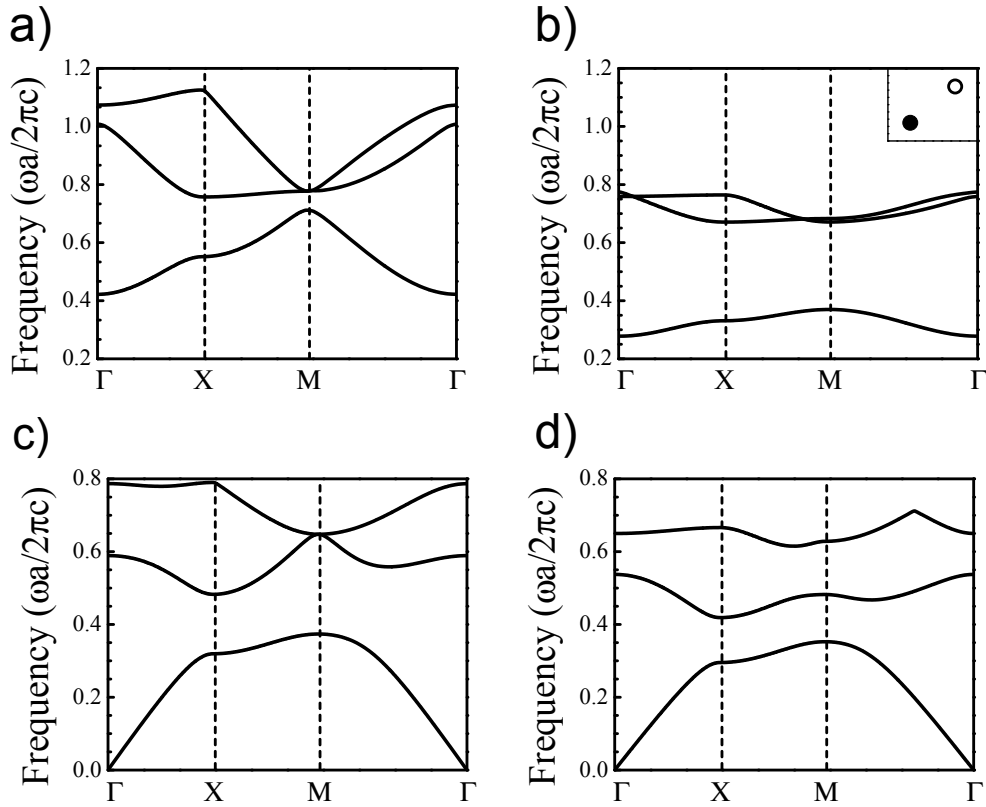


Figure 3.11: The first 3 TM polarized bands for (a) the metallic photonic crystal (b) the metallodielectric photonic crystal (c) the unperturbed dielectric photonic crystal (d) the perturbed dielectric photonic crystal.

3.3.1 The Metallodielectric Photonic Crystal

Luo et. al. [107] used a similar approach to shift the equal frequency surface (EFS) contours in the frequency axes, and theoretically demonstrated all angle negative refraction by embedding metallic rods arranged in a square lattice into a high dielectric constant medium for TM polarized (electric field parallel to the axis of rods) EM waves. The effect of using a high dielectric constant host medium for metallic rods is to increase the effective index of the medium. This results in lowering the EFS contours in frequency, while keeping the area occupied by the EFS contours in the k-space unchanged. Apart from manufacturing difficulties, this approach has some disadvantages. One of these disadvantages is that one has to carefully terminate the surface of the PC. Without a proper termination, the corrugation on the surface of the PC may lead to surface modes [82, 90, 110]. In addition, EM waves incident on the surface of the PC structure will be first refracted by the high dielectric constant host medium. Because of the high index of the host medium, EM waves will be refracted towards the surface normal vector (Γ - M direction for a square lattice tilted by 45°). This refracted beam will be further refracted by the PC structure. EM waves with wave vector directed along Γ - M direction will be refracted along the surface normal vector by the PC structure. As a result the output beam will be directed along the surface normal vector. In our approach, we use a periodic dielectric constant perturbation instead of a high dielectric constant host medium. Periodic dielectric constant perturbation is achieved by adding a dielectric rod to each unit cell of the metallic PC. Our approach has two major advantages. First of all there is no ambiguity on how to terminate the surface and manufacturing is relatively easy. Second, the problem that we discussed due to the refraction by the high dielectric constant host medium is not present in our structure.

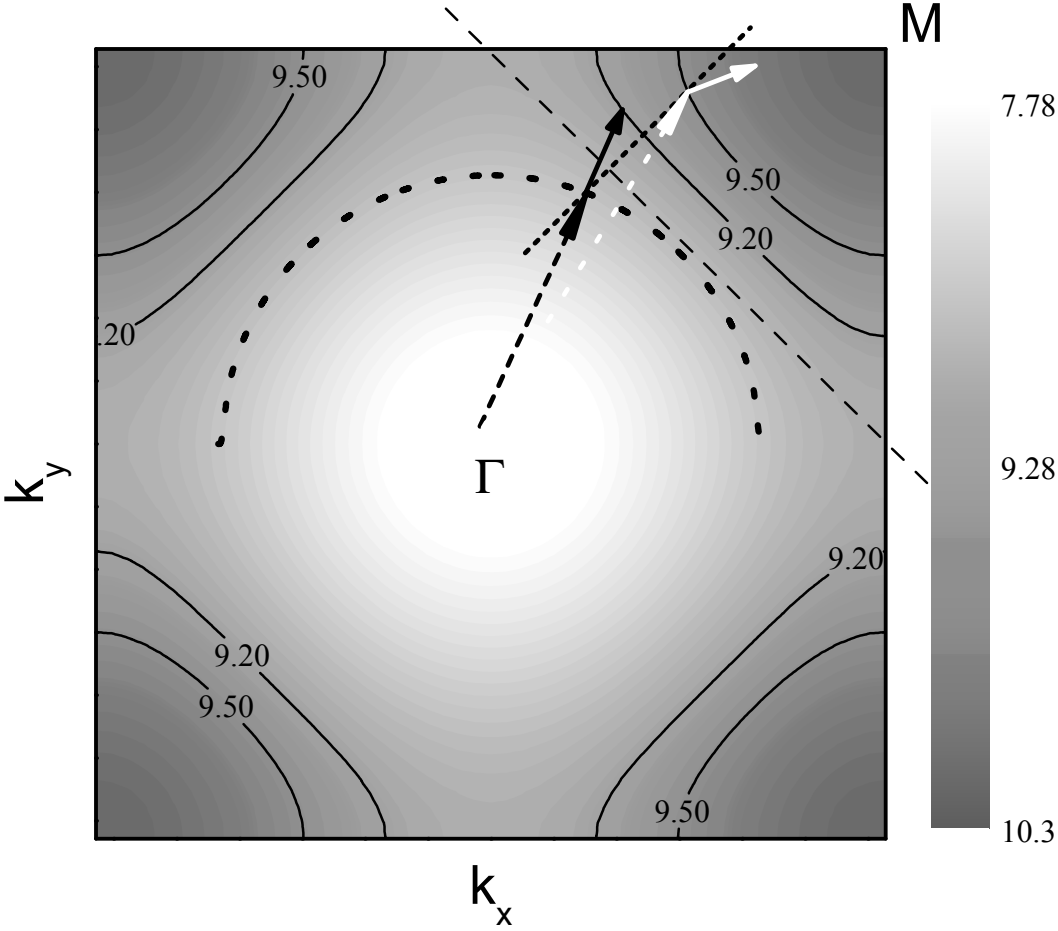


Figure 3.12: Equal frequency contours, solid curves, are shown for the metallodielectric photonic crystal. Crystal orientation is shown by the dashed line. Dotted circle represents the free space equal frequency contour at 9.5 GHz. Frequencies are shown in the GHz scale. Long dashed arrow with black color represents the free space wave vector whereas the short black arrow represents the free space group velocity. Long dashed arrow with white color represents the wave vector of the refracted waves in photonic crystal. Small white colored arrow indicates the direction of group velocity inside photonic crystal.

The metallodielectric photonic crystal that we used in our experiments and

calculations is a square lattice of metallic and dielectric rods. The basis of the crystal consists of a metallic and a dielectric rod placed along the diagonal of the square unit cell (inset of Fig. 3.11 (b)). Cylindrical alumina rods with a radius of 1.55 mm are used for the dielectric rods and in the frequency range of interest the dielectric constant of alumina is 9.61. Metallic (aluminum) rods have a radius of 1.5 mm. Both the metallic and dielectric rods have a height of 15 cm.

One way to view the metallodielectric photonic crystal, especially in the microwave region, is to consider it as a metallic photonic crystal with a periodic dielectric perturbation. It is expected that an attractive perturbation, which corresponds to a positive dielectric constant, will result in lowering of bands [111, 112]. Computed band structures (for TM polarization: electric field is parallel to the axis of rods) for a metallic photonic crystal and a metallodielectric photonic crystal with the same lattice parameters are shown in Figs. 3.11 (a) and (b) respectively. We considered TM polarized EM waves in our calculations and experiments. The dielectric rod used in the calculations is alumina and has a dielectric constant of 9.61. The radius of the dielectric rod is $0.136a$, where a is the lattice constant. The metallic rod is aluminum and has a radius of $0.14a$. Figure 3.11 (b) shows that the bands of the metallodielectric photonic crystal are lowered compared to the bands of the metallic photonic crystal (Fig. 3.11 (a)). For comparison we have calculated the first 3 bands of photonic crystal composed of dielectric rods in a square array (Fig. 3.11 (c)) and a perturbed dielectric crystal with 2 dielectric rods with different dielectric constants (Figs. 3.11 (d)). The unperturbed dielectric PC is composed of alumina rods in a square lattice. The perturbed dielectric PC is obtained by adding a dielectric rod, whose dielectric constant is 3 times smaller than alumina, to the unit cell of the unperturbed dielectric PC. Second and third bands of the perturbed dielectric crystal are appreciably lowered compared to the unperturbed dielectric photonic crystal. However, the first band is only slightly lowered. This can be explained by the fact that the first band is a dielectric band. Since the electric field intensities of these modes have appreciable values only inside the dielectric material, these modes are slightly affected by the perturbation.

Conservation of the surface parallel component of the wave vector suggests

that one way to increase the range of negatively refracted incidence angles is to reduce the radius of free space equal frequency contour. This can be achieved by choosing a lower frequency range at which one expects negative refraction. In addition, the shape and the size of the equal frequency contours for the photonic crystal must be kept unchanged. Hence, lowering the bands without modifying the lattice parameters such as reducing the lattice constant increases the range of incidence angles that are negatively refracted.

3.3.2 Negative Refraction of Electromagnetic Waves by Metallodielectric Photonic Crystal

The computed band structure of the metallodielectric photonic crystal for TM polarization over the first Brillouin zone is plotted in Fig. 3.12. Free space equal frequency contour (dotted circle in Fig. 3.12) and equal frequency contours corresponding to negative refraction are also plotted. Surface of the photonic crystal is aligned such that the normal vector to air-photonic crystal interface is along the $\Gamma - M$ direction. Wave vector of the transmitted waves are found from the conservation of the surface-parallel component of the wave vector. Figure 3.12 shows that for the plotted equal frequency contours, the group velocity of the incident waves and the group velocity of the transmitted waves fall into the opposite sides of the surface normal. Correspondingly, these waves are negatively refracted. For the plotted equal frequency contours, magnitude of the largest surface parallel wave vector component in free space is smaller than the largest surface parallel wave vector component in photonic crystal. In addition, the group velocities in free space and the group velocities in photonic crystal fall into different sides of the surface normal. As a result, for the plotted equal frequency contours EM waves are negatively refracted for all incidence angles.

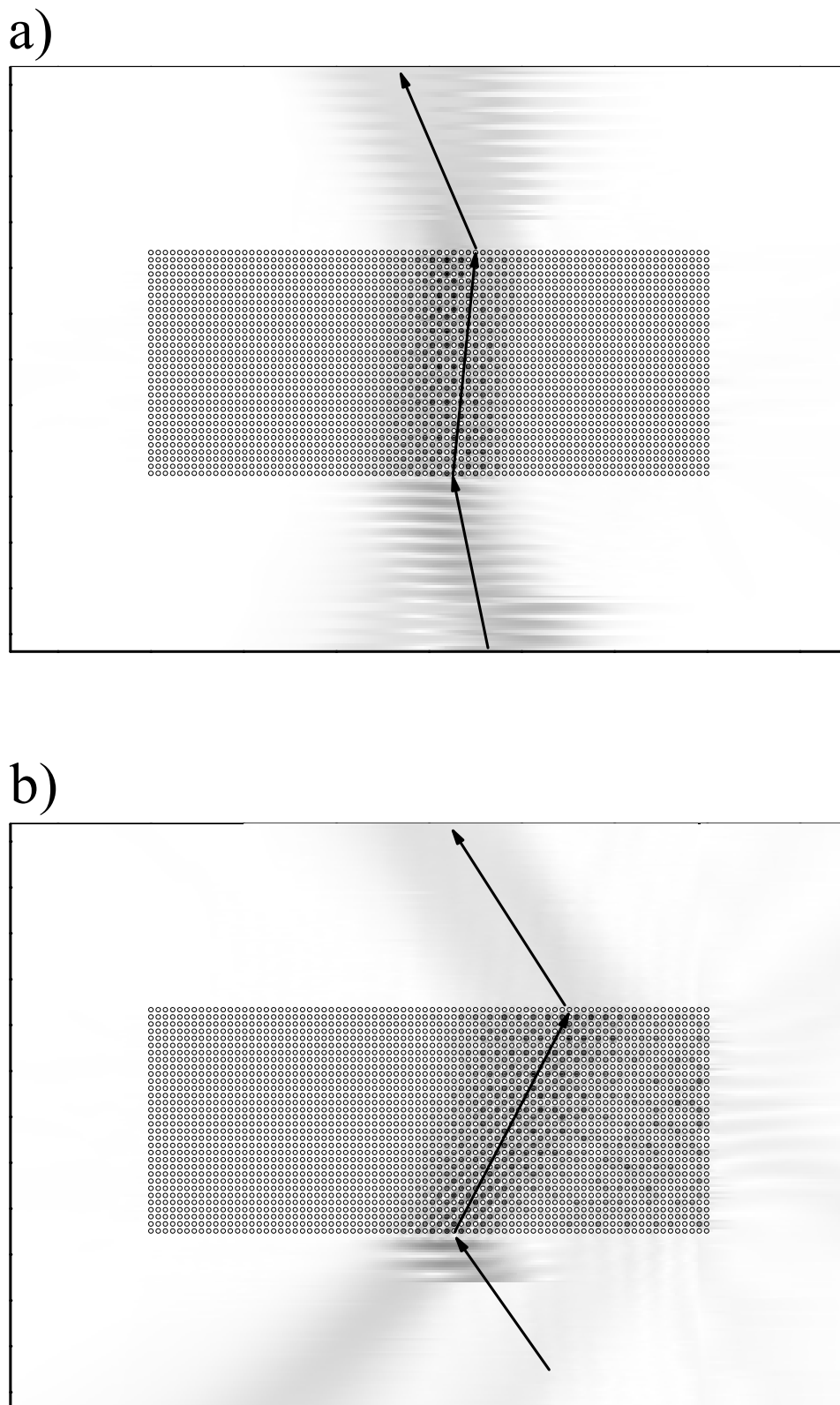


Figure 3.13: a) Electric field distribution for incidence angle 15° b) Electric field distribution for incidence angle 45° . Black represents the maximum field amplitude, whereas white color represents the minimum field amplitude.

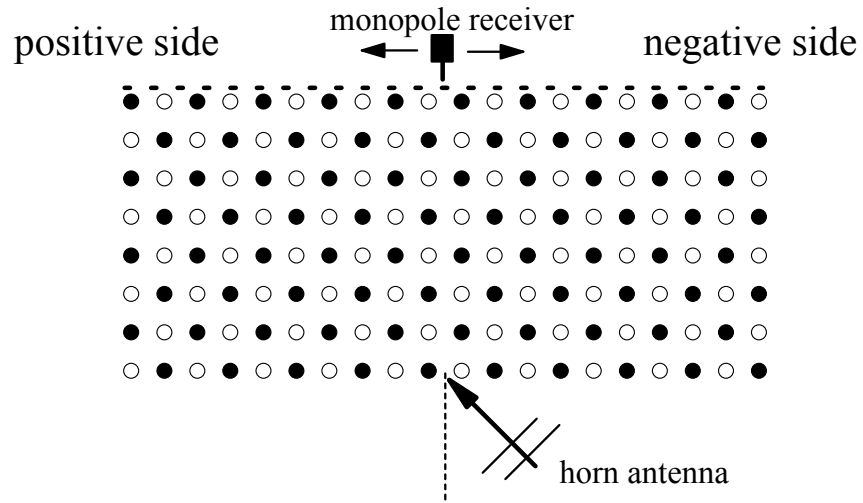


Figure 3.14: Experimental setup for negative refraction measurement. Electric field intensities are measured along the surface of the photonic crystal (shown by the dashed line) by a monopole receiver. Origin of the coordinate system is the middle of the surface. Source is a horn antenna. Incidence direction is represented by the arrow.

We calculated the electric field amplitude distributions for TM polarized waves incident on the metallodielectric PC for various incidence angles. Figure 3.13 shows the steady state electric field amplitudes at 9.7 GHz for incidence angles of 15° and 45° . Incident wave is a Gaussian beam and has a width of 3 wavelengths. Equal frequency contour shown in Fig. 3.12 indicates that at this frequency the metallodielectric photonic crystal may exhibit negative refraction, i.e., incident and transmitted electromagnetic waves shall fall into the same side of the surface normal. Negative refraction effect is clearly observed in Fig. 3.13.

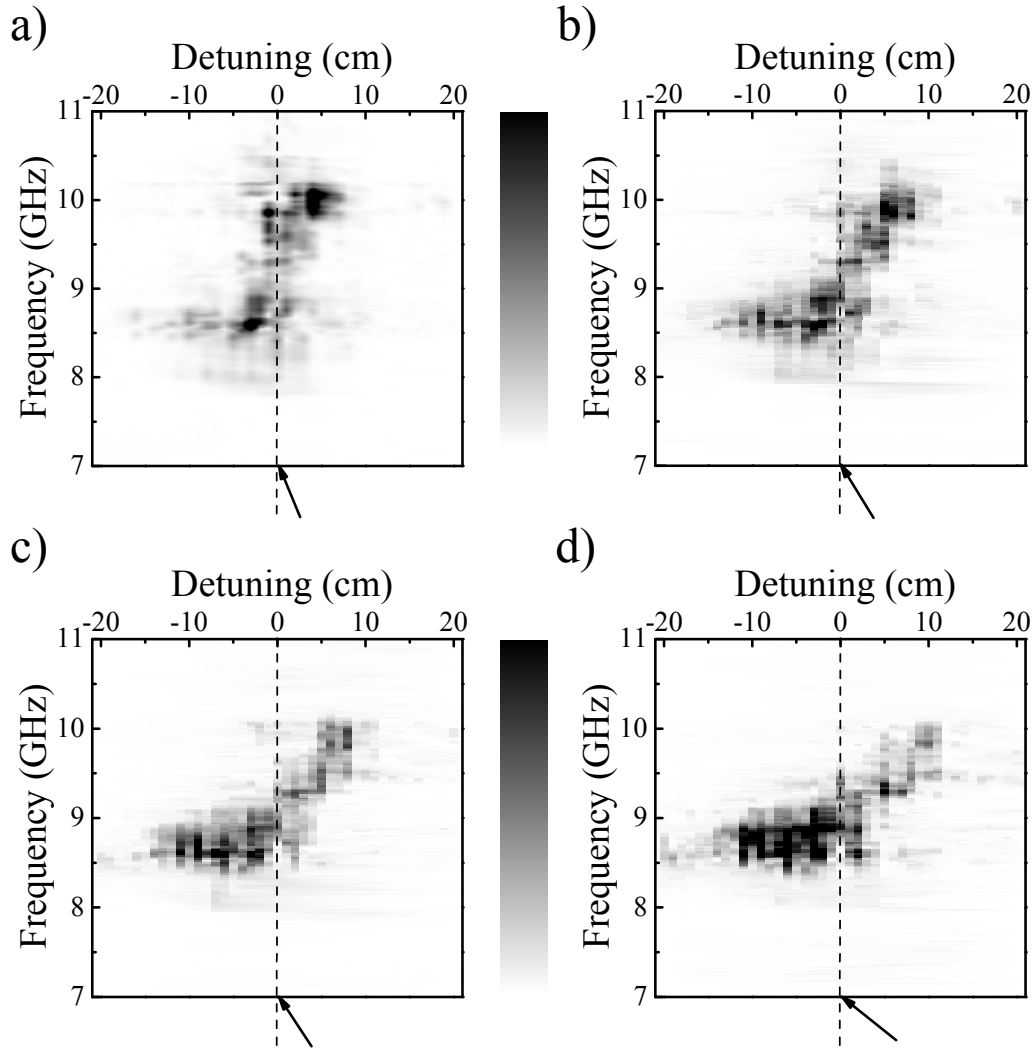


Figure 3.15: Measured electric field intensities along the surface of the photonic crystal are shown for incidence angles of (a) 15° (b) 25° (c) 35° (d) 45° . Incidence direction is shown by the arrow. Black represents the maximum field intensity, whereas white color represents the minimum field intensity.

To demonstrate the negative refraction effect experimentally, one can measure the electric field intensity along the surface of the photonic crystal at the output interface for various incidence angles. A sample measurement setup is shown in Fig. 3.14. In this configuration, transmitting horn antenna is tilted such that EM

waves are incident on the surface of the PC with angle θ . Electric field amplitude is measured along the surface of the PC at the output interface by using a monopole antenna. If the incident EM wave is negatively refracted one detects the output beam on the side indicated by the *negative side* in Fig. 3.14. To be able to use such a measurement scheme certain criteria must be met. First of all, there must be a single refracted beam. The condition for multiple Bragg refracted waves can be written as $|\mathbf{k}_{\text{free}}| \geq |\mathbf{k}_{\text{parallel}} + \mathbf{G}_n|$, where \mathbf{k}_{free} is the free space wave vector, $\mathbf{k}_{\text{parallel}}$ is the surface parallel component of the wave vector, and \mathbf{G}_n is a reciprocal lattice vector [113]. The free space EFS contour shown in Fig. 3.12 is contained in the first Brillouin zone. As a result $|\mathbf{k}_{\text{free}}|$ is smaller than any reciprocal lattice vector, $|\mathbf{G}_n|$. Hence, the condition of single refracted beam is fulfilled for the considered frequency range. The other criteria to be met is that there must not be surface propagating waves in the frequency range of interest. The surface propagating waves may be due to surface corrugation [82, 90] or surface plasmon modes of the metallic rods [114]. There are no corrugations at the surface of the metallodielectric PC that we have used. In addition, surface plasmon modes of the metallic rods occur for the TE (electric field perpendicular to the axes of the rods) polarized waves [113]. As a result there are no surface propagating waves for the structure that we used in this study. Also, our FDTD calculations shown in Fig. 3.13 clearly shows that a single refracted beam propagates inside the photonic crystal and there are no distinguishable surface propagating waves. In conclusion, the experimental scheme depicted in Fig. 3.14 can be used to demonstrate negative refraction for this structure.

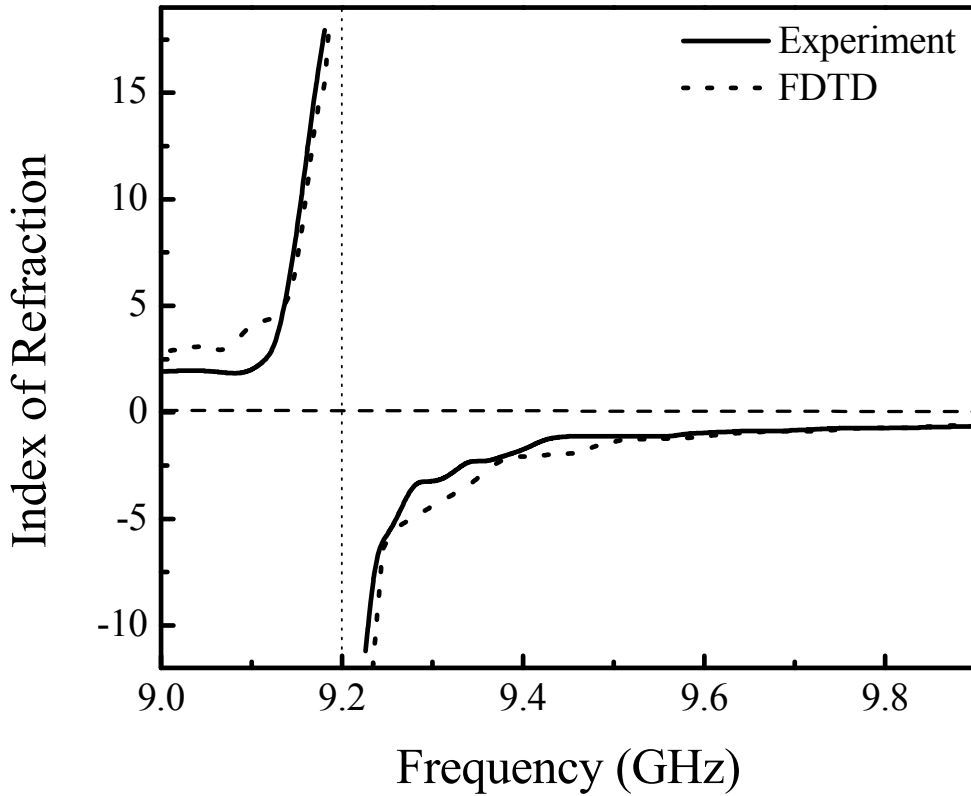


Figure 3.16: Measured and calculated indices of refraction between 9 GHz and 10 GHz at 15° incidence angle. Solid curve represents the experimental data and the dashed curve represents the theoretical indices of refraction obtained from FDTD simulations.

We measured the electric field intensities along the surface of the photonic crystal for various incidence angles to demonstrate the negative refraction experimentally. We used an HP-8510 C vector network analyzer in our measurements. Electromagnetic waves are transmitted by a standard gain horn antenna and measured by a monopole antenna. Incidence direction is indicated by a long arrow and the surface normal is indicated by the dashed line. Waves that are positively refracted are expected to emerge from the positive side of the surface, whereas negatively refracted waves are to emerge from the negative side. Measurement results for incidence angles of 15° , 25° , 35° , and 45° are shown in Figs. 3.15 (a), (b), (c), and (d), respectively. Figure 3.15 shows that between 9.25 GHz and

10.3 GHz waves emerge from the negative side of the PC. Hence, between 9.25 GHz and 10.3 GHz EM waves are negatively refracted by the PC. By using the shift with respect to the center of the PC surface one can calculate the indices of refraction. The sign of the index of refraction is decided by whether the shift is to the positive side or to the negative side. Experimental and theoretical results for the indices of refraction at 25° incidence angle is shown in Fig. 3.16. The indices of refraction are positive between 9 GHz and 9.19 GHz. Around 9.2 GHz there is an abrupt change: just below 9.2 GHz the indices of refraction are positive and just above 9.2 GHz the indices of refraction are negative. Moreover, in the close vicinity of 9.2 GHz the indices of refraction are very high, +18 and -12 . This is due to the flatness of EFS contours around 9.2 GHz (Fig. 3.12). Between 9.25 GHz and 10 GHz indices of refraction are negative. Figure 3.16 shows that indices of refraction are strongly dependent on frequency at fixed incidence angle. In addition, due to the anisotropic EFS contours shown in Fig. 3.12 one expects indices of refraction to be dependent on the incidence angle. Measured indices of refraction at fixed frequency, 9.7 GHz, for incidence angles of 15° , 25° , 35° , and 45° are -0.65 , -0.85 , -0.88 , and -0.96 , respectively. These results clearly show that incidence angle independent indices of refraction can not be defined for the metallodielectric photonic crystal used in this study. This is due to the shape of the EFS contours near the frequencies where one observes negative refraction (Fig. 3.12). To obtain uniform angle independent negative indices of refraction two conditions must be satisfied. First, a circular EFS centered at the origin of the Brillouin zone is required. Second, the radius of circular EFS must be decreasing with increasing frequency.

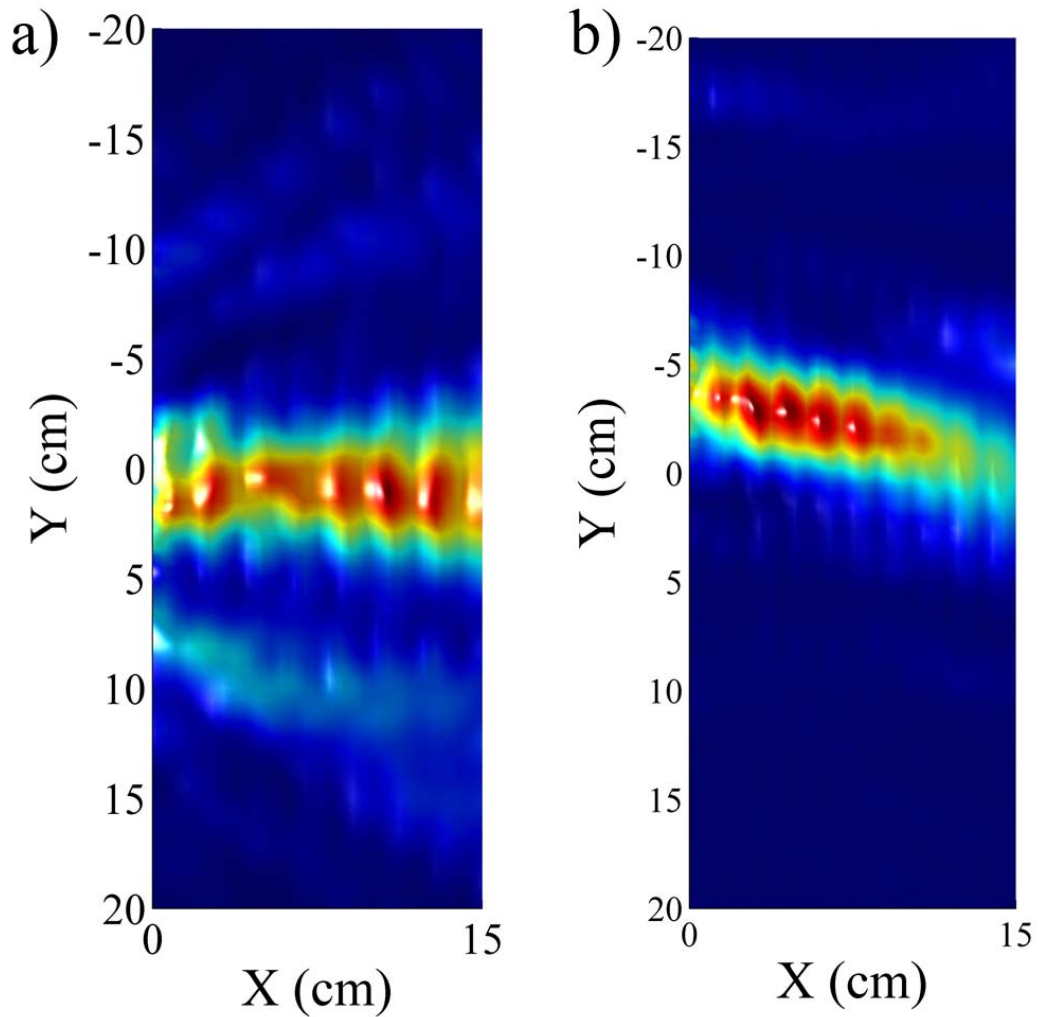


Figure 3.17: a) Electric field intensity for 9 GHz. b) Electric field intensity for 9.7 GHz. Incidence angle is 25 degrees.

We further explored the negative refraction effect by measuring the electric field intensities on the output side of the photonic crystal over an area of $40 \times 15 \text{ cm}^2$ area. The measurements were carried out by using a precision X-Y stage with steps of 2.5 mm. The measurement results for an incidence angle of 25 are shown in Figs. 3.17 (a) and (b). Figure 3.17 (a) shows the electric field intensity for 9 GHz. Note that at 9 GHz the incident electromagnetic waves are positively refracted by the metallodielectric photonic crystal. On the other hand,

Fig. 3.17 (b) shows the electric field intensities for 9.7 GHz. Figure 3.17 (b) clearly demonstrates that the electromagnetic waves are negatively refracted at 9.7 GHz when they are incident by 25 on the metallodielectric photonic crystal.

3.3.3 Focusing of Electromagnetic Waves

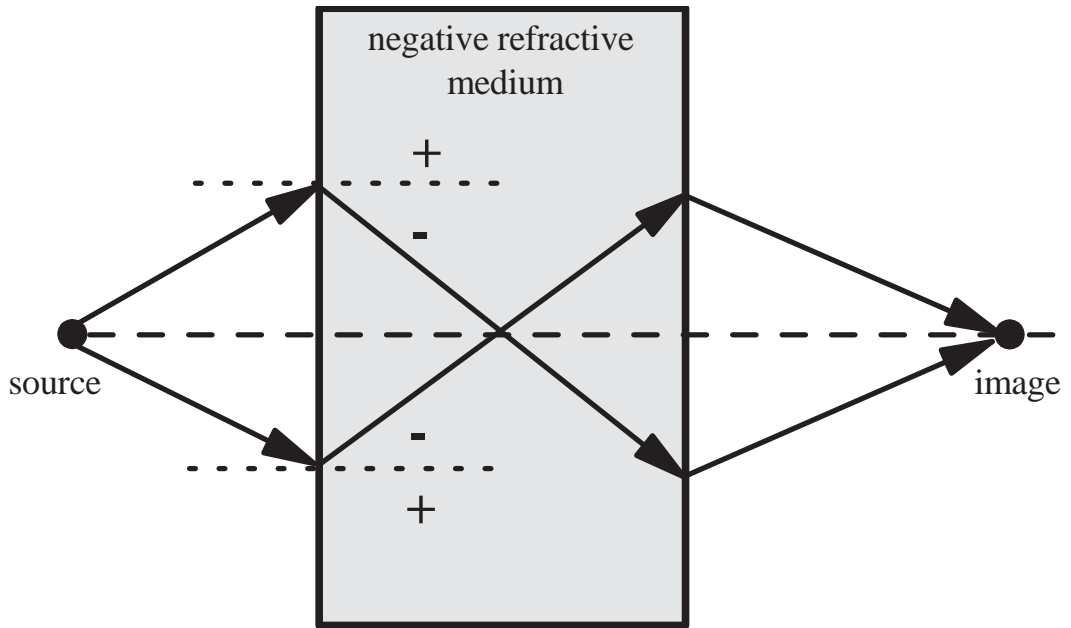


Figure 3.18: A simple illustration of the focusing effect.

Negative refraction effect may be utilized in certain applications. One such application is the focusing of electromagnetic waves [106, 115, 116, 117]. An illustration of this effect by using simple ray optics arguments is given in Fig. 3.18. Two rays emerging from a point source will be refracted to the negative side of the surface-normal as they impinge on the photonic crystal. On the other side of the photonic crystal-air interface, EM waves will be once more refracted towards the negative side of the surface normal. As a result two rays will intersect at a point. At the intersection point an image of the source will be formed. We will call this point as the image point or focus point throughout the rest of the paper.

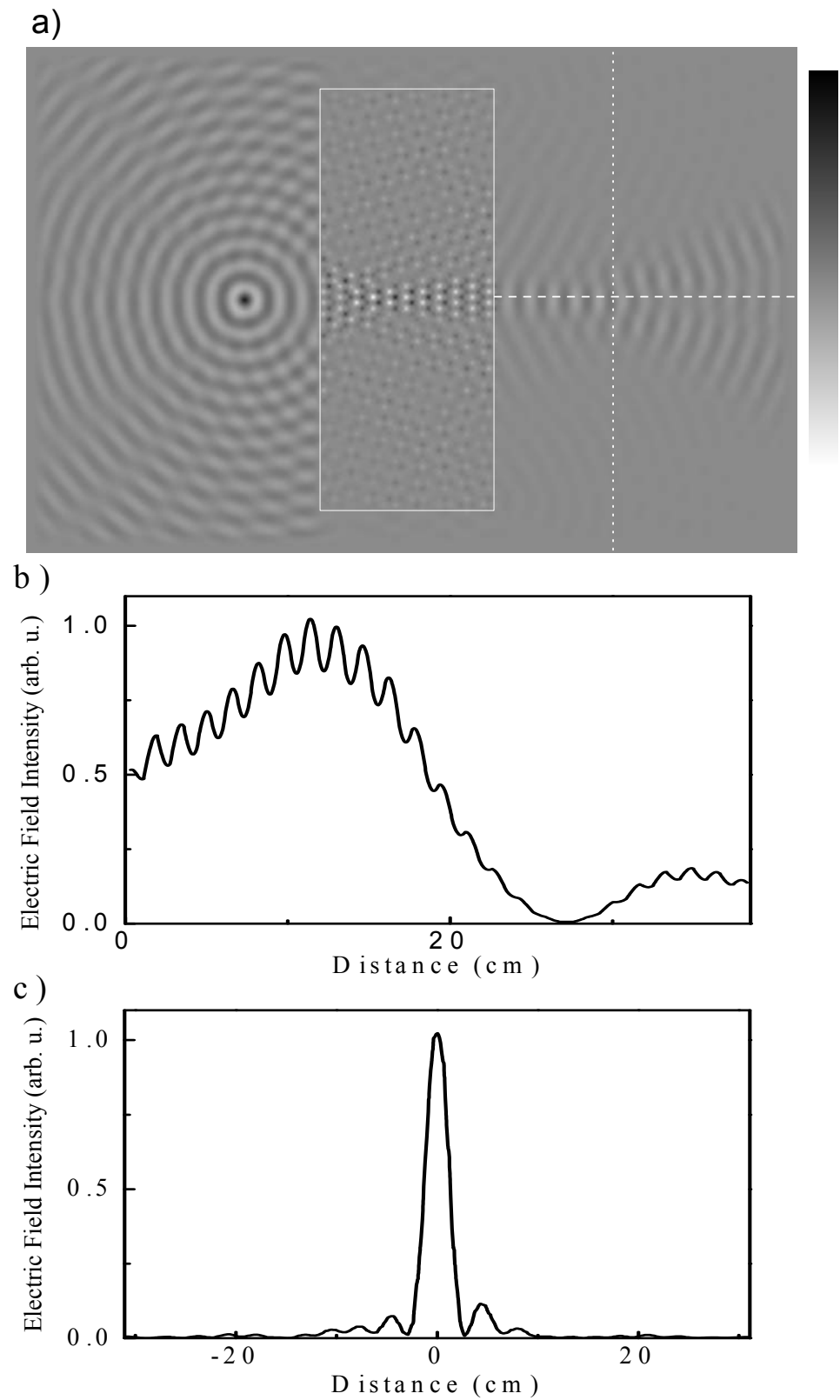


Figure 3.19: a) Electric field distribution from a monopole source placed in front of the metallodielectric PC. Black represents the maximum field amplitude, whereas white color represents the minimum field amplitude. b) Electric field intensity along the dashed-line c) Electric field intensity along the dotted-line

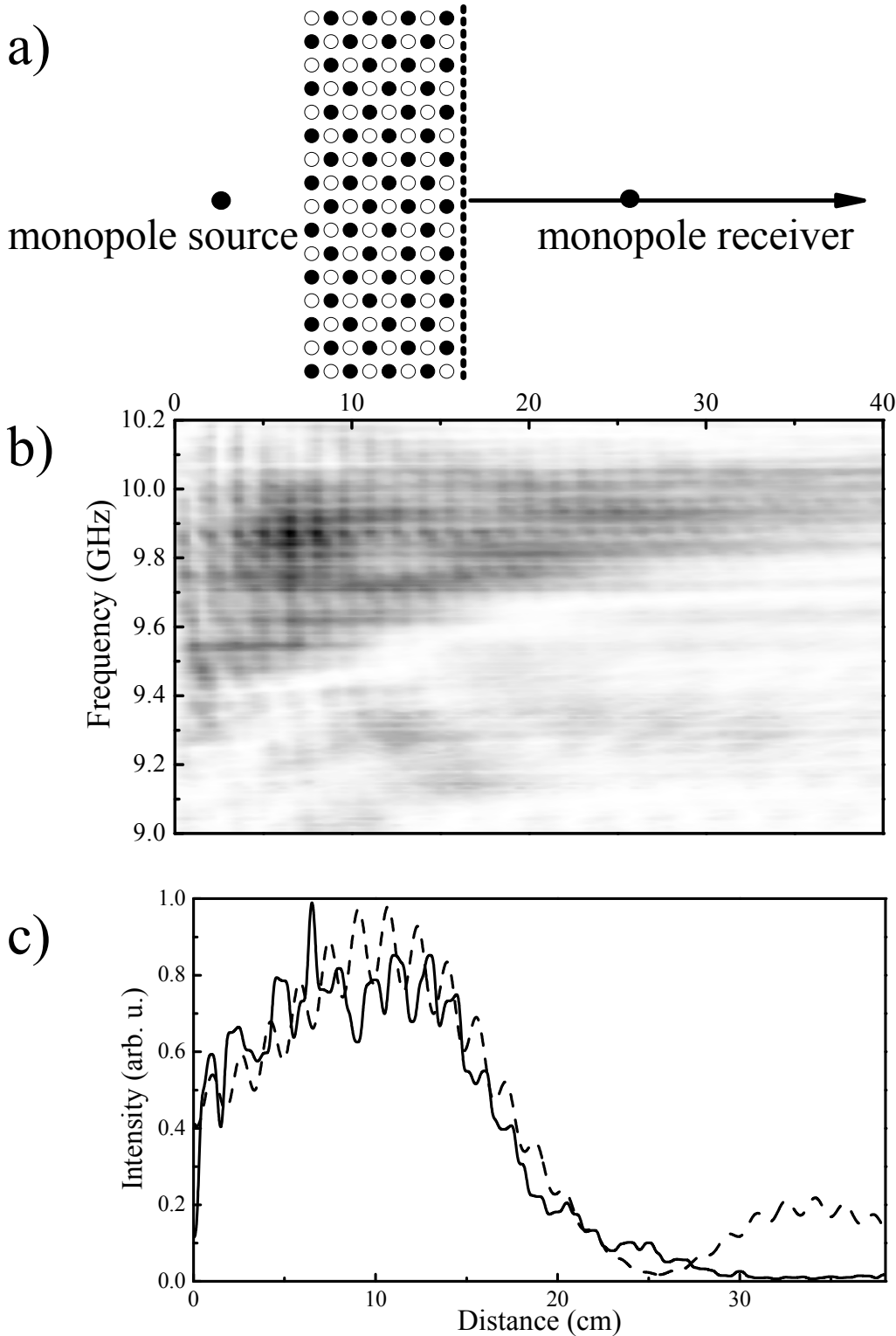


Figure 3.20: (a) Experimental setup for focusing measurement. Both the receiver and the source are monopole antennas. Electric field intensities are measured along the direction shown by the arrow. (b) Electric field intensities for when the source is placed 11 cm away from the photonic crystal. Black represents the maximum field intensity, whereas white color represents the minimum field intensity. (c) Measured and calculated electric field intensities at 9.7 GHz

Focusing of EM waves emitted from a monopole source is theoretically demonstrated in Fig. 3.19. A monopole source is placed in front of the metallodielectric PC. The monopole source is 11 cm away from the surface of the PC. Electric field amplitude distribution is calculated by using FDTD method at 9.7 GHz. It was shown in Fig. 3.15 that EM waves with a frequency of 9.7 GHz are negatively refracted by the metallodielectric PC. Since at this frequency EM waves are negatively refracted, one expects to observe the focusing of EM waves emitted from a source at 9.7 GHz. Figure 3.19 shows that EM waves emitted from the monopole source are focused both inside the PC and outside the PC. This is consistent with the simple ray optics scheme shown in Fig. 3.18. Electric field intensity along the dashed-line (Fig. 3.19 (a)) is shown in Fig. 3.19 (b). Figure 3.19 (b) indicates that the image formed outside the PC is located at a distance 13 cm away from the metallodielectric PC. The electric field intensity along the dotted-line (Fig. 3.19 (a)) is shown in Fig. 3.19 (c). Figure 3.19 (b) and (c) show that an image of the monopole source is formed at a distance of 13 cm away from the surface of the PC. The half-power beam width is 2.6 cm. This may be compared to the wavelength at 9.7 GHz, 3.09 cm.

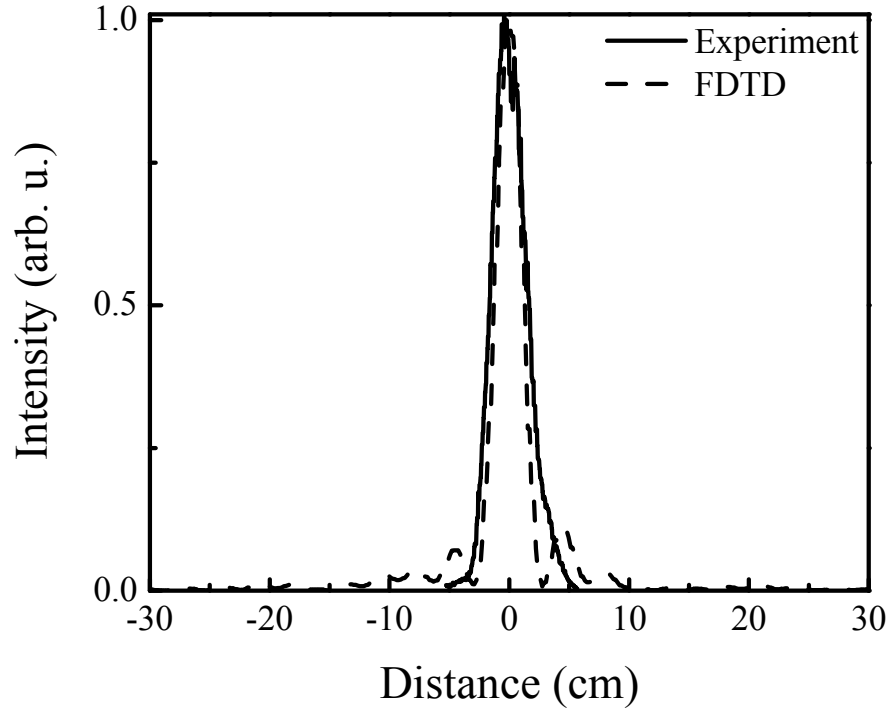


Figure 3.21: (a) Electric field intensities measured at a distance of 13 cm away from the surface of the photonic crystal. Measurement direction is along the surface of the photonic crystal. Measurement is performed at 9.7 GHz.

We measured the electric field intensity along the normal vector of the surface to demonstrate the focusing effect experimentally. Experimental setup is shown in Fig. 3.20 (a). A monopole source is placed in front of the photonic crystal and the electric field intensity is measured on the other side of the photonic crystal along the direction indicated by the arrow. Measurement results for a source distance 11 cm away from the surface of the photonic crystal are shown in Fig. 3.20 (b). Figure 3.20 (c) shows the calculated and measured intensity profile at 9.7 GHz. Note that the measurement and simulation results are in quite good agreement. Figure 3.20 (c) shows that although an image of the source is formed on the other side of the PC, the extent of the image is not sharp along the direction of surface normal when compared to the wavelength. This is mainly due to two reasons. First, the index of refraction is an anisotropic

function of incidence angle. Second, the index of refraction is different from -1 . To observe a correct image of the source an index of refraction equal to -1 at all incidence angles is required [118]. To further investigate the focusing effect we also measured electric field intensities parallel to the surface of the photonic crystal around the image point. Experimental setup is similar to that of Fig. 3.20 (a), except that the intensities are measured parallel to the surface of the PC near the image point. Such a measurement provides information about the extent of the focusing. Measurement and calculation results at 9.7 GHz when the source is placed 11 cm away from the PC surface is shown in Fig. 3.21. For this case the image point is at 13 cm away from the surface of the photonic crystal. Figure 3.21 shows that the electric field intensities are confined to a narrow region at 9.7 GHz. To be explicit, the measured half-width of the intensity profile at this frequency is 2.78 cm, which can be compared to the wavelength $\lambda = 3.09$ cm at this frequency. Note that the image formed is not a "stigmatic image" or "sharp image" as defined in optics [37]. The image of the point source is deformed due to the anisotropic negative indices of refraction. The deformation is also due to the indices of refraction being different than -1 . As a result, the metallodielectric PC introduces spatial aberration to the image. This effect can be compared to the caustics effects [119, 120]. Our results clearly shows that one requires isotropic $n = -1$ indices of refraction for better imaging.

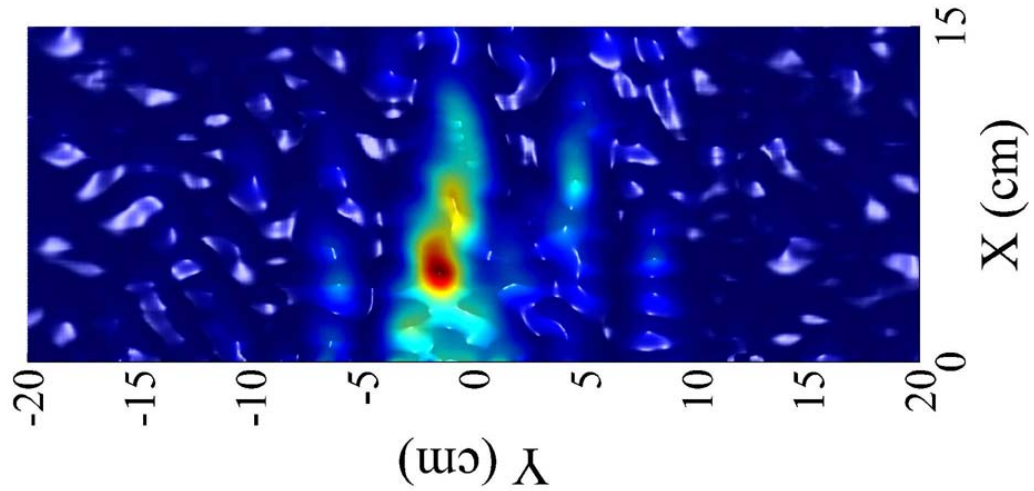


Figure 3.22: Measured electric field intensity at the output side of the metallodielectric photonic crystal. The source monopole was placed on the other side of the photonic crystal. The distance of the source monopole antenna to the input surface of the metallodielectric photonic crystal was 11 cm.

We further analyzed the focusing effect by measuring the electric field over a large area on the output side. The measurements were performed over an area of 40×15 cm² with steps of 1 mm. Note that in the previous section it was that EM waves with a frequency of 9.7 GHz are negatively refracted by the metallodielectric PC. Since at this frequency EM waves are negatively refracted, one expects to observe the focusing of EM waves emitted from a source at 9.7 GHz. The measured field intensities for 9.7 GHz are shown in Fig. 3.22. First of all, Figure 3.22 shows that the electromagnetic fields emitted in all directions by the source monopole antenna are focused by the metallodielectric photonic crystal. Moreover, the image formed by the focusing effect is quite sharp. Also, note that, the image is elongated along x-axis.

Chapter 4

Related Work

4.1 Content-Based Retrieval Systems

4.2 Visual Query Languages and Interfaces

4.3 Presenting Results and Design Guidelines

Chapter 5

Conclusions and Future Work

I would like to conclude my thesis by including several new ideas on metamaterials and photonic crystals. One of these ideas is related to the control of emission of radiation by use of metamaterials. One basic property of the building blocks of metamaterials make them quite interesting for the study of source-material interactions. This property is related to the resonant nature of these building blocks. For instance, the split-ring resonator structure exhibits a quite strong magnetic resonance. Without going much in to detail, we calculated the relative spontaneous emission rate of a point dipole when it is placed near a left-handed structure. The results are plotted in Fig. 5.1. Notice that there is a well pronounced peak. The spontaneous emission rate of the point dipole is enhanced 100 times with respect to free space emission rate at this peak. In addition, we calculated the S11 response of a finite size dipole when it is placed in free space and in front of a left-handed structure, Fig. 5.2. S11, back reflection, may in this case be interpreted as the coupling efficiency to the electromagnetic modes. Figure 5.2 shows a huge enhancement around 4.8 GHz when the dipole is placed in close vicinity of a left-handed structure. Almost 93% of the pumped power is coupled out by use of metamaterial, whereas only 4% is coupled out without metamaterial. This huge enhancement effect may find applications for THz quantum cascade lasers and microwave antennas.

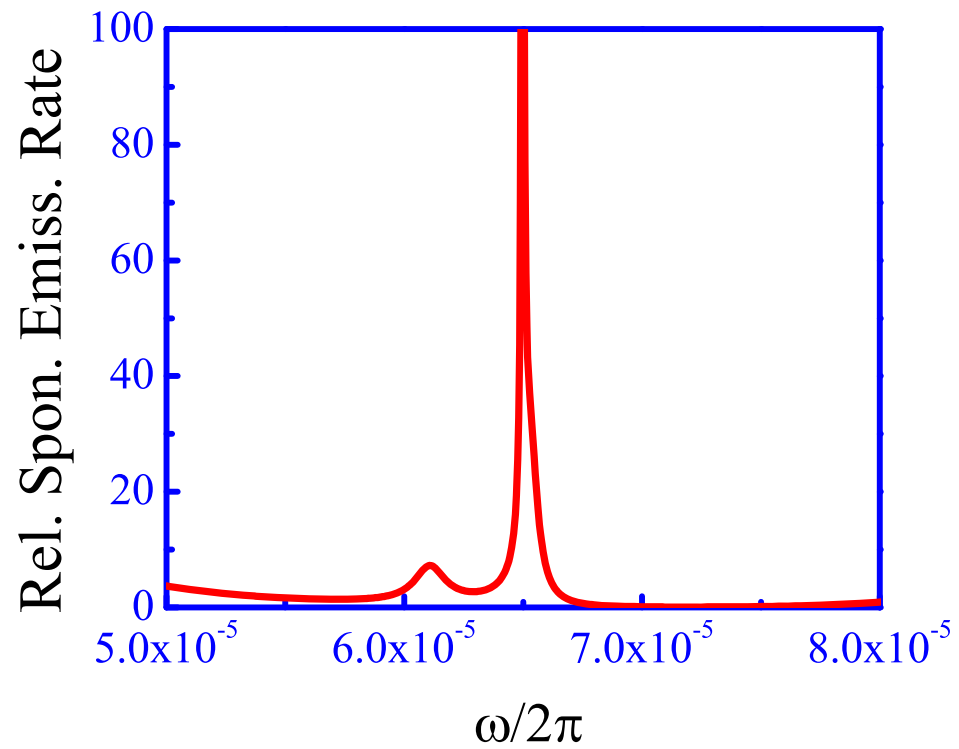


Figure 5.1: Relative spontaneous emission rate of a point dipole when it is placed in front of a left-handed structure. The term "relative" refers to the spontaneous emission rate in free space.

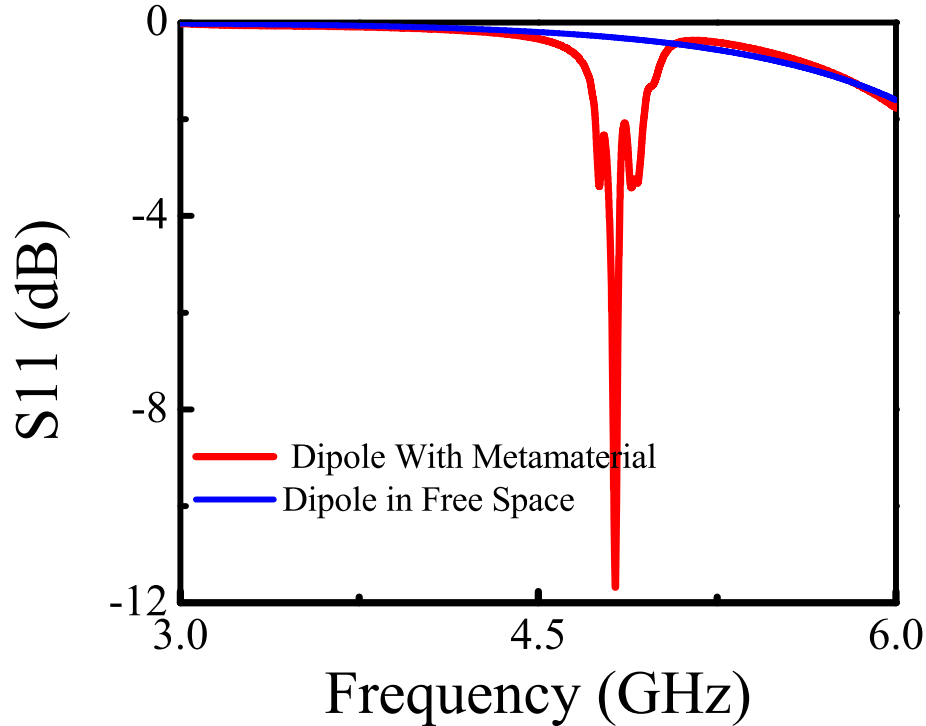


Figure 5.2: S_{11} response of a finite size dipole when it is placed in free space and when it is placed in closed vicinity to a left-handed material.

Another application that I propose is the ultra-small high quality cavities based on metamaterials. While the properties of a metamaterial can be described by effective parameters, permittivity and permeability, there is another way to look at the problem. The metamaterial medium still consists of periodic arrangement of sub-wavelength features. As a result, we can describe metamaterials also by Bloch modes, just as photonic crystals (see chapter 3). An important implication of such a definition is the possibility of cavity modes when a suitable local perturbation is introduced to the periodic potential. Such cavity modes are observed as well-pronounced transmission peaks inside the forbidden frequency region of transmission response of the structure without the perturbation. We plotted the calculated transmission through negative permeability medium when

a local perturbation is added in Fig. 5.3 (a). There is a transmission peak inside the forbidden frequency range. We associate this peak with the existence of a cavity mode. As a matter of fact our eigenmode calculations proved that there is a cavity mode at this frequency with a quality factor around ≈ 20000 . The size of the local perturbation is around $\lambda/20$. In addition, we calculated the transmission spectrum through a negative permittivity and permeability medium, Fig. 5.3. There are two transmission peaks. Both of these transmission peaks are associated with cavity modes.

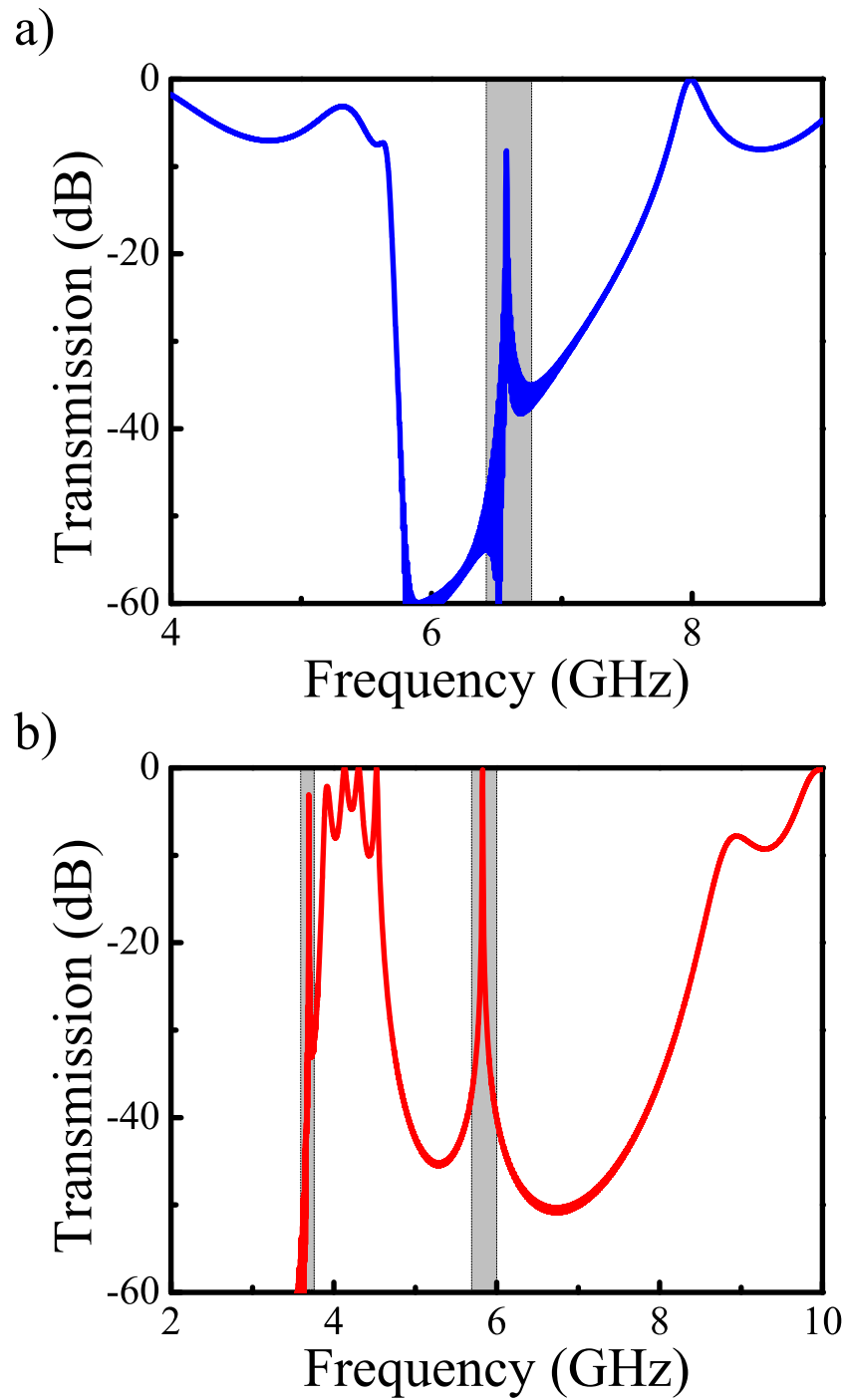


Figure 5.3: a) Transmission through negative permeability medium when a local perturbation is introduced to the structure. b) Transmission through negative permeability and negative permittivity medium when a local perturbation is introduced to the structure.

One final application is related to the beaming of electromagnetic waves by surface modes of a photonic crystal. In section 3.2.3, we showed that surface modes can be utilized for beaming applications. But the beam profile were aligned along a particular direction. One wonders wether this direction can be controlled. We believe that such a control can be achieved to some degree by playing with the surface morphology of the photonic crystal. We plotted the electric field distribution of electromagnetic waves when the surface morphology is significantly altered in Fig. 5.4. Note that the direction of the beam is tilted.

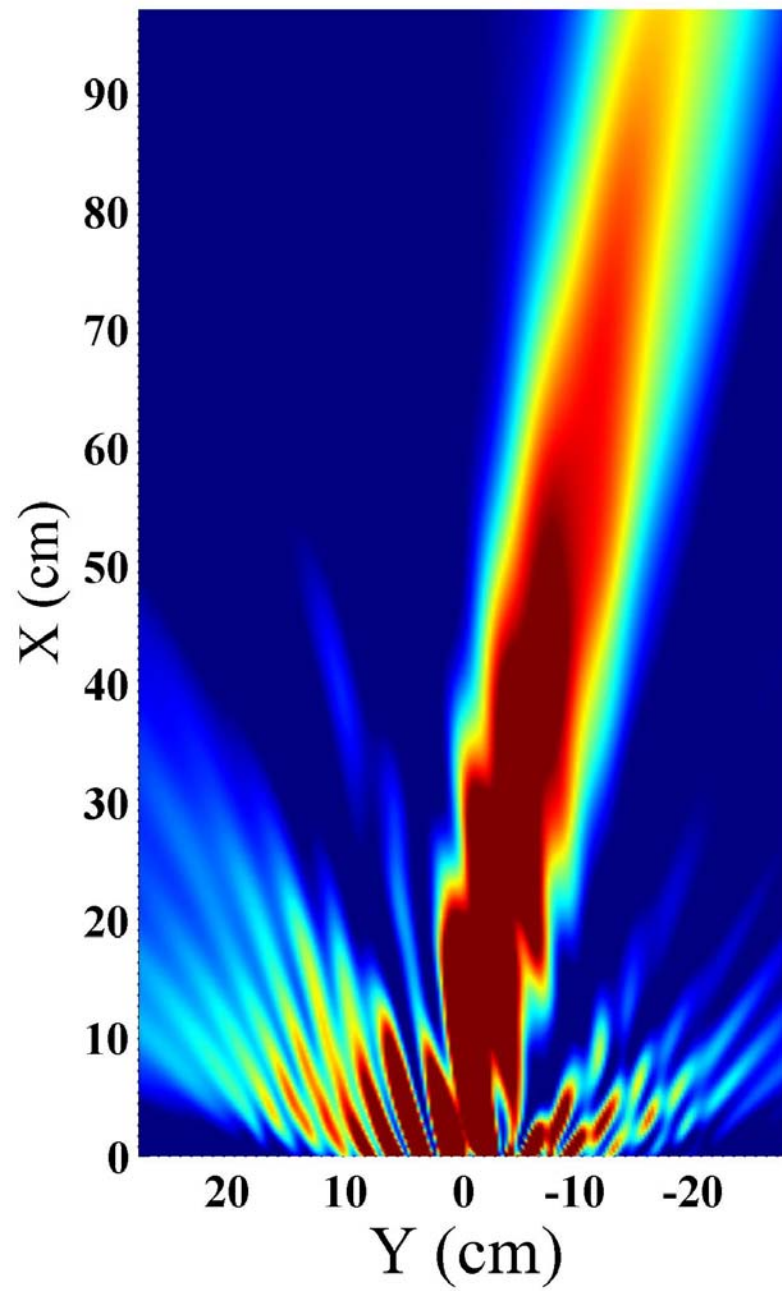


Figure 5.4: Off-axis beaming of electromagnetic waves by utilizing surface modes.

Bibliography

- [1] Ltd Samsung Electronics Co. Us patent 7064886: Light regulating device and photonic crystal display utilizing photonic bandgap controls, 2006.
- [2] Axel Scherer and Marko Loncar. Us patent 7079240: Photonic crystal laser sources for chemical detection, 2006.
- [3] Philip St. John Russell, Timothy Adam Birks, and Jonathan Cave Knight. Us patent 6631234: Photonic crystal fibers, 2003.
- [4] Jan Lipson, Hongyu Deng, and Thomas Lenosky. Us patent 6810056: Single mode vertical cavity surface emitting laser using photonic crystals with a central defect, 2004.
- [5] Inc BioTell. Us patent 6728429: Optical detection, 2004.
- [6] Randall W. Nelson, Jennifer R. Krone, Russell Granzow, Osten Jansson, and Stefan Sjolander. Us patent 5955729: Surface plasmon resonance-mass spectrometry, 1999.
- [7] Mitsuhiro Sakaguchi, Tineke Thio, Richard A. Linke, Thomas W. Ebbesen, and Henri J. Lezec. Us patent 6834027: Surface plasmon-enhanced read/write heads for optical data storage media, 2004.
- [8] D. R. Smith, Willie J. Padilla, D. C. Vier, S. C. Nemat-Nasser, and S. Schultz. Composite medium with simultaneously negative permeability and permittivity. *Phys. Rev. Lett.*, 84:4184, 2000.

- [9] Daniel D. Stancil, Benjamin E. Henty, Ahmet G. Cepni, and J. P. Van't Hof. Observation of an inverse doppler shift from left-handed dipolar spin waves. *Physical Review B (Condensed Matter and Materials Physics)*, 74(6):060404, Aug. 2006.
- [10] J. B. Pendry. Negative refraction makes a perfect lens. *Phys. Rev. Lett.*, 85:3966, 2000.
- [11] Lucent Technologies Inc. Us patent 6661392: Resonant antennas, 2003.
- [12] Lucent Technologies Inc. Us patent 6958729: Phased array metamaterial antenna system, 2005.
- [13] Hou-Tong Chen, Willie J. Padilla, Joshua M. O. Zide, Arthur C. Gossard, Antoinette J. Taylor, and Richard D. Averitt. Active terahertz metamaterial devices. *Nature*, 444:597, 2006.
- [14] V. G. Veselago. The electrodynamics of substances with simultaneously negative values of permittivity and permeability. *Sov. Phys. Usp.*, 10:509, 1968.
- [15] D. F. Sievenpiper, M. E. Sickmiller, and E. Yablonovitch. 3d wire mesh photonic crystals. *Phys. Rev. Lett.*, 76:2480, 1996.
- [16] J. B. Pendry, A. J. Holden, W. J. Stewart, and I. Youngs. Extremely low frequency plasmons in metallic mesostructures. *Phys. Rev. Lett.*, 76:4773, 1996.
- [17] S. I. Maslovski, S.A. Tretyakov, and P.A. Belov. Wire media with negative effective permittivity: A quasi-static model. *Microwave Opt. Technol. Lett.*, 35:47, 2002.
- [18] J. B. Pendry, A. J. Holden, D. J. Robins, and W. J. Stewart. Magnetism from conductors and enhanced nonlinear phenomena. *IEEE Trans. Microwave Theory Technol.*, 47:2075, 1999.
- [19] J. B. Pendry, A. J. Holden, D. J. Robbins, and W. J. Stewart. Low frequency plasmons in thin-wire structures. *J. Phys.: Condens. Matter*, 10:4785, 1998.

- [20] S. I. Maslovski, S. A. Tretyakov, and P. A. Belov. Wire media with negative effective permittivity: A quasi-static model. *Microwave Opt. Technol. Lett.*, 35:47, 2002.
- [21] IEEE. *Research on the macro effect of the thin wire array in metamaterial by equivalent circuit method*, IEEE AP-S International Symposium And USNC/URSI National Radio Science Meeting, Washington D.C., USA, 2005.
- [22] P. Markos and C. M. Soukoulis. Transmission studies of left-handed materials. *Phys. Rev. B*, 65:033401, 2001.
- [23] Mehmet Bayindir, K. Aydin, E. Ozbay, P. Marko, and C. M. Soukoulis. Transmission properties of composite metamaterials in free space. *Appl. Phys. Lett.*, 81:120, 2002.
- [24] Philippe Gay-Balmaz and Olivier J. F. Martin. Electromagnetic resonances in individual and coupled split-ring resonators. *J. Appl. Phys.*, 92:2929, 2002.
- [25] R. Marques, J. Martel, F. Mesa, and F. Medina. Left-handed-media simulation and transmission of em waves in subwavelength split-ring-resonator-loaded metallic waveguides. *Phys. Rev. Lett.*, 89:183901, 2002.
- [26] C. R. Simovski and B. Sauviac. Role of wave interaction of wires and split-ring resonators for the losses in a left-handed composite. *Phys. Rev. E*, 70:046607, 2004.
- [27] A. B. Movchan and S. Guenneau. Split-ring resonators and localized modes. *Phys. Rev. B*, 70:125116, 2004.
- [28] Yi-Jang Hsu and Yen-Chun Huang, Jiann-Shing Lih, and Jyh-Long Chern. Electromagnetic resonance in deformed split ring resonators of left-handed meta-materials. *J. Appl. Phys.*, 96:1979, 2004.
- [29] M. Shamonin, E. Shamonina, V. Kalinin, and L. Solymar. Properties of a metamaterial element: Analytical solutions and numerical simulations for a singly split double ring. *J. Appl. Phys.*, 95:3778, 2004.

- [30] Yen-Chun Huang, Yi-Jang Hsu, Jiann-Shing Lih, and Jyh-Long Chern. Transmission characteristics of deformed split-ring resonators. *Jpn. J. Appl. Phys., Part 2*, 43:L190, 2004.
- [31] B. Sauviac, C.R. Simovski, and S.A. Tretyakov. Double split-ring resonators: Analytical modeling and numerical simulations. *Electromagnetics*, 24:317, 2004.
- [32] Philippe Gay-Balmaz and Olivier J. F. Martin. Efficient isotropic magnetic resonators. *Appl. Phys. Lett.*, 81:939, 2002.
- [33] R. Marques, F. Medina, and R. Rafi-El-Idrissi. Role of bianisotropy in negative permeability and left-handed metamaterials. *Phys. Rev. B*, 65:144440, 2002.
- [34] R. Marques, F. Mesa, J. Martel, and F. Medina. Comparative analysis of edge- and broadside- coupled split ring resonators for metamaterial design - theory and experiments. *IEEE Trans. Antennas Propag.*, 51:2572, 2003.
- [35] D. R. Smith, J. Gollub, J. J. Mock, W. J. Padilla, and D. Schuring. Calculation and measurement of bianisotropy in a split ring resonator metamaterial. *J. Appl. Phys.*, 100:024507, 2006.
- [36] Yu. O. Averkov and V. M. Yakovenko. Cherenkov radiation by an electron bunch that moves in a vacuum above a left-handed material. *Phys. Rev. B*, 72:205110, 2005.
- [37] Max Born and Emil Wolf. *Principles of Optics: Electromagnetic Theory of Propagation, Interference and Diffraction of Light*. Cambridge University Press, The Edinburgh Building, Cambridge CB2 2RU, UK, 7. edition edition, 1999.
- [38] Richard W. Ziolkowski and Allison D. Kipple. Application of double negative materials to increase the power radiated by electrically small antennas. *IEEE TRANSACTIONS ON ANTENNAS AND PROPAGATION*, 51:2626, 2003.

- [39] M. C. K. Wiltshire, J. B. Pendry, I. R. Young, D. J. Larkman, D. J. Gilderdale, and J. V. Hajnal. Microstructured magnetic materials for rf flux guides in magnetic resonance imaging. *Science*, 291:849, 2001.
- [40] D. R. Smith, S. Schultz, P. Markos, and C. M. Soukoulis. Determination of effective permittivity and permeability of metamaterials from reflection and transmission coefficients. *Phys. Rev. B*, 65:195104, 2002.
- [41] T. Koschny, M. Kafesaki, E. N. Economou, and C. M. Soukoulis. Effective medium theory of left-handed materials. *Phys. Rev. Lett.*, 93:107402, 2004.
- [42] T. Koschny, P. Markos, D. R. Smith, and C. M. Soukoulis. Resonant and antiresonant frequency dependence of the effective parameters of metamaterials. *Phys. Rev. E*, 68:065602, 2003.
- [43] Th. Koschny, P. Markos, E. N. Economou, D. R. Smith, D. C. Vier, and C. M. Soukoulis. Impact of inherent periodic structure on effective medium description of left-handed and related metamaterials. *Phys. Rev. B*, 71:245105, 2005.
- [44] D. R. Smith, D. C. Vier, N. Kroll, and S. Schultz. Direct calculation of permeability and permittivity for a left-handed metamaterial. *Appl. Phys. Lett.*, 77:2246, 2000.
- [45] Xudong Chen, Tomasz M. Grzegorzcyk, Bae-Ian Wu, Jr. Joe Pacheco, and Jin Au Kong. Robust method to retrieve the constitutive effective parameters of metamaterials. *Phys. Rev. E*, 70:016608, 2004.
- [46] Xudong Chen, Bae-Ian Wu, Jin Au Kong, and Tomasz M. Grzegorzcyk. Retrieval of the effective constitutive parameters of bianisotropic metamaterials. *Phys. Rev. E*, 71:046610, 2005.
- [47] Andrew A. Houck, Jeffrey B. Brock, and Isaac L. Chuang. Experimental observations of a left-handed material that obeys snell's law. *Phys. Rev. Lett.*, 90:137401, 2003.

- [48] Z. G. Dong, S. N. Zhu, H. Liu, J. Zhu, and W. Cao. Numerical simulations of negative-index refraction in wedge-shaped metamaterials. *Phys. Rev. E*, 72:016607, 2005.
- [49] R. A. Shelby, D. R. Smith, and S. Schultz. Experimental verification of a negative index of refraction. *Science*, 292:77, 2001.
- [50] L. Ran, J. Huangfu, H. Chen, X. Zhang, K. Chen, T. M. Grzegorzczak, and J. A. Kong. Beam shifting experiment for the characterization of left-handed properties. *J. Appl. Phys.*, 95:2238, 2004.
- [51] A. A. Houck, J. B. Brock, and I. L. Chuang. Experimental observations of a left-handed material that obeys snell's law. *Phys. Rev. Lett.*, 90:137401, 2003.
- [52] C. G. Parazzoli, R. B. Greegor, K. Li, B. E. C. Koltenbah, and M. Tanielian. Experimental verification and simulation of negative index of refraction using snell's law. *Phys. Rev. Lett.*, 90:107401, 2003.
- [53] K. Aydin, K. Guven, C. M. Soukoulis, and E. Ozbay. Observation of negative refraction and negative phase velocity in left-handed metamaterials. *Appl. Phys. Lett.*, 86:124102, 2005.
- [54] K. Guven, K. Aydin, K. B. Alici, C. M. Soukoulis, and E. Ozbay. Spectral negative refraction and focusing analysis of a two-dimensional left-handed photonic crystal lens. *Phys. Rev. B*, 70:205125, 2004.
- [55] N. Katsarakis, T. Koschny, M. Kafesaki, E. N. Economou, and C. M. Soukoulis. Electric coupling to the magnetic resonance of split-ring resonators. *Appl. Phys. Lett.*, 84:2943, 2004.
- [56] K. Aydin, K. Guven, M. Kafesaki, L. Zhang, C. M. Soukoulis, and E. Ozbay. Experimental observation of true left-handed transmission peaks in metamaterials. *Opt. Lett.*, 29:2623, 2004.
- [57] M. Nieto-Vesperinas. Problem of image superresolution with a negative-refractive-index slab. *J. Opt. Soc. Am. A*, 21:491, 2004.

- [58] CST GmbH, Darmstadt, Germany. *User Manual Version 5.0*, 2005.
- [59] A. Grbic and G. V. Eleftheriades. Growing evanescent waves in negative-refractive-index transmission-line media. *Appl. Phys. Lett.*, 82:1815, 2003.
- [60] Irfan Bulu, Humeyra Caglayan, and Ekmel Ozbay. Experimental demonstration of subwavelength focusing of electromagnetic waves by labyrinth-based two-dimensional metamaterials. *Opt. Lett.*, 31:814, 2006.
- [61] Richard W. Ziolkowski. Propagation in and scattering from a matched metamaterial having a zero index of refraction. *Phys. Rev. E*, 70:046608, 2004.
- [62] Alexander A. Zharov, Ilya V. Shadrivov, , and Yuri S. Kivshar. Nonlinear properties of left-handed metamaterials. *Phys. Rev. Lett.*, 91:037401, 2003.
- [63] J. A. Porto, L. Martin-Moreno, and F. J. Garcia-Vidal. Optical bistability in subwavelength slit apertures containing nonlinear media. *Phys. Rev. B*, 70:081402, 2004.
- [64] A. Kafaratzis and Z. Hu. *IEEE High Frequency Postgraduate Student Colloquium*, page 77, 2005.
- [65] Jing-Ping Xu, Nian-Hua Liu, and Shi-Yao Zhu. Spontaneous emission field of a two-level atom embedded in one-dimensional left-handed- and right-handed-material photonic crystals. *Phys. Rev. E*, 73:016604, 2006.
- [66] Stefan Enoch, Grard Tayeb, Pierre Sabouroux, Nicolas Gurin, and Patrick Vincent. A metamaterial for directive emission. *Phys. Rev. Lett.*, 89:213902, 2002.
- [67] K. Li, S. J. McLean, R. B. Greegor, C. G. Parazzoli, and M. H. Tanielian. Free-space focused-beam characterization of left-handed materials. *Appl. Phys. Lett.*, 82:2535, 2003.
- [68] N. Katsarakis, T. Koschny, M. Kafesaki, E. Economou, and C. M. Soukoulis. Electric coupling to the magnetic resonance of split ring resonators. *Appl. Phys. Lett.*, 84:2943, 2004.

- [69] T. J. Yen, W. J. Padilla, N. Fang, D. C. Vier, D. R. Smith, J. B. Pendry, D. N. Basov, and X. Zhang. Terahertz magnetic response from artificial materials. *Science*, 303:1494, 2004.
- [70] C. A. Balanis. *Antenna Theory: Analysis and Design*. Wiley, New York, 1997.
- [71] I. Bulu, H. Caglayan, and E. Ozbay. Highly directive radiation from sources embedded inside photonic crystals. *Appl. Phys. Lett.*, 83:3263, 2003.
- [72] D. Chigrin. Radiation pattern of a classical dipole in a photonic crystal: Photon focusing. *Phys. Rev. E*, 70:056611, 2004.
- [73] G. Poilasne, J. Lenormand, P. Pouliguen, K. Mahdjoubi, C. Terret, and P. Gelin. Theoretical study of interactions between antennas and metallic photonic bandgap materials. *Microwave Opt. Technol. Lett.*, 15:384, 1997.
- [74] G. Poilasne, P. Pouliguen, K. Mahdjoubi, C. Terret, P. Gelin, and L. Desclos. Experimental radiation pattern of dipole inside metallic photonic bandgap material. *Microwave Opt. Technol. Lett.*, 22:10, 1999.
- [75] M. Qiu and S. He. High-directivity patch antenna with both photonic bandgap substrate and photonic bandgap cover. *Microwave Opt. Technol. Lett.*, 30:41, 2001.
- [76] C. R. Simovski and S. He. Antennas based on modified metallic photonic bandgap structures consisting of capacitively loaded wires. *Microwave Opt. Technol. Lett.*, 31:214, 2001.
- [77] K. M. Ho, C. T. Chan, and C. M. Soukoulis. Existence of a photonic gap in periodic dielectric structures. *Phys. Rev. Lett.*, 65:3152, 1990.
- [78] E. Yablonovitch. Inhibited spontaneous emission in solid-state physics and electronics. *Phys. Rev. Lett.*, 58:2059, 1987.
- [79] A. Yariv, Y. Xu, R. K. Lee, and A. Scherer. Coupled-resonator optical-waveguide:a proposal and analysis. *Opt. Lett.*, 24:711, 1999.

- [80] N. Stefanou and A. Modinos. Impurity bands in photonic insulators. *Phys. Rev. B*, 57:12127, 1998.
- [81] Yong-Jae Lee, Se-Heon Kim, Joon Huh, Guk-Hyun Kim, Yong-Hee Lee, Sang-Hwan Cho, Yoon-Chang Kim, and Young Rag Do. A high-extraction-efficiency nanopatterned organic light-emitting diode. *Applied Physics Letters*, 82(21):3779–3781, 2003.
- [82] Robert D. Meade, Karl D. Brommer, Andrew M. Rappe, and J. D. Joannopoulos. Electromagnetic bloch waves at the surface of a photonic crystal. *Phys. Rev. B* 44, 44:10961, 1991.
- [83] D. Beaglehole. Coherent and incoherent radiation from optically excited surface plasmons on a metal grating. *Phys. Rev. Lett.*, 22:498, 1967.
- [84] L. Martn-Moreno, F. J. Garca-Vidal, H. J. Lezec, K. M. Pellerin, T. Thio, J. B. Pendry, and T. W. Ebbesen. Theory of extraordinary optical transmission through subwavelength hole arrays. *Phys. Rev. Lett.*, 86:1114, 2001.
- [85] Humeyra Caglayan, Irfan Bulu, and Ekmel Ozbay. Extraordinary grating-coupled microwave transmission through a subwavelength annular aperture. *Opt. Express*, 13:1666, 2005.
- [86] L. Martin-Moreno, F. J. Garcia-Vidal, H. J. Lezec, A. Degiron, and T.W. Ebbesen. Theory of highly directional emission from a single subwavelength aperture surrounded by surface corrugations. *Phys. Rev. Lett.*, 90:167401–1, 2003.
- [87] Liang-Bin Yu, Ding-Zheng Lin, Yi-Chun Chen, You-Chia Chang, Kuo-Tung Huang, Jiunn-Woei Liaw, Jyi-Tyan Yeh, Jonq-Min Liu, Chau-Shiung Yeh, and Chih-Kung Lee. Physical origin of directional beaming emitted from a subwavelength slit. *Phys. Rev. B*, 71:041405, 2005.
- [88] D. Egorov, B. S. Dennis, and G. Blumberg. Two-dimensional control of surface plasmons and directional beaming from arrays of subwavelength apertures. *Phys. Rev. B*, 70:033404, 2004.

- [89] H. J. Lezec, A. Degiron, E. Devaux, R. A. Linke, L. Martin-Moreno, F. J. Garcia-Vidal, and T. W. Ebbesen. Beaming light from a subwavelength aperture. *SCIENCE*, 297:820, 2002.
- [90] F. Ramos-Mendieta and P. Halevi. Surface electromagnetic waves in two-dimensional photonic crystals: effect of the position of the surface plane. *Phys. Rev. B*, 59:15 112, 1999.
- [91] W. M. Robertson, G. Arjavalingam, R. D. Meade, K. D. Brommer, A. M. Rappe, and J. D. Joannopoulos. Observation of surface photons on periodic dielectric arrays. *Opt. Lett.*, 18:528, 1993.
- [92] E. Ozbay and B. Temelkuran. Reflection properties and defect formation in photonic crystals. *Appl. Phys. Lett.*, 69:743, 1996.
- [93] Irfan Bulu, Humeyra Caglayan, and Ekmel Ozbay. Radiation properties of sources inside photonic crystals. *Phys. Rev. B*, 67:205103, 2003.
- [94] Steven G. Johnson, Pierre R. Villeneuve, Shanhui Fan, and J. D. Joannopoulos. Linear waveguides in photonic-crystal slabs. *Phys. Rev. B* 62, 62:8212, 2000.
- [95] Mehmet Bayindir, B. Temelkuran, and E. Ozbay. Propagation of photons by hopping: A waveguiding mechanism through localized coupled cavities in three-dimensional photonic crystals. *Phys. Rev. B*, 61:R11855, 2000.
- [96] Esteban Moreno, F. J. Garcia-Vidal, and L. Martin-Moreno. Enhanced transmission and beaming of light via photonic crystal surface modes. *Phys. Rev. B*, 69:121402, 2004.
- [97] H. A. Bethe. Theory of diffraction by small holes. *Phys. Rev.*, 66:163–182, 1944.
- [98] A. Chutinan and S. Noda. Waveguides and waveguide bends in two-dimensional photonic crystal slabs. *Phys. Rev. B*, 62:4488–4492, 2000.
- [99] Mehmet Bayindir and E. Ozbay. Dropping of electromagnetic waves through localized modes in three-dimensional photonic band gap structures. *Appl. Phys. Lett.*, 81:4514, 2002.

- [100] S. Fan, P. R. Villeneuve, J. D. Joannopoulos, and H. A. Haus. Channel drop tunneling through localized states. *Phys. Rev. Lett.*, 80:960, 1998.
- [101] H. Kosaka, T. Kawashima, A. Tomita, M. Notomi, T. Tamamura, T. Sato, and S. Kawakami. Photonic crystals for micro lightwave circuits using wavelength-dependent angular beam steering. *Appl. Phys. Lett.*, 74:1370, 1999.
- [102] S. Noda, A. Chutinan, and M. Imada. Trapping and emission of photons by a single defect in a photonic bandgap structure. *Nature*, 407:608, 2000.
- [103] Stefan Enoch, Boris Gralak, and Gerard Tayeb. Enhanced emission with angular confinement from photonic crystals. *Appl. Phys. Lett.*, 81:1588, 2002.
- [104] M. Notomi. Theory of light propagation in strongly modulated photonic crystals: Refractionlike behavior in the vicinity of the photonic band gap. *Phys. Rev. B*, 62:10696, 2000.
- [105] S. Foteinopoulou and C. M. Soukoulis. Negative refraction and left-handed behavior in two-dimensional photonic crystals. *Phys. Rev. B* 67, 67:235107, 2003.
- [106] Ertugrul Cubukcu, Koray Aydin, Ekmel Ozbay, Stavroula Foteinopoulou, and Costas M. Soukoulis. Electromagnetic waves: Negative refraction by photonic crystals. *Nature*, 423:604, 2003.
- [107] Chiyan Luo, Steven G. Johnson, J. D. Joannopoulos, and J. B. Pendry. Negative refraction without negative index in metallic photonic crystals. *Opt. Express*, 11:746, 2003.
- [108] Chiyan Luo, Steven G. Johnson, J. D. Joannopoulos, and J. B. Pendry. All-angle negative refraction without negative effective index. *Phys. Rev. B*, 65:201104, 2002.
- [109] Boris Gralak, Stefan Enoch, and Gerard Tayeb. Anomalous refractive properties of photonic crystals. *J. Opt. Soc. Am. A*, 17:1012, 2000.

- [110] Sanshui Xiao, Min Qiu, Zhichao Ruan, and Sailing He. Influence of the surface termination to the point imaging by a photonic crystal slab with negative refraction. *Appl. Phys. Lett.*, 85(19):4269, 2004.
- [111] Hiroyuki Takeda and Katsumi Yoshino. Tunable photonic band schemes in two- and three-dimensional photonic crystals with double periodicity and their applications. *Jpn. J. Appl. Phys.*, 41:L773, 2002.
- [112] Chongjun Jin, Bingying Cheng, Baoyuan Man, Daozhong Zhang, Shouzheng Ban, Bo Sun, Lieming Li, Xiangdong Zhang, and Zhaoqing Zhang. Two-dimensional metallodielectric photonic crystal with a large band gap. *Appl. Phys. Lett.*, 75:1201, 1999.
- [113] K. Sakoda. *Optical Properties of Photonic Crystals*. Springer, Germany, 2001.
- [114] T. Ito and K. Sakoda. Photonic bands of metallic systems. ii. features of surface plasmon polaritons. *Phys. Rev. B*, 64:045117, 2001.
- [115] Patanjali V. Parimi, Wentao T. Lu, Plarenta Vodo, and Srinivas Sridhar. Photonic crystals: Imaging by flat lens using negative refraction. *Nature*, 426:404, 2003.
- [116] Ilya V. Shadrivov, Andrey A. Sukhorukov, and Yuri S. Kivshar. Beam shaping by a periodic structure with negative refraction. *Appl. Phys. Lett.*, 82:3820, 2003.
- [117] Hi-Yuan Li and Lan-Lan Lin. Evaluation of lensing in photonic crystal slabs exhibiting negative refraction. *Phys. Rev. B*, 68:245110, 2003.
- [118] A. Martnez, H. Miguez, A. Griol, and J. Mart. Experimental and theoretical analysis of the self-focusing of light by a photonic crystal lens. *Phys. Rev. B*, 69:165119, 2004.
- [119] James A. Lock and Judith R. Woodruff. An analysis of two unusual reflection caustics. *Am. J. Phys*, 57:260, 1989.
- [120] James A. Lock and James H. Andrews. Optical caustics in natural phenomena. *Am. J. Phys*, 60:397, 1992.

Appendix A

Publications in SCI journals

1. E. Ozbay, Irfan Bulu, and Humeyra Caglayan, "Transmission, refraction, and focusing properties of one, two, and three dimensional labyrinth based left-handed metamaterials," (To Be Published Physica Status Solidi B)
2. Irfan Bulu, Humeyra Caglayan, Koray Aydin, and Ekmel Ozbay, "Study of the field emitted by a source placed inside a two dimensional left-handed metamaterial," (To Be Published Optics Letters)
3. E Ozbay, Koray Aydin, Irfan Bulu and Kaan Guven, "Negative refraction, subwavelength focusing and beam formation by photonic crystals," Journal of Physics D: Applied Physics (in press).
4. Koray Aydin, Irfan Bulu, and Ekmel Ozbay "Electromagnetic wave focusing from sources inside a two-dimensional left-handed material superlens," New Journal of Physics, volume 8, 221 (2006).
5. Irfan Bulu, Humeyra Caglayan, and Ekmel Ozbay "Designing materials with desired electromagnetic properties," Microwave and Optical Technology Letters, volume 48, 2611(2006).
6. Koray Aydin, Irfan Bulu, and Ekmel Ozbay "Verification of impedance matching at the surface of left-handed materials," Microwave and Optical Technology Letters, volume 48, 2548(2006).

7. Humeyra Caglayan, Irfan Bulu, and Ekmel Ozbay "Plasmonic structures with extraordinary transmission and highly directional beaming properties," *Microwave and Optical Technology Letters*, volume 48, 2491(2006).
8. Ekmel Ozbay, Irfan Bulu, Kaan Guven, Humeyra Caglayan, and Koray Aydin, "Observation of Negative Refraction and Focusing in Two-Dimensional Photonic Crystals," *Japanese Journal of Applied Physics*, Vol. 45, 6064 (2006).
9. M. Gokkavas, K. Guven, I. Bulu, K. Aydin, R.S. Penciu, M. Kafesaki, C.M. Soukoulis, and E. Ozbay, "Experimental demonstration of a left-handed metamaterial operating at 100 GHz," *Physical Review B*, vol. 73, 193103 (2006).
10. S. Sena Akarca-Biyikli, Irfan Bulu, and Ekmel Ozbay, "Resonant excitation of surface plasmons in one-dimensional metallic grating structures at microwave frequencies," *J. Opt. A: Pure Appl. Opt.*, vol. 7, 159 (2005).
11. Ekmel Ozbay, Irfan Bulu, Koray Aydin, Humeyra Caglayan, K. Bora Alici, and Kaan Guven, "Highly Directive Radiation and Negative Refraction Using Photonic Crystals," *Laser Physics Journal*, Vol. 15, 217 (2005).
12. H. Caglayan, I. Bulu, and E. Ozbay, "Extraordinary grating-coupled microwave transmission through a subwavelength annular aperture," *Opt. Express* 13, 1666-1671 (2005).
13. I. Bulu, H. Caglayan, and E. Ozbay, "Negative refraction and focusing of electromagnetic waves by metallodielectric photonic crystals ", *Phys. Rev. B* 72, 045124 (2005).
14. K Aydin, I Bulu, K Guven, M Kafesaki, C M Soukoulis and E Ozbay, "Investigation of magnetic resonances for different split ring resonator parameters and designs ", *New Journal of Physics* 7, 168 (2005).
15. Irfan Bulu, Humeyra Caglayan, and E Ozbay, "Beaming of Light and Enhanced Transmission via Surface Modes of Photonic Crystals ", *Optics Letters* 30, 3078 (2005).

16. Humeyra Caglayan, Irfan Bulu, and E Ozbay, "Highly directional enhanced radiation from sources embedded inside three-dimensional photonic crystals", *Optics Express* 13, 7645 (2005).
17. Irfan Bulu, H Caglayan, K Aydin and E Ozbay , "Compact size highly directive antennas based on SRR metamaterial medium", *New Journal of Physics* 7, 223 (2005).
18. Koray Aydin, Irfan Bulu, and Ekmel Ozbay , "Focusing of electromagnetic waves by a left-handed metamaterial flat lens", *Optics Express* 13, 8753 (2005).
19. Irfan Bulu, Humeyra Caglayan, and Ekmel Ozbay , "Experimental demonstration of labyrinth-based left-handed metamaterials", *Optics Express* 13, 10238 (2005).
20. Irfan Bulu, Humeyra Caglayan, and Ekmel Ozbay , "Experimental Demonstration of Sub-wavelength Focusing of Electromagnetic Waves by Labyrinth Based Two-Dimensional Metamaterials", *Optics Letters*, vol. 31, 814 (2006).
21. Humeyra Caglayan, Irfan Bulu, and E Ozbay, "Beaming of electromagnetic waves emitted through a subwavelength annular aperture", *Journal of Optical Society of America B*. 23, p. 419 (2006).
22. "Enhanced transmission of microwave radiation in one-dimensional metallic gratings with subwavelength aperture", S. Sena Akarca-Biyikli, Irfan Bulu, and Ekmel Ozbay, *Appl. Phys. Lett.* 85, 1098 (2004).
23. Ekmel Ozbay, Irfan Bulu, Koray Aydin, Humeyra Caglayan, and Kaan Guven, "Physics and applications of photonic nanocrystals", *International Journal of Nanotechnology*, vol. 1, 379 (2004).
24. Ekmel Ozbay, Irfan Bulu, Koray Aydin, Humeyra Caglayan, and Kaan Guven, "Physics and applications of photonic crystals", *Photonics and Nanostructures*, vol. 2, 87 (2004).

25. "Highly directive radiation from sources embedded inside photonic crystals", Irfan Bulu, Humeyra Caglayan, and Ekmel Ozbay, *Appl. Phys. Lett.* 83, 3263 (2003).
26. "Radiation properties of sources inside photonic crystals", Irfan Bulu, Humeyra Caglayan, and Ekmel Ozbay, *Phys. Rev. B* 67, 05103 (2003).
27. "Investigation of localized coupled-cavity modes in two-dimensional photonic band gap structures", Mehmet Bayindir, I. Bulu, E. Cubukcu, and E. Ozbay *IEEE Journal of Quantum Electronics*, (2002).
28. "Photonic band gap effect, localization, and waveguiding in two-dimensional Penrose lattice", Mehmet Bayindir, E. Cubukcu, I. Bulu, and E. Ozbay *Physical Review B*, volume 63, No 161104(R) (2001).
29. "Photonic band gaps, defect characteristics, and waveguiding in two-dimensional disordered dielectric and metallic photonic crystals", Mehmet Bayindir, E. Cubukcu, I. Bulu, T. Tut, E. Ozbay, and C. M. Soukoulis *Physical Review B*, volume 64, No 195113 (2001).
30. "Photonic band gaps and localization in two-dimensional metallic quasicrystals", Mehmet Bayindir, E. Cubukcu, I. Bulu, and E. Ozbay *Europhysics Letters*, volume 56, page 41 (2001).

Appendix B

Conference Proceedings

1. E. Ozbay, Irfan Bulu "The almost magical world of negative index materials", EU NoE Phoremost Florence Workshop June 18-22, 2006, Montegufoni (Florence), Italy.
2. K. Aydin, Irfan Bulu, and E. Ozbay, "Negative refraction and focusing by a left-handed material slab in free space", CLEO/QELS Meeting, May 21-26, 2006 Long Beach, CA.
3. K. Aydin, I. Bulu, K. Guven, and E. Ozbay, "Transmission properties of various split ring resonator systems", CLEO/QELS Meeting, May 21-26, 2006 Long Beach, CA.
4. Irfan Bulu, Humeyra Caglayan, and Ekmel Ozbay, "Designing materials with desired electromagnetic properties" Third Workshop on Metamaterials and Special Materials for Electromagnetic Applications and TLC, Rome, Italy, 30-31 March, 2006.
5. K. Aydin, I. Bulu, and E. Ozbay, "Verification of impedance matching at the surface of left-handed materials" Third Workshop on Metamaterials and Special Materials for Electromagnetic Applications and TLC, March 30-31 2006, Rome, Italy.
6. Humeyra Caglayan, Irfan Bulu, and Ekmel Ozbay, "Plasmonic structures

with extraordinary transmission and highly directional beaming properties” Third Workshop on Metamaterials and Special Materials for Electromagnetic Applications and TLC, Rome, Italy, 30-31 March, 2006.

7. (INVITED) Ekmel Ozbay, Irfan Bulu, ”Negative Refraction and Subwavelength Focusing using left handed photonic crystals and metamaterials,” Materials Research Society Meeting, San Francisco, April 17-20, 2006.
8. (INVITED) Ekmel Ozbay, Irfan Bulu, ”Experimental demonstration of subwavelength imaging by labyrinth based left handed composite metamaterials,” SPIE Photonics West meeting, San Jose, CA, USA Jan. 23-27, 2006.
9. (INVITED) Ekmel Ozbay, Irfan Bulu, ”Development of left-handed composite materials and negative refracting photonic crystals with subwavelength focusing,” SPIE Photonics East meeting, Boston, MA, USA Oct. 23-26, 2005.
10. (INVITED) Ekmel Ozbay, Irfan Bulu, ”EU-METAMORPHOSE: European Network of Excellence on Metamaterials,” 1st Annual workshop on Advances in Nanophotonics, Heraklion, Greece, Oct. 10-11, 2005.
11. (INVITED) Ekmel Ozbay, Irfan Bulu, ”Negative Refraction and Subwavelength Focusing Using photonic crystals,” International Conference on Electromagnetics in Advanced Applications (ICEAA 05), Torino, Italy September 12-15, 2005.
12. (INVITED) Ekmel Ozbay, Irfan Bulu, ”Negative Refraction and Subwavelength Focusing using Photonic Crystals,” Conference on Photonics Crystals and Fibers, SPIE Optics and Optoelectronics, Warsaw, Poland August 29-September 02 2005.
13. (INVITED) Ekmel Ozbay, Irfan Bulu, ”Development of left-handed composite metamaterials and negative refracting photonic crystals with subwavelength focusing,” International International Workshop on Nanophotonics and Nanobiotechnology, Istanbul, June 28-July 8, 2005.

14. (INVITED) Ekmel Ozbay, Irfan Bulu, "Development of left-handed composite materials and negative refracting photonic crystals with subwavelength focusing," EPFL Latsis Symposium, Lausanne, Switzerland, Feb 28-March 02, 2005.
15. Humeyra Caglayan, Irfan Bulu, and Ekmel Ozbay, "Highly directional enhanced radiation from sources embedded inside 2- and 3-D photonic crystals," San Jose, California, USA, 22-27 January 2005
16. Humeyra Caglayan, Irfan Bulu, and Ekmel Ozbay, "Extraordinary grating-coupled microwave transmission through a subwavelength annular aperture," Central European Workshop on Quantum Optics, Ankara, Turkey, June 6-9 2005.
17. Humeyra Caglayan, Irfan Bulu, and Ekmel Ozbay, "Enhanced Confined Light Transmission by Single Subwavelength Apertures" International Workshop on Nanophotonics and Nanobiotechnology, Istanbul, Turkey, June 28-July 8, 2005
18. Irfan Bulu, Humeyra Caglayan, and Ekmel Ozbay, "Resonant Transmission and Beaming of Electromagnetic Waves via Photonic Crystal Surface States," PECS-VI: International Symposium on Photonic and Electromagnetic Crystal Structures, Aghia Pelaghia, Crete, Greece, June 19-24, 2005.
19. Irfan Bulu, Humeyra Caglayan, and Ekmel Ozbay, "Negative refraction and focusing of electromagnetic waves by metallodielectric photonic crystals," Central European Workshop on Quantum Optics, Ankara, Turkey, June 6-9 2005.
20. (INVITED) Ekmel Ozbay, Irfan Bulu, "Physics and Applications of Photonic Crystals," 13th International Laser Physics Conference (LPHYS'04), Trieste, Italy, July 12-16 2004.
21. (INVITED) Ekmel Ozbay, Irfan Bulu, "Physics and Applications of 2D and 3D Photonic Crystals," 5th Photonics and Electromagnetic Crystals Conference (PECS-V), Kyoto, Japan, March 8-11, 2001.

22. (INVITED) Ekmel Ozbay, Irfan Bulu, Koray Aydin, Humeyra Caglayan, Kaan Guven, "Physics and Applications of Photonic Crystals," 323. WE-Heraeus-Seminar, Physikzentrum Bad Honnef, Germany, 26 - 30 April 2004.
23. Irfan Bulu, Humeyra Caglayan, and Ekmel Ozbay, "Radiation properties of sources embedded inside photonic crystals," Progress in Electromagnetic Research Symposium 2004, Pisa, Italy, March 28-31, 2004.
24. Ekmel Ozbay, Koray Aydin, and Kaan Guven, "Transmission and reflection properties of composite double negative materials in free space," Progress in Electromagnetic Research Symposium 2004, Pisa, Italy, March 28-31, 2004.
25. Irfan Bulu, Humeyra Caglayan, and Ekmel Ozbay, "Radiation properties of sources embedded inside photonic crystals," Progress in Electromagnetic Research Symposium 2004, Pisa, Italy, March 28-31, 2004.
26. Irfan Bulu, Humeyra Caglayan, and Ekmel Ozbay, "Enhancement of radiation from sources embedded inside photonic crystals," W.3 International Meeting: Optical Properties of Complex Materials over Different Length Scales, San Sebastian, Spain, July 7-11, 2003.
27. Ekmel Ozbay, Mehmet Bayindir, Ertugrul Cubukcu, and Irfan Bulu, "Coupled Cavities in Photonic Crystals," , SPIE Photonics West meeting, San Jose, CA, USA 21-25 Jan. 2002, Proceedings of the SPIE vol.4655, p.16 (2003).
28. Irfan Bulu, Humeyra Caglayan, and Ekmel Ozbay, "Enhancement of radiation from sources embedded inside photonic crystals," Third International Wilhelm and Else Heraeus Summer School on Photonic Crystals: Optical Materials for the 21st Century. Wittenberg, Germany, July 15-25, 2002.
29. " Mehmet Bayindir, E. Cubukcu, I. Bulu, and E. Ozbay, "Photonic band gap effect and localization in two-dimensional Penrose lattice," QELS 2001 Technical Digest, page 122 (CLEO/QELS Meeting, May 6-11, Baltimore).

30. Mehmet Bayindir, Irfan Bulu, and Ekmel Ozbay, "Disorder effects in two dimensional photonic crystals," PECS-3: Electromagnetic Crystal Structures, St. Andrews, Scotland, 9-14 June 2001.
31. Mehmet Bayindir, E. Cubukcu, I. Bulu, E. Ozbay, and C. M. Soukoulis, "Influence on disorders on photonic band gaps defect characteristics, waveguiding in two-dimensional dielectric and metallic photonic crystals," OSA/ILS'01 meeting, Los Angeles, October 2001
32. Evrim Colak, Irfan Bulu, and Ekmel Ozbay "Theoretical and experimental study of enhancement of extraction efficiency in GaN LEDs by use of photonic bandgap structures," 2nd Annual workshop on Advances in Nanophotonics, Vilnius, Lithuania, September 25-27, 2006.
33. Maria Kafesaki, Costas Soukoulis, Irfan Bulu, and Ekmel Ozbay "Surface Modes in Photonics Crystals," 2nd Annual workshop on Advances in Nanophotonics, Vilnius, Lithuania, September 25-27, 2006.
34. Koray Aydin, Irfan Bulu, Kaan Guven, Deniz and Ekmel Ozbay, "Sub-wavelength imaging and resolution by left-handed material superlens," The 1st European Topical Meeting on Nanophotonics and Metamaterials 8-11 January, 2007, Seefeld, Tirol, Austria
35. Irfan Bulu, Humeyra Caglayan and Ekmel Ozbay, "Ultra small cavities by use of metamaterials," The 1st European Topical Meeting on Nanophotonics and Metamaterials 8-11 January, 2007, Seefeld, Tirol, Austria
36. Humeyra Caglayan, Irfan Bulu, and Ekmel Ozbay, "Focusing surface waves via changing the incident angle," The 1st European Topical Meeting on Nanophotonics and Metamaterials 8-11 January, 2007, Seefeld, Tirol, Austria
37. (INVITED) I. Bulu, and E. Ozbay, "Negative refraction and subwavelength focusing using left-handed 3D composite metamaterials," The 1st European Topical Meeting on Nanophotonics and Metamaterials 8-11 January, 2007, Seefeld, Tirol, Austria